

AD-A270 105

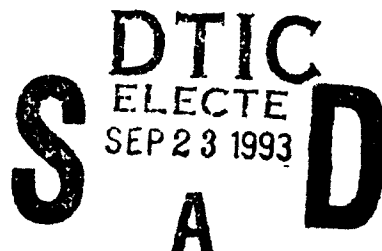


2

PL-TR-93-2172

**ADVANCED WAVEFORM RESEARCH
METHODS FOR GERESS RECORDINGS**

**H. P. Harjes
M. Jost
J. Schweitzer
J. Wuster**



**Ruhr-University-Bochum
D-4630 Bochum
FEDERAL REPUBLIC OF GERMANY**

15 April 1993

**Final Report
15 February 1992-14 February 1993**

APPROVED FOR PUBLIC RELEASE; DISTRIBUTION UNLIMITED

93-22038



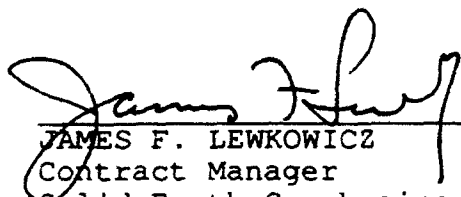
**PHILLIPS LABORATORY
Directorate of Geophysics
AIR FORCE MATERIEL COMMAND
HANSCOM AIR FORCE BASE, MA 01731-3010**

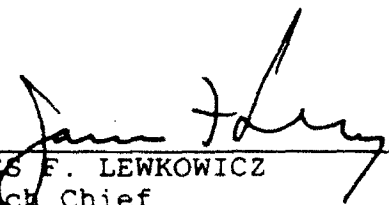


93 9 22 003

The views and conclusions contained in this document are those of the authors and should not be interpreted as representing the official policies, either expressed or implied, of the Air Force or the U.S. Government.

This technical report has been reviewed and is approved for publication.


JAMES F. LEWKOWICZ
Contract Manager
Solid Earth Geophysics Branch
Earth Sciences Division


JAMES F. LEWKOWICZ
Branch Chief
Solid Earth Geophysics Branch
Earth Sciences Division


DONALD H. ECKHARDT, Director
Earth Sciences Division

This document has been reviewed by the ESD Public Affairs Office (PA) and is releasable to the National Technical Information Service (NTIS).

Qualified requestors may obtain additional copies from the Defense Technical Information Center. All others should apply to the National Technical Information Service.

If your address has changed, or if you wish to be removed from the mailing list, or if the addressee is no longer employed by your organization, please notify PL/IMA, 29 Randolph Road, Hanscom AFB MA 01731-3010. This will assist us in maintaining a current mailing list.

Do not return copies of this report unless contractual obligations or notices on a specific document require that it be returned.

REPORT DOCUMENTATION PAGE			Form Approved OMB No. 0704-0188	
Public reporting burden for this collection of information is estimated to average 1 hour per response, including the time for reviewing instructions, searching existing data sources, gathering and maintaining the data needed, and completing and reviewing the collection of information. Send comments regarding this burden estimate or any other aspect of this collection of information, including suggestions for reducing this burden, to Washington Headquarters Services, Directorate for Information Operations and Reports, 1215 Jefferson Davis Highway, Suite 1204, Arlington, VA 22202-4302, and to the Office of Management and Budget, Paperwork Reduction Project (0704-0188), Washington, DC 20503.				
1. AGENCY USE ONLY (Leave blank)	2. REPORT DATE 15 April 1993	3. REPORT TYPE AND DATES COVERED Final (15 Feb 1992 - 14 Feb 1993)		
4. TITLE AND SUBTITLE Advanced Waveform Research Methods for GERESS Recordings		5. FUNDING NUMBERS PE 62714E PR 9A10 TA DA WU AE Contract AFOSR-90-0189		
6. AUTHOR(S) H. P. Harjes J. Wuster M. Jost J. Schweitzer				
7. PERFORMING ORGANIZATION NAME(S) AND ADDRESS(ES) Ruhr-University-Bochum D-4630 Bochum Federal Republic of Germany		8. PERFORMING ORGANIZATION REPORT NUMBER		
9. SPONSORING/MONITORING AGENCY NAME(S) AND ADDRESS(ES) Phillips Laboratory 29 Randolph Road Hanscom AFB, MA 01731-3010 Contract Manager: James Lewkowicz/GPEH		10. SPONSORING/MONITORING AGENCY REPORT NUMBER PL-TR-93-2172		
11. SUPPLEMENTARY NOTES				
12a. DISTRIBUTION/AVAILABILITY STATEMENT Approved for public release; distribution unlimited		12b. DISTRIBUTION CODE		
13. ABSTRACT (Maximum 200 words) The GERESS array project is a cooperative research program, jointly undertaken by Southern Methodist University Dallas (USA) and Ruhr-University Bochum in Germany. It is part of a multi-array network which includes NORESS, ARCESS, and FINESSA in Scandinavia. This report summarizes research activities carried out at the data centre in the Institute of Geophysics in Bochum during 1992. GERESS data are continuously transmitted from the array hub in Bavaria to Bochum via 64 kbit line. In Bochum, an experimental on-line processing system, based on RONAPP, is operated to monitor data quality and initiate maintenance activities. In 1992, Ruhr-University continued the on-site maintenance of the array as part of the research grant. As described in detail in the annual status report (chapter 1), the monthly uptime of the array varied in 1992 between 87.8 % and 99.8 % with an average of 96.9 %. As part of the maintenance, a thorough investigation of the GERESS instrument calibration was performed (chapter 2). Components which were checked, include: GS-13 generator constant, transfer function, and calibration coil motor constant. (continued)				
14. SUBJECT TERMS Waveform GERESS NORESS		ARCESS FINESSA RDAS preamplification		15. NUMBER OF PAGES 132
		A/D conversion Calibration signal		16. PRICE CODE
17. SECURITY CLASSIFICATION OF REPORT Unclassified	18. SECURITY CLASSIFICATION OF THIS PAGE Unclassified	19. SECURITY CLASSIFICATION OF ABSTRACT Unclassified	20. LIMITATION OF ABSTRACT SAR	

RDAS preamplification, A/D conversion, and calibration signal. Although several minor deviations were found, the majority of channels fit the technical specifications on overall sensitivity at 1 Hz within 5 % (13 channels are within 1 %).

At the data centre in Bochum, an automatic event bulletin - interactively reviewed by an analyst - is produced and widely distributed to interested institutions. For 1992, the GERESS contribution to NEIC was especially evaluated (chapter 3). In the teleseismic range (20° - 180°) GERESS detected 44.57 % of the corresponding NEIC events. As expected, the detection capability changed with epicentral distance showing a minimum between 100° and 120° (core shadow). Interestingly, GERESS detected 85 % of all NEIC events which occurred in the PKP caustic range to GERESS. This again demonstrates that sensitive stations at epicentral distances around the PKP caustic can drastically improve the detecting capability for remote areas where nearby observatories are missing and/or are difficult to be installed.

Another study (chapter 4) reports on steep-angle reflections from the Earth's core observed with the GERESS array. These rare observations can either be used to investigate the spherical structure of the Earth or they can serve as additional information for the Earth's tomography.

In chapter 5, the GERESS data base of presumed nuclear tests is extended to include all observations from 1992.

Another paper (chapter 6) presents a method to synthesize the true ground displacement in a very broad frequency range from several band-limited digital recordings. The method is applied to the instruments collocated at the GERESS reference site GEC2.

Finally, our work on discriminating industrial explosions from natural earthquakes at near-regional distances is continued (chapter 7). Source characteristics and firing-techniques for industrial explosions are modeled to quantify the observed time-independent spectral structures in sonograms.

Accession For	
NTIS	CRA&I <input checked="" type="checkbox"/>
DTIC	TAB <input type="checkbox"/>
Unannounced	<input type="checkbox"/>
Justification	
By	
Distribution /	
Availability Codes	
Dist	Avail and/or Special
A-1	

DTIC QUALITY INSPECTED 1

CONTENTS

1. GERESS STATUS REPORT	1
1.1 General	1
1.2 GERESS Observatory at Ruhr-University Bochum	1
1.3 GERESS Array Hub	3
1.4 Conclusion	6
References	7
Appendix 1-1: Chronological Status List GERESS	9
2. REPORT ON GERESS INSTRUMENT CALIBRATION	18
2.1 Abstract	18
2.2 The Problem	18
2.3 Routine Calibration Checks	19
2.4 Transfer Functions	21
2.5 RDAS Signal Generator	24
2.6 Pre-Amplifier and A/D-Converter	24
2.7 Seismometer Generator Constant	25
2.8 Shaking Table Experiments	27
2.9 Electrical Excitation	29
2.10 Calibration Irregularities	30
2.11 Conclusions	
References	32
3. TELESEISMIC DETECTION AND LOCATION CAPABILITIES OF THE GERESS ARRAY	33
3.1 Introduction	33
3.2 GERESS Detection Capabilities	33
3.3 GERESS Mislocation Vectors	35
3.4 Travel Time and Amplitude Residuals of GERESS	36
3.5 Conclusion	37
References	38
4. STEEP ANGLE REFLECTIONS FROM THE EARTH'S CORE OBSERVED WITH THE GERESS ARRAY	51
4.1 Introduction	51
4.2 PcP Observations in Less Than 35° Epicentral Distance	51
4.3 Observations in Less Than 20° Epicentral Distance	54
4.4 PKiKP Observation With the GERESS Array 51.4°	55

	Contents
4.5 Conclusion	56
References	56
5. GERESS RECORDINGS OF PRESUMED NUCLEAR TESTS IN 1992	80
5.1 Introduction	80
5.2 Lop Nor	81
5.3 Nevada	81
References	82
6. SYNTHESIS OF BROAD BAND DISPLACEMENT SEISMOGRAMS FROM BAND LIMITED DIGITAL REGISTRATIONS	89
6.1 Summary	89
6.2 Introducing the Method	89
6.3 An Example	90
6.3.1 Restitution of True Ground Movements	90
6.3.2 Adjustment of Sample Frequencies	95
6.3.3 Compensation of Time Shifts	95
6.3.4 Tailoring of Individual Passbands	95
6.3.5 Addition and Numerical Differentiation	95
6.4 Verification	98
6.5 Discussion	99
Appendix I	101
Appendix II	103
7. QUANTIFICATION OF TIME-INDEPENDENT SPECTRAL STRUCTURES IN SONOGRAMS	106
7.1 Introduction	106
7.2 Why Quantify?	106
7.3 Cepstral Analysis	109
7.4 Harmonic Product Spectrum	114
7.5 Horizontal Sums	114
7.6 Determination of Blasting Delays	117
7.7 Discussion	119
References	120

1. GERESS STATUS REPORT

January 1992 - December 1992

Michael L. Jost

1.1 General

The German Experimental Seismic System (GERESS) is a cooperative research program of Southern Methodist University Dallas, Texas; and Ruhr-University Bochum, Germany. It is an extension of the Scandinavian regional array network, i. e., NORESS, ARCESS, and FINESA, into Central Europe. The GERESS array is located in the Bavarian Forest area at the southeastern part of Germany near the border to Austria and Czechoslovakia. The array consists of 25 stations with vertical-component short-period Teledyne Geotech GS-13 instruments sampled at 40 Hz. In addition, four of the sites include horizontal component instruments. At the key station of the array, GEC2 (48.84511 N, 13.70156 E, 1132 m), a STS-2 is sampled with 80 Hz (broad-band element). The geometry of the array is based on concentric rings providing an overall aperture of about 4 km. The GERESS aperture is larger than that of NORESS by a factor of 4/3 which resulted from signal and noise correlation measurements by Harjes (1990). The array became fully operational in January 1991. Data from the array were continuously transmitted to NORSAR and to the Institute of Geophysics, Ruhr-University Bochum via 64-kbit telephone lines in 1992. In early 1993, the NORSAR line has been terminated and a wide area network (WAN) has been established between the GERESS data centers in Bochum and Kjeller (Figure 1-1).

1.2 GERESS Observatory at Ruhr-University Bochum

The Department of Geophysics of Ruhr-University Bochum operates an experimental on-line processing system for GERESS data (Harjes et al., 1993). This system uses software developed at NORSAR (Mykkeltveit and Bungum, 1984; Fyen, 1987). During the Group of Scientific Experts Technical Test (GSETT-2) and in 1992 numerous updates to the program package were implemented in Bochum.

The on-line processing consists of 3 steps: detection, fk-analysis, and location. The first stage of the on-line processing accesses data in 30 second

segments and runs a STA/LTA detector. The detector presently recognizes an onset if the STA/LTA ratio for a filtered trial-beam exceeds a threshold of 4. The next step of the on-line processing is the transformation of a 3 second filtered data segment at each onset time (derived from the detection time) into the frequency-wavenumber domain. As a result, the slowness and back-azimuth of the phase is determined. From the slowness information, seismic phases are identified. The final step of the on-line data processing is the location of events. The seismic phases as identified in the fk-analysis are associated to events in this step. From the arrival time difference of regional phases, the distance to the epicenter can be determined from the Jeffreys - Bullen travel time tables for regional seismic phases. Together with a mean back-azimuth, the epicenter locations of local and regional events are determined. For 1992, 18 events have been automatically located each day on average (Table 1-1). Figure 1-2 shows the automatic event locations for 1992.

Since October 1992, analysts started to review regional events. They repicked onset times, redetermined back-azimuths and phase velocities, and relocated events using the LOCSAT routine which is a modified version of TTA-ZLOC (Bratt and Bache, 1988). Figure 1-3 (Schulte-Theis, pers. comm.) shows the relocated events from Oct-Dec 1992.

Table 1-1
Statistics on the GERESS Bochum On-line Processing for 1992

	number	number/day
detections	62749	171
f-k analyses	57090	156
locations	6540	18

At Bochum, local magnitudes are calculated by the following procedure (the algorithm was implemented by J. Schweitzer):

- 1) Determination of the optimum S-phase beam.
- 2) High-pass filter at 0.7 Hz.
- 3) Transformation of beam-trace to a Wood-Anderson record.
- 4) Picking of maximum amplitude of the S-waves and correction for epicentral distance.

The ML magnitude distance correction from Gutenberg and Richter (1956) was changed following the procedure of Ebel (1982) using the attenuation relation for France from Nicolas *et al.* (1982). In addition to the beam magnitude, local magnitudes have been determined for the single station C2 and for the horizontal components in a similar way. Usually, all 3 magnitude values differ less than about 0.3 magnitude units. On the other hand, GERESS local magnitudes

appear low by at least 0.5 magnitude units compared to values published by other European networks.

Since Sep. 1991, the results of the on-line processing have been sent to interested institutions via e-mail (e.g. Bundesanstalt für Geowissenschaften und Rohstoffe (BGR), Frankfurt University, Gräfenberg Array, ORFEUS, seismological institutes in CSFR, Hungaria, Slovenia, Switzerland; Stuttgart University). In addition, the On-line Processing Display Manager (Jost, 1991) has been used by many scientists for near real time information on parameter data. Recently, a Data Request Manager (DRM) by Krake Inc. has been installed for trial operation. The DRM should enable the transmission of data (GSE, SEED) and interfaces to the German Regional Network of Broad-Band Stations.

Since late October 1991, alert messages of strong teleseismic and regional events are automatically sent to NEIC (Golden, CO) and BGR in near real-time. 46 times, GERESS alert messages were used in NEIC alerts in 1992. In addition, teleseismic events have been routinely reevaluated by an analyst, and parameter data (onset time, amplitude, period, azimuth and slowness) for 11649 phases (i.e., 32 phases per day) have been sent to NEIC (Golden, CO) and other institutions in 1992.

In 1992, the data acquisition software (TM Science Horizons) was upgraded several times and became robust. The RDAS-200 appears to send infrequently data with corrupted time stamps. These data appear to be in the future (Figure 1-4). In 1992, SHI succeeded in taking care of this problem by software improvements. Table 1-3 shows that the outage due to future data entering the data acquisition process amounted to more than 2 days in 1992. One old problem of the data acquisition software has still remained up to the end of 1992: About once a month, the SCHEDULER driven program MRG crashes 2 consecutive times. This results in a data loss of 30 minutes. Table 1-3 shows that data loss due to this problem caused outage that amounted to 7.5 hours in 1992.

1.3 GERESS Array Hub

The GERESS array showed stable operation in 1992. Table 1-2 shows the uptime of the system including the Bochum Observatory (uptimes directly correspond to the data archived in Bochum). The average uptime was 96.9 %, i.e., the total outage amounts to 11.2 days in 1992. The highest uptime

Table 1-2
GERESS uptime in 1992 (incl. Bochum data center)

Month	uptime %
Jan	99.7
Feb	99.0
Mar	87.8
Apr	91.5
May	97.5
Jun	94.2
Jul	96.0
Aug	99.4
Sep	99.6
Oct	99.5
Nov	99.4
Dec	99.8

Table 1-3
Causes of GERESS downtimes in 1992 (incl. Bochum data center)
(The total downtime was 980300 sec)

cause	downtime [sec]	downtime [%]
Bochum data acq. software (SS2DL)	16620	1.7
Bochum data acq. software (SCHEDULER)	27000	2.8
Bochum data acq. software (future data received)	178310	18.2
Bochum data acq. software (maintenance)	4265	0.4
Bochum data acq. workstation	97900	10.0
Bochum CIM	2155	0.2
Bochum power outage	19888	2.0
total outage Bochum	346138	35.3
Communication line	9467	1.0
HUB IAC crashes	329295	33.6
HUB thunderstorm damage	203490	20.8
HUB maintenance	50719	5.2
HUB power outage	11226	1.1
total outage HUB	594730	60.7
other causes	29965	3.0

(99.8 %) was observed in December 1992; the lowest uptime (87.8 %) occurred in March 1992 due to thunderstorm damage at the array site. Table 1-3 further specifies the causes of the observed outages. The causes of the downtimes are clearly related to the well known problems of this installation. The technical status of GERESS is summarized in chronological order in Appendix 1-1 (comprehensive monthly status reports are available upon request).

In 1992, the technical installation of GERESS could not be considered fully acceptable. Problems have been identified during the GERESS System Verification Test in September 1991 (Golden et al., 1991): A persistent problem is that data gaps are inherent in the IAC. The number of 1-second gaps per data channel were found to form 4 groups. These 4 groups correspond to the 4 communication boards (digiboards) on the array-controller (Table 1-4). The reason is that the digiboards perform sporadic self-resets, loosing about 9 seconds of data each time (Figure 1-5). Therefore, the overall data loss is significantly greater than the loss in data transmission as specified and observed by the German Telekom (1 bit in $10E+06$).

Based on the findings of the GERESS System Verification Test, Teledyne Geotech started corrective action under warranty. In May 1992, a hardware (IAC) and software upgrade (IAC and RDAS-200) was sent by Teledyne and installed by Bochum engineers. The idea of the upgrade was to make the baud rates between the RDAS'es and digiboards in the IAC different. Unfortunately, this upgrade did not solve the data gap problem (Table 1-4, Figure 1-5). At Dallas, Teledyne Geotech has continued to work on this problem; but at the end of 1992, the data gap problem still awaits a solution.

Table 1-4

Number of 1 second data gaps averaged for a specific digiboard (DB). Results of 6 tests are given (times were adjusted to a test duration of 241896 seconds).

DB	29.10.92	21.8.92	15.12.91	18.9.91	5.6.91	15.11.90
1	161	137	409	522	176	274
2	270	355	511	1084	527	459
3	131	216	181	194	240	?
4	103	158	99	161	97	?

It has been noted that the optical data links between RDAS'es and HUB are very sensitive to lightning damage due to destruction of optical modems which are fed by DC power from the HUB. This means that the optical links have to undergo maintenance work comparatively often. Since proper equipment to adjust these links is extremely expensive (and does not exist at GERESS), the adjustment is done by trial and error. A deviation or drift from

the optimum adjustment means that time synchronization pulses (1 pps signals) can be distorted, hence the synchronization of the array is fundamentally affected. An example: On Nov 3, it was noted that C5 was out of synchronization by 0.4 seconds. The exact start time of desynchronization was determined as Aug 17. At that time, strong thunderstorms had damaged various channels of the array repeatedly and also damaged the optical modem of C5. Unfortunately this had not been noticed at that time. One problem is that the synchronization can only be checked by looking at strong teleseismic onsets. Another indicator of a possible misadjustment in the optical links are self-resets of RDAS'es (e.g.: D5 (Jan), D8 (Apr), B1 (May), B3 (May), B1 (Jun), C7 (Jun), C5 (Jun, Jul), D8 (Jun-Oct), D9 (Aug), D1 (Sep), A2 (Sep-Dec), B3 (Oct)). For stable channel synchronization, possibilities to provide each RDAS with an independent time receiver should be investigated. However low cost GPS receivers reach a synchronization (± 1 msec) that seems not sufficient.

The current release of RDAS-200 software installed at GERESS shows a problem: A station does not synchronize with the GERESS master clock after it comes on-line after a power shutdown. In addition, the RDAS does not execute time-sets promptly, sometimes a reinit followed by a time-set works, sometimes several time-sets are necessary. Furthermore, various channels have shown "artificial" data (i.e., pure electronic noise that mimics seismic noise pretty closely in the time domain (e.g. Figure 1-6)). These instances appear after a power up or after a self-reset and vanish only after a manual reinit from Bochum.

Some channels of GERESS show a significant higher noise level due to site effects (Jost, 1993). The vaults of A0, A3, and B3 could not be placed on bedrock but are on very local pockets of weathered granite or gneiss. In order to move these channels within the rigid restrictions set by the array layout, a shallow refraction study was performed near station A0 and A3 in cooperation with the BGR (Gestermann, 1993). This was the first step of a mapping project of the bedrock around the critical stations. Gestermann (1993) concluded that bedrock can be reached at a depth of 45 m below A0 and 35 m below A3. In the vicinity of A0, a syncline seems to be present and a lateral shift of the station location is prohibitive. Therefore, a bore-hole seismometer should be emplaced. For A3 and B3, further mapping of the basement depth should enable a lateral shift of station positions.

1.4 Conclusion

At the GERESS data center Bochum, 18 regional events have been automatically located daily on average. In addition, extensive parameter data

for 32 teleseismic phases have been interactively determined each day on average. The GERESS data center Bochum is the only German station that provides NEIC with alert messages. In conclusion, GERESS is the most sensitive seismological station in Central Europe.

The Bochum observatory routine included data archival and automatic on-line analysis. The automatic locations of regional events render a good first solution, in general. Since October 1992, regional locations are reevaluated by analysts. Results of the interactive re-analysis of teleseismic data have been used by NEIC for the PDE. In addition, interested institutions have used parameter data of GERESS for their tasks. The Bochum observatory is an open station similar to the German Regional Network of Broad-Band Stations. In addition, Bochum serves as data center where various bulletins (e.g., automatic NEIC locations, NEIC alerts, QED, PDE (weekly), PDE (monthly), fast CMT's from Harvard, onset list of YKA) are available for the interested user.

The GERESS data center Bochum has been responsible for GERESS maintenance. The GERESS uptime which includes the Bochum observatory was 96.9 % in 1992. This demonstrates the high level of reliability of the installation and its successful maintenance. On the other hand, the technical installation of GERESS cannot be considered fully acceptable for the period covered in this report. Problems identified during the GERESS System Verification Test in September 1991 (Golden et al., 1991) have remained unsolved in 1992.

Acknowledgements

J. Schweitzer, N. Gester mann, O. Mindavalli, H. Schulte-Theis, N. Schnieders, B. Klotz, L. Kühne, and O. Richter supported the daily observatory routine. Special thanks are expressed to various officers of the Bundesgrenzschutz (BGS) who helped in many emergency repairs in 1992. The GERESS array is funded by DARPA and its operation is supported by grant AFOSR 90-0189.

Literature

- Bratt, S. R. and T. C. Bache (1988). Locating events with a sparse network of regional arrays, *Bull. Seism. Soc. Am.* 78, 780-798.
- Ebel, J. E. (1982). ML measurements for northeastern United States earthquakes, *Bull. Seism. Soc. Am.* 72, 1367-1378.
- Fyen, J. (1987). Improvements and Modifications, Semiannual Technical Summary, 1 October 1986 - 31 March 1987, *NORSAR Sci. Rep. No. 2-86/87*, Kjeller, Norway.

- Gestermann, N. (1993). Ergebnisse der Refraktionsseismischen Messung am GERESS Array im November 1992, BGR internal report.
- Golden, P., E. T. Herrin, and C. Hayward (1991). Development of an intelligent seismic facility and preparation for participation in the conference on disarmament group of scientific experts technical test. Results of the GERESS verification test, *Quarterly Technical Report SMU-R-91-152*, Southern Methodist University, Dallas, Texas, 64 pp.
- Gutenberg, B. and C. F. Richter (1956). Earthquake magnitude, intensity, energy, and acceleration (2. paper), *Bull. Seism. Soc. Am.* 46, 105-145.
- Harjes, H.-P. (1990). Design and siting of a new regional array in Central Europe, *Bull. Seism. Soc. Am.* 80, 1801-1817.
- Harjes, H.-P., M. L. Jost, J. Schweitzer, and N. Gestermann (1993). Automatic seismogram analysis at GERESS, *Computers & Geosciences* 19, 157-166.
- Jost, M. L. (1991). The Bochum on-line processing display manager, in *Advanced Waveform Research Methods for GERESS Recordings*, DARPA Annual Report No. AFOSR-90-0189, 38-43. PL-TR-91-2134, ADA239199
- Jost, M. L. (1993). SNR improvement by beamforming at GERESS, in *Advanced Waveform Research Methods for GERESS Recordings*, DARPA Annual Report No. AFOSR-90-0189. PL-TR-93-2172
- Mykkeltveit, S. and H. Bungum (1984). Processing of regional seismic events using data from small-aperture arrays, *Bull. Seism. Soc. Am.* 74, 2313-2333.
- Nicolas, M., B. Massinon, P. Mechler, and M. Bouchon (1982). Attenuation of regional phases in Western Europe, *Bull. Seism. Soc. Am.* 72, 2089-2106.

Appendix 1-1: Chronological Status List GERESS

Calibration sequence: Jan-April 8:00-8:13; May-Dec 03:00-03:13. D8 and D9 show abnormal amplitudes at calibration.

Jan. 1992:

- Installation of test version of the Data Request Manager (DRM) by Krake Inc.

Feb. 1992:

- IAC crashes: 2
- Feb. 10 - 14, maintenance visit by RUB engineer.
- Desynchronization on B1 (1 msec due to defective clock board).
- RDAS-200 software update (version 3.01) loaded to C2B (desynchronization problem BB13 on a RDAS-200 (Golden et al., 1991) was not fixed).
- Installation of hardware for power cycling the IAC remotely (e.g., from Bochum) (information provided on the PSAC screen of each RDAS-200 can also be remotely obtained for diagnostics at Bochum).
- At Bochum, a software update for MONITOR_DL (version 1.5.2, SHI) was installed (several problems related to future data generated on the data acquisition system remain).

Mar. 1992:

- IAC crashes: 2
- Data transmission stopped for 3 days due to thunderstorm damage at the HUB.
- Mar 23 - 25, emergency maintenance visit by RUB engineers.
- RDAS-200 software update (version 3.01) loaded to C2B (desynchronization problem BB13 on a RDAS-200 (Golden et al., 1991) fixed).
- At Bochum, a software update for MONITOR_DL (version 1.5.2, SHI) was installed (several problems related to future data generated on the data acquisition system remain).

Apr. 1992:

- IAC crashes: 5
- Apr 9-10, maintenance visit by RUB engineer.
- Apr 23, synchronous self reset all channels: clock problem.
- Officers of Bundesgrenzschutz (BGS) started to use part of HUB as office.

May 1992:

- IAC crashes: 8
- May 11-15, maintenance visit by RUB engineers; May 19-22 emergency maintenance visit.
- change of baud rate between RDAS'es and IAC.
- hardware changes IAC (eeproms, digiboards, sdic board), new software IAC.exe (version 2.00)
- software changes of RDAS (3.30)

- digiboard 2 failed.
- GERESS DCF-77 clock defective and temporarily repaired by RUB engineers.
- vault inspection by SAG (subcontractor of Lahmeyer Inc.), no leaks found.

Jun. 1992:

- IAC crashes: 2
- thunderstorm damage on 10 channels
- June 3-5 and June 19-26, maintenance visits by RUB engineers.
- replacement DCF-77 clock installed in parallel to defective one (interface problems).
- installation of new digiboard 2
- power outage on HUB
- GERESS GRAND OPENING
- Warranty repairs by M. Browne (Teledyne-Geotech)
- new release of data acquisition software (SHI): DL2CB (3.9.1), CB2DB (3.9), MONITOR_DL (1.6).

Jul. 1992:

- IAC crashes: 1
- thunderstorm damage on 1 channel (Jul 3), 15 channels (Jul 10), and 6 channels (Jul 22)
- July 13-14 and July 27, emergency and regular maintenance visits by RUB engineers.
- new release of data acquisition software (SHI): SS2DL (2.1.3), MONITOR_PRGS (1.5.1), MRG (2.10), RUNMRG. Severe malfunction of MRG (2.10) documented.
- internet number for data analysis workstation
- upgrade of data request manager (DRM) by Krake Inc.

Aug. 1992:

- IAC crashes: 1
- thunderstorm damage of 2 channels (Aug 10), 11 channels (Aug 21), and 2 channels (Aug 26); field trip not necessary.
- extensive data gap testing under the direction of Teledyne.
- new release of data acquisition software (SHI): MRG (2.10.1), RUNMRG.
- power outage HUB
- power glitch at Bochum data center due to thunderstorm

Sep. 1992:

- IAC crashes: 2
- thunderstorm damage on 1 channel (field trip not necessary).
- data quality received at data center in Norway deteriorated to the point that data are useless (Sep 21). This correlates in time to extended outages on digiboard 2. The GERESS data received at data center in Kjeller remained unusable to the end of 1992.

Oct. 1992:

- thunderstorm damage of 10 stations (Oct 7).
- Oct 5-24, maintenance work at HUB.
- installation of improved thunderstorm protection equipment and power conditioning unit at each RDAS
- loading new RDAS configuration files (calibration sequence included)
- investigating calibration problems on D7 (repaired), D8, D9.
- installation of new DCF-77 master clock for GERESS
- Connection of Streckeisen (STS-2) at C2 (80 Hz) on Oct 8 (disconnection of BB-13 and GS-13 @ 120 Hz).
- start of reviewing regional event locations by analysts

Nov. 1992:

- Nov 25-26, maintenance work at HUB.
- supervision of digging near main cable route to HUB

Dec. 1992:

- Dec 14-18, maintenance work at HUB.
- installation of improved thunderstorm protection equipment at HUB.
 - BB-13 (vertical) reconnected
 - absolute time displayed on DCF-77 master clock and in the IAC different by minutes
 - Bochum: upgrade (version 1.19) data request manager (DRM by Krake Inc.) installed

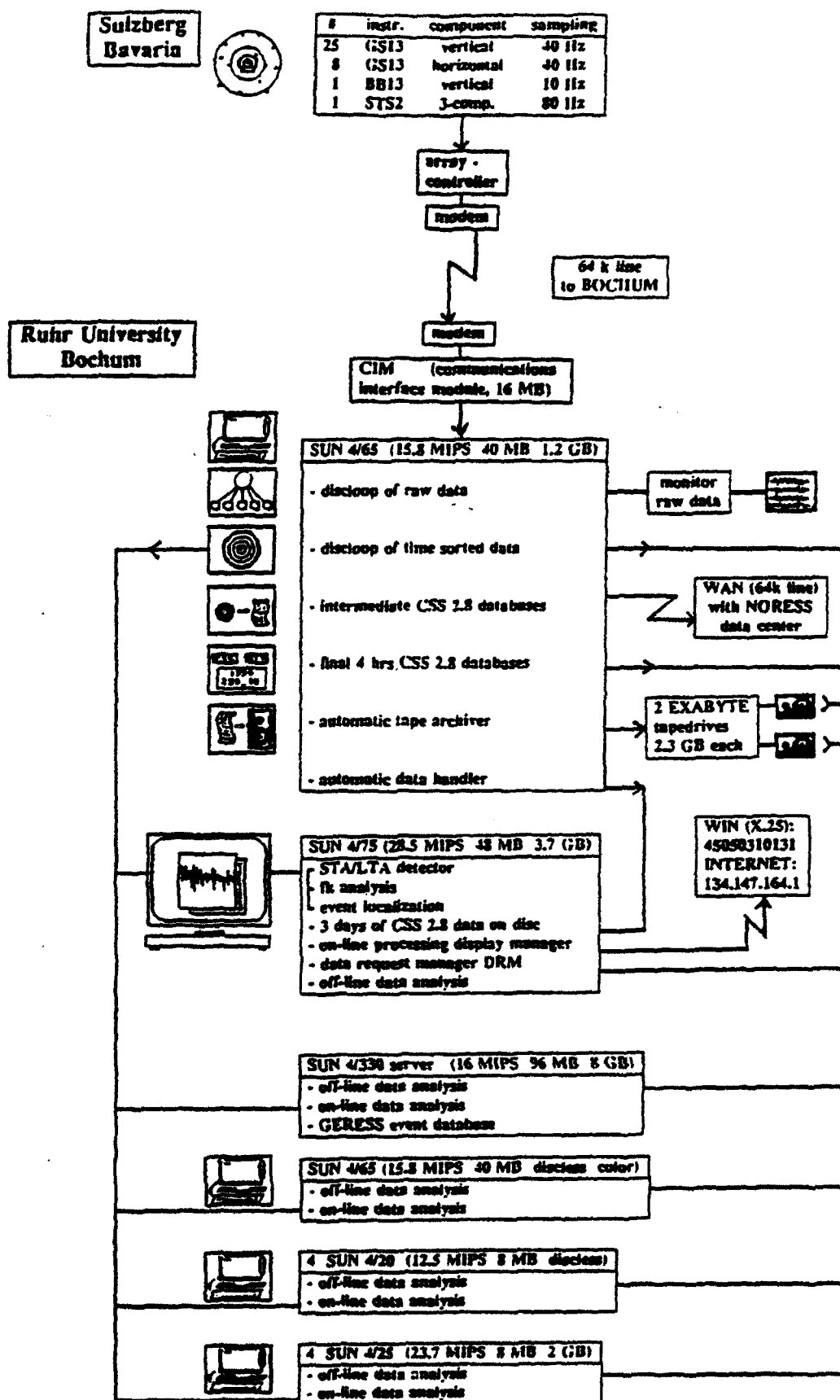


Figure 1-1: GERESS Observatory Bochum. Data Flow.

GERESS BOCHUM: AUTOMATIC LOCATIONS FOR 1992

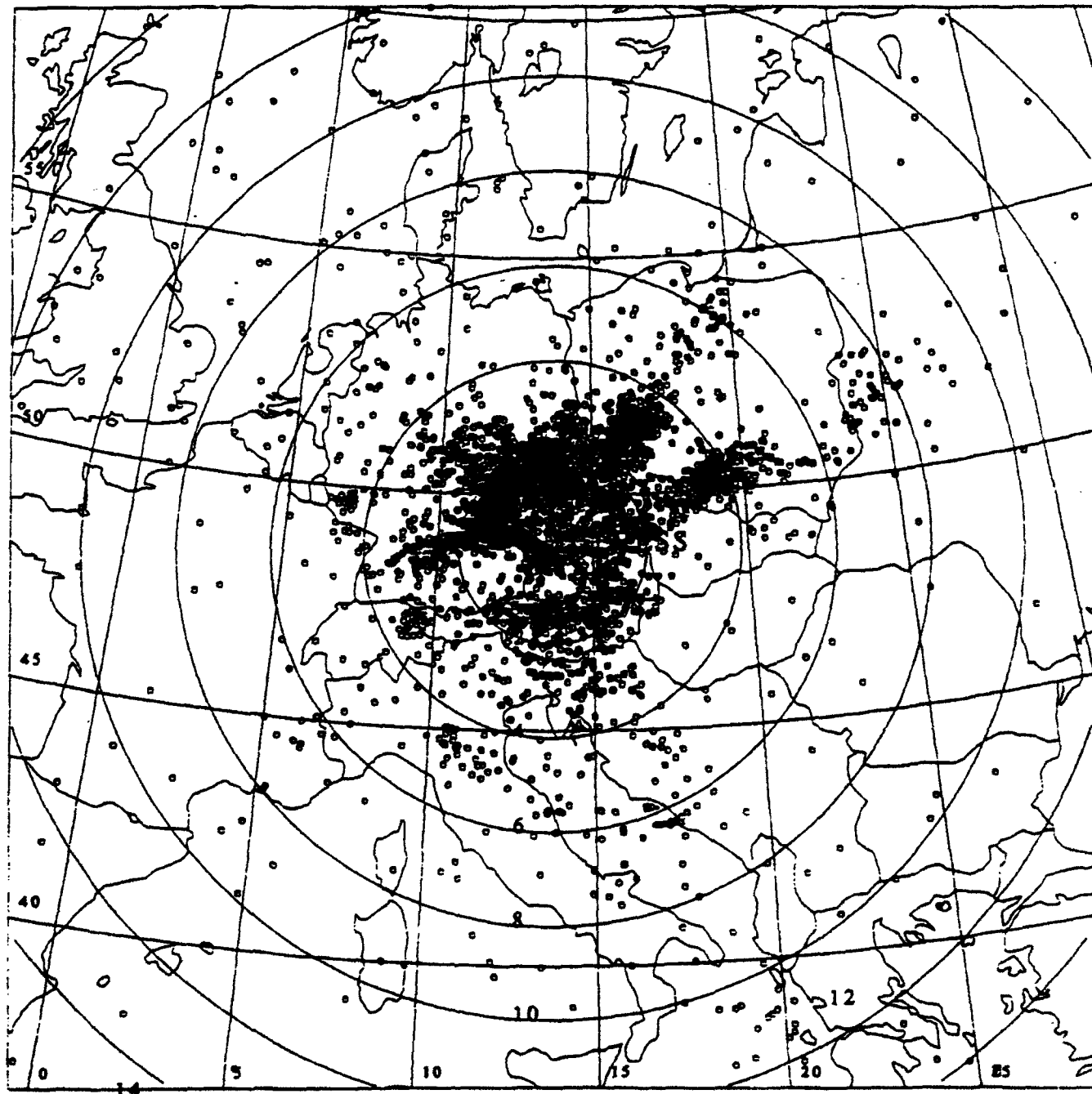


Figure 1-2

GERESS BOCHUM: ANALYST REVIEWED LOCATIONS OCT-DEC 19

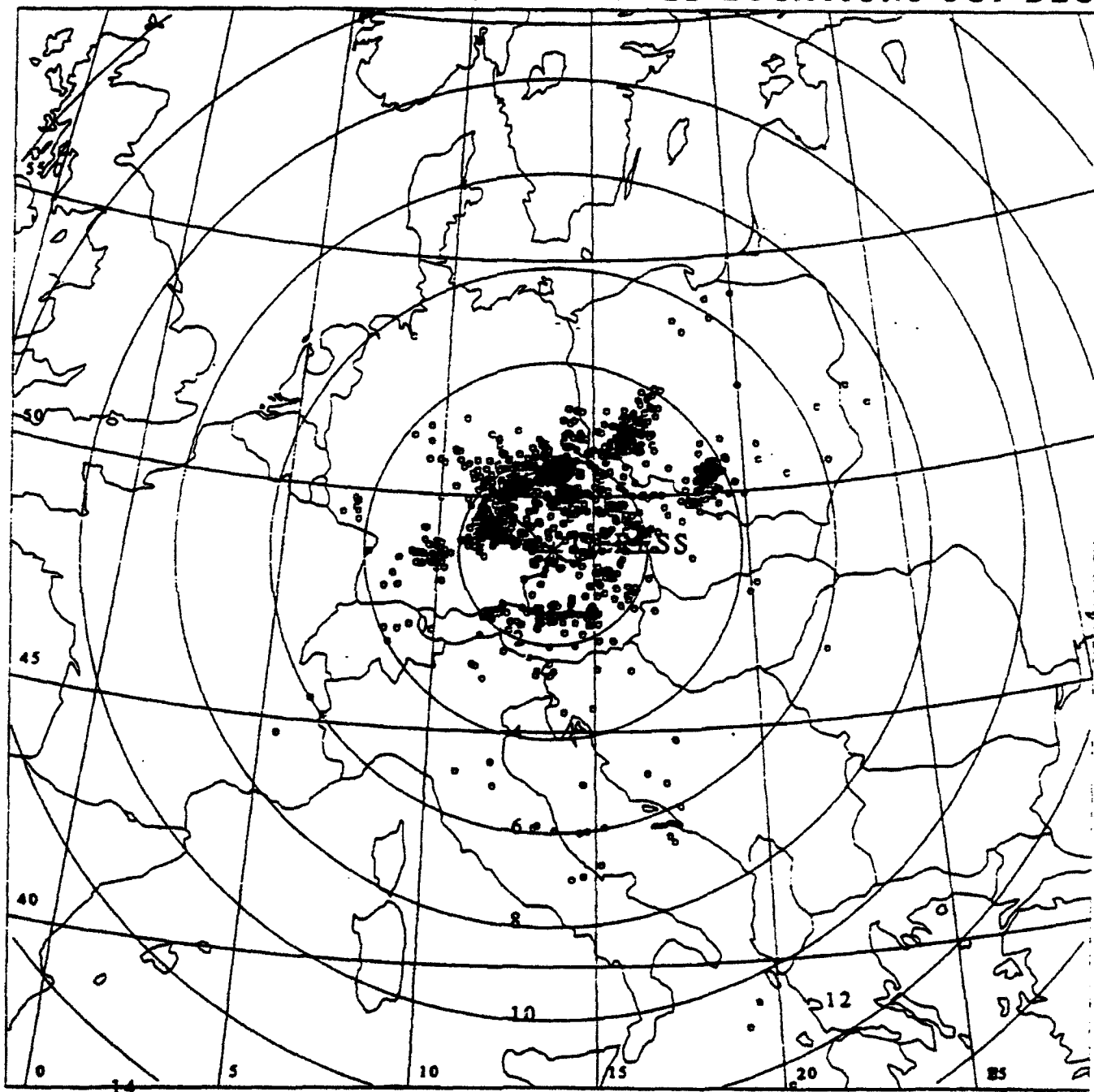
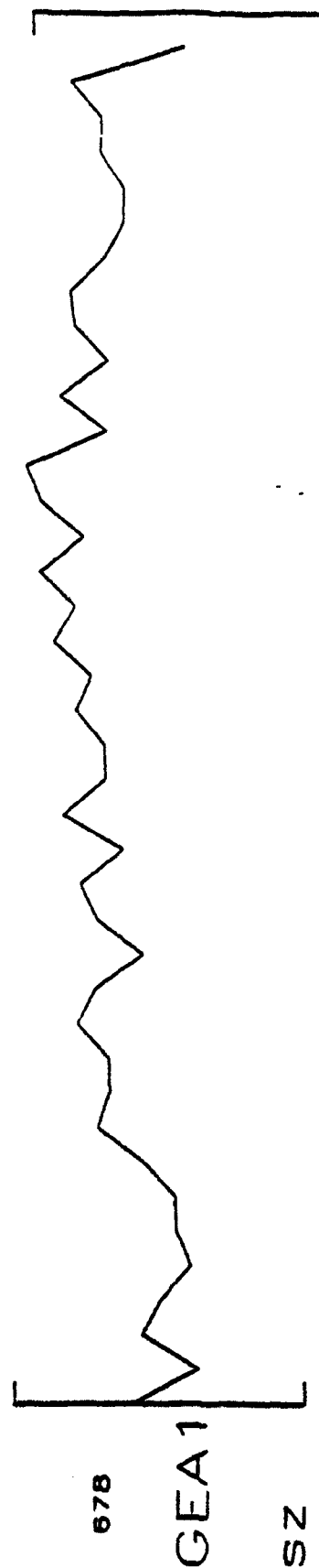


Figure 1-3



DATA OF APRIL 3, 1992 21:49:13 RECORDED ON MARCH 29, 1992

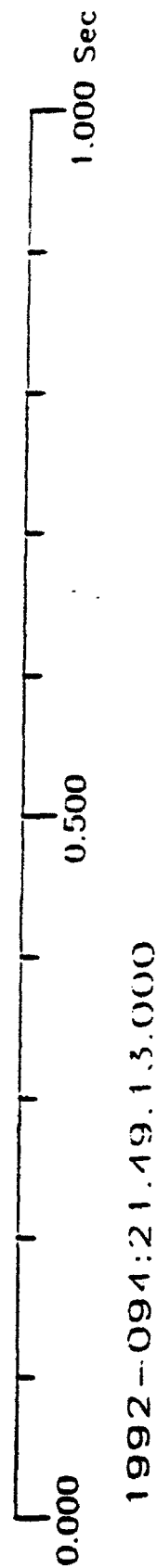


Figure 1-4

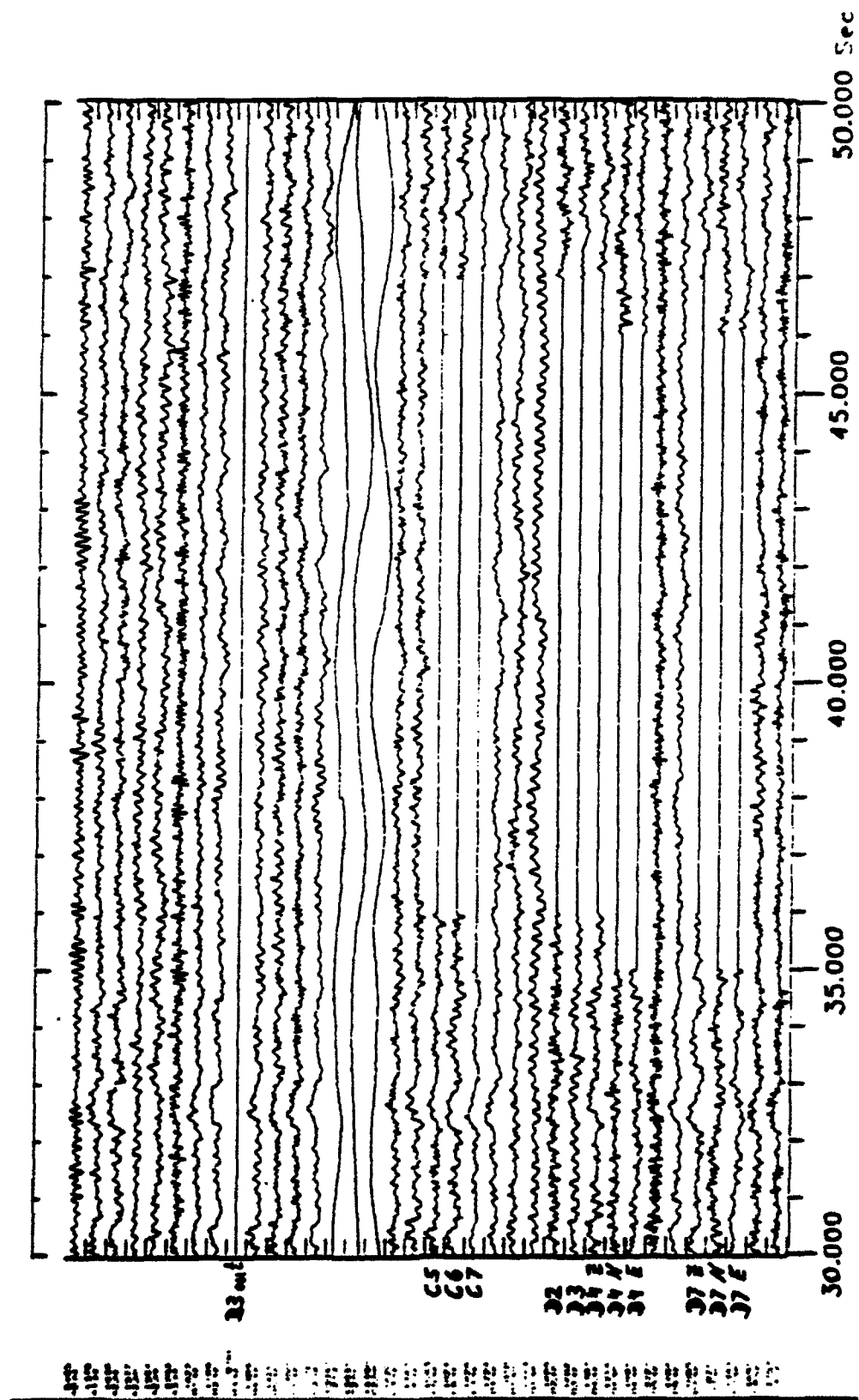


Figure 1-5: GERESS waveform display for all channels on December 11, 1992 11:42:00.
Note the "9-second" data gaps on all channels of digiboard 3 (B3 is out).

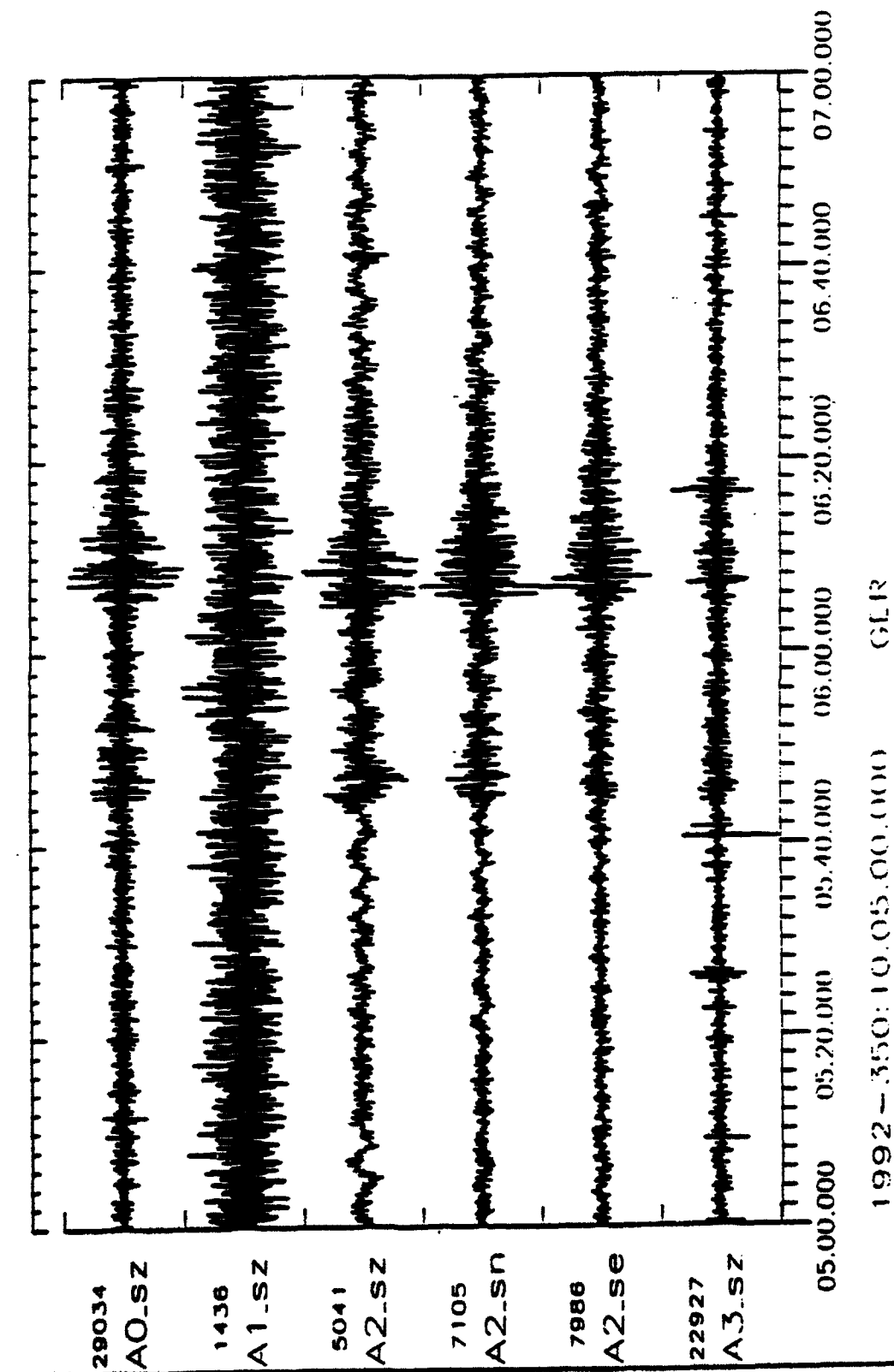


Figure 1-6: GERESS waveform display of A0 and A-ring for December 15, 1992 10:05:00. Note the artificial data on A1. Amplitudes on A0 and A3 are larger due to a site effect at these stations. Data on A1 consist obviously of electronic noise, and a seismic contribution to the data on this channel cannot be seen. The artificial data appeared after a power-on of the RDAS and vanished only after a manual reset from Bochum.

2. REPORT ON GERESS INSTRUMENT CALIBRATION

Jan Wüster

2.1 Abstract

GERESS local magnitudes have been observed to be systematically low by at least 0.5 magnitude units in comparison with neighbouring stations. In order to exclude the possibility that this effect is due to some sort of instrumental or procedural error, a thorough check on GERESS instrument calibration was performed in October and November 1992. Components of the system which were checked include: GS13 generator constant, transfer function and calibration coil motor constant, RDAS calibration signals, RDAS pre-amplification and A/D-conversion. Although several minor deviations from technical specifications were found, none of them can account for a systematic diminution of amplitudes by a factor of 2 or more. Consequently the low magnitudes need to be explained otherwise.

2.2 The Problem

At GERESS, Richter local magnitudes are determined from Wood-Anderson simulated traces (see e.g. Jost, 1992) using an amplitude-distance relationship for Western Europe (Nicolas, 1982.) To take advantage of the improved signal/noise ratio, standard M_L -values reported in the GERESS event lists are calculated from the vertical beam trace. Horizontal beams and a single horizontal station (GEC2) have also been used for comparison. The signal loss due to beam-forming was found to be 0.2 magnitude units on average (Schweitzer, pers. comm.) Even if this is taken into account, GERESS M_L -values are systematically low in comparison with neighbouring stations and networks.

The effect has been observed for some time by GERESS and GRF staff, it was studied quantitatively by Kradolfer (1992), who found that the M_L -values from GERESS were on the average 0.8 ± 0.3 magnitude units lower than the corresponding values calculated by the Swiss Seismological Service for a sample of 42 Swiss events from Nov 19 1991 to May 18 1992, although part of this difference could be attributed to the different procedures used for local magnitude determination. m_b -determinations at GERESS for teleseismic events also tend to be lower than the values reported by NEIC (Schweitzer, this report, chapter 3)

Before attributing these findings to external factors, we must make sure that any internal causes can be excluded. Therefore it was decided to check thoroughly all relevant components of the GERESS signal transmission system for compliance with technical specifications.

2.3 Routine calibration checks

Routine calibration checks are being performed every day between 03:00 and 03:13 UT. A calibration signal (4500 mV zero-to-peak nominal amplitude, 1 Hz frequency, 50 s duration) is being fed into all channels following a schedule published most recently in the GERESS status report of August '92 (Jost 1992.) [Note that 4500 mV is the nominal voltage value downloaded to the RDASs. For actual voltage values see below under 2..5.] In each seismometer the calibration signal drives a calibration coil in series with a capacitor, making the electrically induced velocity of the seismometer mass proportional to the applied voltage (Teledyne 1988, page 628/19.) Teledyne measured the transfer function $H(s)$ of the electrically driven seismometer (Horn 1990) and express them in terms of poles, zeros and gain [the gain being valid for the nominal calibration voltage values.] In theory, transfer functions of all GERESS GS13-channels should be identical, because effective generator constant, natural frequency and effective damping have been normalized to 2000 Vs/m, 1 Hz and 0.75 critical damping respectively. The amplitude of the transfer function evaluated at 1 Hz is $H(2\pi i \cdot 1 \text{ Hz}) = 70727.3 \text{ counts/Volt}$. This means that with $U_{cal} = 4.5 \text{ V}$ we expect to measure 318273 digital counts zero-to-peak. Table 2-1 shows the results of a comparison of amplitude values measured during a routine calibration on Oct 28 1992 with the theoretical values, giving the deviation in percent.

13 of 33 short period channels are within specifications ($\pm 1\%$), another 14 channels are within $\pm 5\%$ of the theoretical value. Deviation is not acceptable for channels D4.sz (-5.1%), D1.sz (-6.4%), D7.sz (-7.8%) and D1.sn (+12.2%). Values for D8.sz (factor 26.4) and D9.sz (factor 1/185.4) are drastically off. These drastic deviations are not observed in seismic signal or noise amplitudes and will be considered separately below in section 2..10. The percentage values in Table 2!-1 were checked on several days and were found to be quite stable. Daily fluctuations typically affect the second decimal place only.

It is concluded that although some channels are definitely outside specifications, GS13 overall channel sensitivity to electrical excitation at 1 Hz is as expected.

Table 2-1: Check on Calibration of GS13 40 Hz channels at
1992-302:03.00.00.000

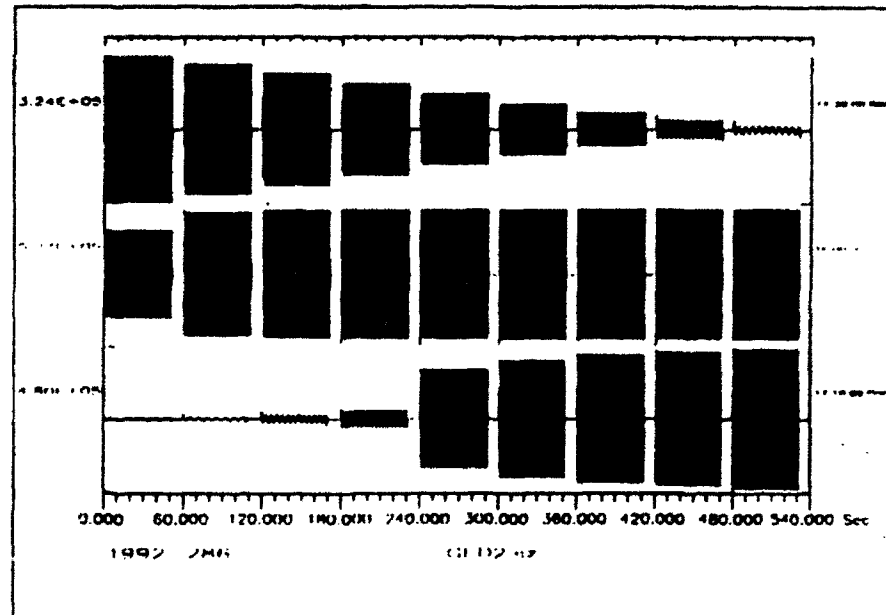
Vertical Channels, CALNORM = 318273

1	GEA0_sz	316598	=	-0.526	%
2	GEA1_sz	320279	=	0.630	%
3	GEA2_sz	311520	=	-2.12	%
4	GEA3_sz	320545	=	0.714	%
5	GEB1_sz	319350	=	0.338	%
6	GEB2_sz	316753	=	-0.478	%
7	GEB3_sz	309209	=	-2.85	%
8	GEB4_sz	319951	=	0.527	%
9	GEB5_sz	310433	=	-2.46	%
10	GEC1_sz	315426	=	-0.895	%
11	GEC2_sz	312798	=	-1.72	%
12	GEC3_sz	315587	=	-0.844	%
13	GEC4_sz	311976	=	-1.98	%
14	GEC5_sz	311985	=	-1.98	%
15	GEC6_sz	316194	=	-0.653	%
16	GEC7_sz	304366	=	-4.37	%
17	GED1_sz	297857	=	-6.41	%
18	GED2_sz	325289	=	2.20	%
19	GED3_sz	317074	=	-0.377	%
20	GED4_sz	302023	=	-5.11	%
21	GED5_sz	307657	=	-3.34	%
22	GED6_sz	318786	=	0.161	%
23	GED7_sz	293462	=	-7.80	%
24	GED8_sz	0.838861E+07	---	too big	for cal
25	GED9_sz	1717	---	too small	for cal

Horizontal Channels, CALNORM = 318273

26	GEA2_sn	318578	=	0.096	%
27	GEA2_se	315817	=	-0.772	%
28	GED1_sn	357015	=	12.17	%
29	GED1_se	314265	=	-1.26	%
30	GED4_sn	312781	=	-1.73	%
31	GED4_se	312670	=	-1.76	%
32	GED7_sn	309569	=	-2.73	%
33	GED7_se	308426	=	-3.09	%

Figure 2-1: Sinusoid signals of various frequencies and fixed amplitudes were applied to the calibration coil on channel GED2.sz:



2.4 Transfer functions

The GS13 sensitivity for ground velocity has a plateau for frequencies $> 1 \text{ Hz}$ and a descending flank for frequencies $< 1 \text{ Hz}$, the natural frequency of 1 Hz being the 3 dB point. The exact shape of the sensitivity curve in the transition region is relevant for local magnitude determination, because the largest amplitudes in the S-wavetrain often have periods around $T = 1 \text{ s}$.

An extended electrical calibration was performed on two randomly selected vertical channels (D2.sz and B5.sz.) To this end sinusoidal signals of various frequencies in the range $0.1 \dots 1 \text{ Hz}$ and a constant amplitude were applied to the calibration coils of the respective seismometers (Fig 2-1.) The signal amplitudes measured match the amplitude of the transfer function quite well (see Fig 2-2), except in the case of the calibration signal of 0.1 Hz , which is obviously not produced correctly by the RDAS signal generating unit (Figure 2-3.) The small sensitivity surplus at higher frequencies on Channel D2.sz is best brought out by a half-logarithmic plot (Figure 2-4.) Although measured values lie well on the theoretical curve (the solid line) at and below 1 Hz , they are significantly higher above 1 Hz . To adjust the theoretical curve to the measured value at 5 Hz , the static gain would need to be raised by 6% (the dashed line), at the expense of a poor fit in the 1 Hz -region. The second channel checked was found to be within specification over the whole frequency range covered (Figure 2-5.)

Figure 2-2: D2.sz calibration measurements and theoretical transfer function amplitude

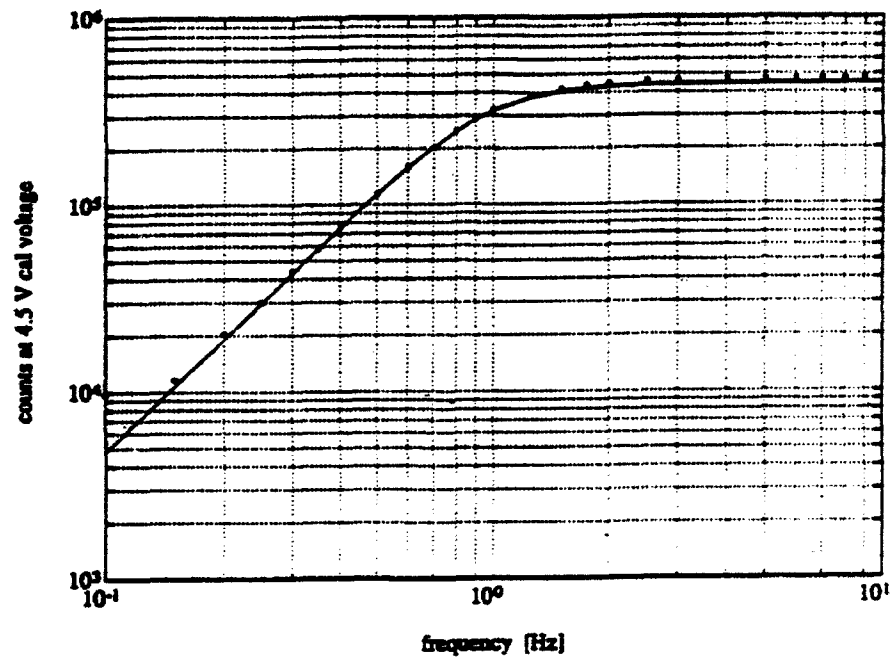


Figure 2-3: RDAS calibration signal at 0.1 Hz

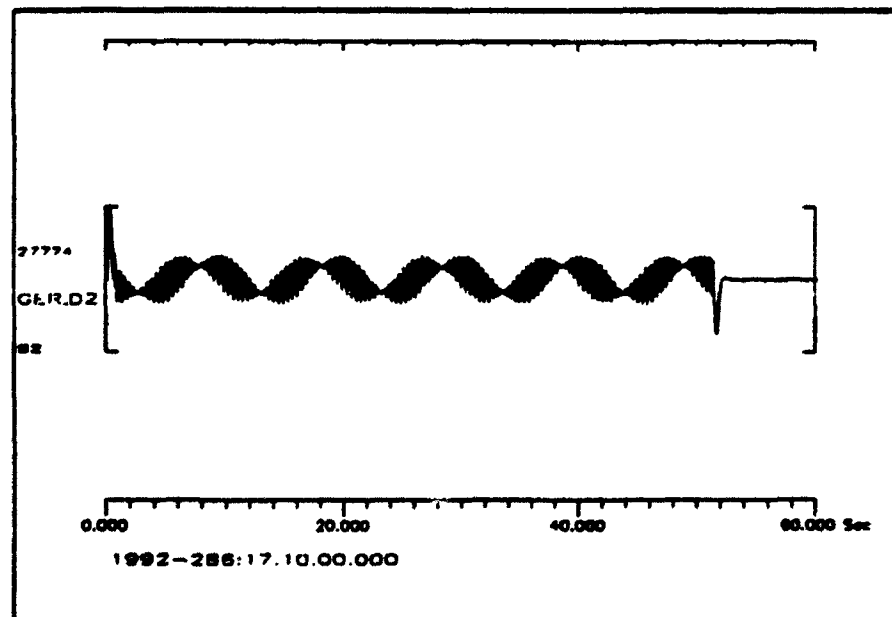


Figure 2-4: D2_sz calibration measurements and theoretical transfer function
amplitude: half-logarithmic scale

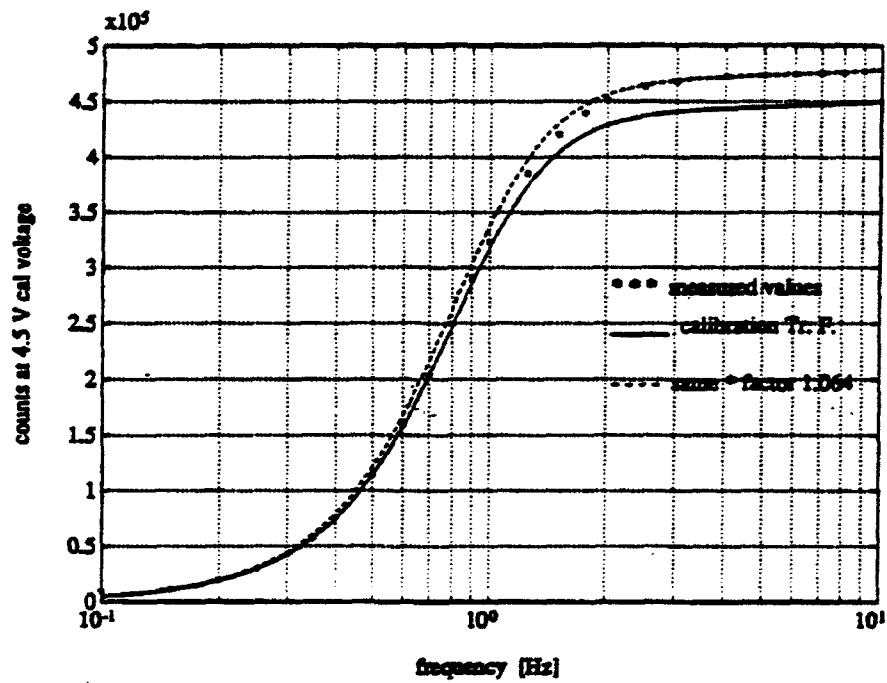
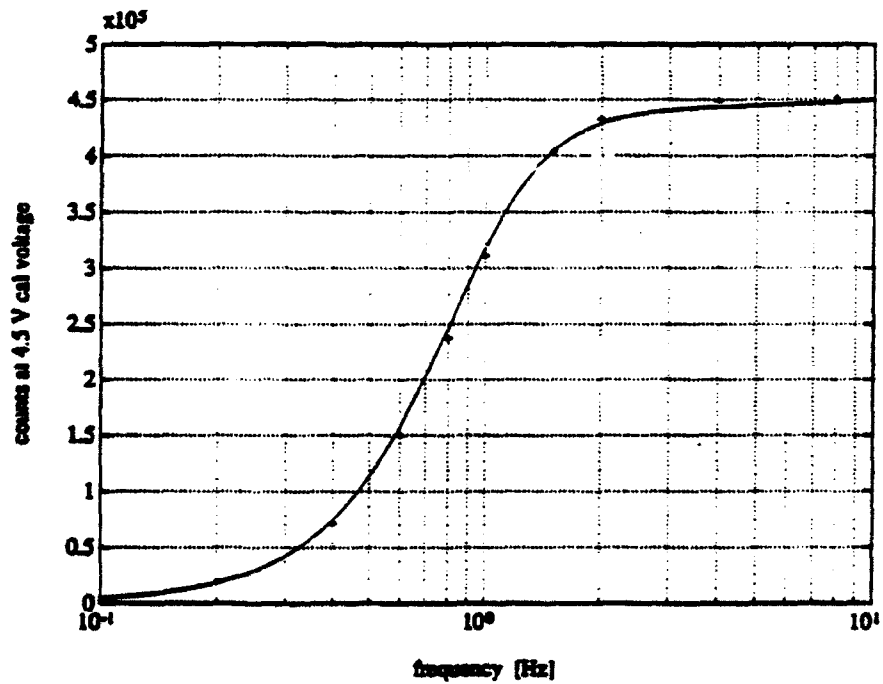


Figure 2-5: B5_sz calibration measurements and theoretical transfer function
amplitude



It is concluded that even when sensitivity matches the specified value closely at 1 Hz, this may not necessarily be true at other frequencies. But the 1 Hz-region is most important for M_L determination and hence the observed amplitude deviations at higher frequencies cannot be responsible for a systematic diminution of magnitudes.

2.5 RDAS signal generator

So far, channel sensitivity has been checked using electrical excitation by the RDAS signal generating unit. But this unit itself might be faulty or the electrical excitation might for some reason differ from seismic excitation. Therefore an effort was made to test all the components which determine the amplitude separately, starting with the signal generator.

Here, indeed, a major deviation was found: Calibration signals output by the RDAS were displayed on an oscilloscope in vaults D7, D8 and D9 at various voltage settings from 10 mV to 4500 mV and were consistently found to be too high by a factor of 2 (see Table 2!-2.) If, for example, the calibration voltage has been downloaded to be 100 mV_{0p}, the actual signal output will have an amplitude of 400 mV_{pp}, equivalent to 200 mV_{0p}. In order to explain the fact that overall sensitivity to electrical excitation has been found to be in conformity with the calibration transfer function supplied, while calibration signal amplitudes are obviously in error, it must be assumed, that the calibration transfer function has been originally derived using the excessive RDAS signal amplitudes. Electrical excitation without use of the RDAS signal generator is considered below in section 2..9.

A side result of the checks on the signal generators is, that the peculiarities observed in routine calibration (see section 2..3) on channels D8.sz and D9.sz are not caused by the signal generators.

2.6 Pre-amplifier and A/D-converter

Pre-amplification and A/D-converting stages were not checked separately but as a unit. Calibration signals of known amplitudes were fed directly into the RDAS signal input ports on channels D8.sz and D9.sz, the seismometer being disconnected. Amplitudes measured on the recorded trace (in digital counts) were converted to signal input levels using the specified A/D-converter LSB = 2.3841857 μ V/count and the pre-amplification factor of V = 31.6228 (30 dB.) The results are shown in Table 2!-2. Calculated input signal levels (zero-to-peak) are close to the signal amplitudes measured with an oscilloscope (zero-to-peak), as expected. Oscilloscope measurements are only exact up to $\pm 10\%$, but if we assume, that the output of the signal generators is *exactly* twice the value specified (see above under 2!-2) there is less than 2% deviation between nominal amplitudes times 2 and measured amplitudes (assuming

Table 2-2: Calibration signal amplitudes at 1 Hz

channel	nominal amp [mV _{op}]	measured amp [mV _{op}] ± 10%	max trace amp dig. counts _{op}	calc. input amp [mV _{op}]
D9.sz	10	25	$2.612 \cdot 10^5$	19.693
	20	40	$5.262 \cdot 10^5$	39.673
	40	85	$1.048 \cdot 10^6$	79.014
	60	120	$1.571 \cdot 10^6$	118.45
	80	165	$2.097 \cdot 10^6$	158.10
	100	210	$2.651 \cdot 10^6$	199.87
D8.sz	40	80	$1.049 \cdot 10^6$	79.104
	60	120	$1.5731 \cdot 10^6$	118.603
	80	160	$2.0983 \cdot 10^6$	158.200
	100	200	$2.6523 \cdot 10^6$	199.969

specified LSB and V.) The fact that all deviations are negative indicates, that either the signal generator output level multiplied by 2 or LSB and V are about 1% lower than expected on the two channels checked.

It is concluded that the pre-amplification and A/D-conversion stages of the RDAS are not responsible for a diminution of magnitudes. Also, calibration irregularities observed on channels D8.sz and D9.sz (section 2.3) are not due to these stages, they were reproduced after changing the respective RDAS A/D-converter card.

2.7 Seismometer generator constant

Weight-lifting tests were performed on channels D7.sz, D8.sz and D9.sz. The results could only be used qualitatively to confirm that generator constants at D8 and D9 (showing irregularities in calibration) do not drastically differ from D7 (not showing irregularities.) An indirect method was used to confirm the specified GS13 generator constant of 2000 Vs/m. An STS2-seismometer with a specified generator constant of 1500 Vs/m has been temporarily installed in the GEC2B vault. Its 3-component output is recorded on the C2.hn, .hz and .he high frequency channels, and the STS2-C2.hz trace can be compared to the GS13-C2.sz trace measured at the GEC2A vault. The STS2 transfer function, however, is flat to velocity up to a period of $T = 120s$, so the traces cannot be compared directly (Figure 2-6.) But from each of the different traces a Wood/Anderson trace can be simulated using suitable IIR filters constructed on the basis of the specified transfer functions and generator constants.

Figure 2-6 shows the maximum S-wavegroup amplitudes of an event from Switzerland, from which M_L would be determined. The upper 2 traces are the original STS2 and GS13 traces, the lower 2 traces are the simulated Wood/Anderson traces. The latter are indistinguishable in signal shape, but

Figure 2-6: Time-window containing the S-wavegroup maximum amplitude of an event from Switzerland. Upper two traces: STS2 and GS13 original seismograms. Lower two traces: Wood/Anderson traces simulated from STS2 and GS13, respectively: the lower traces are indistinguishable except for a 7% difference in static gain.

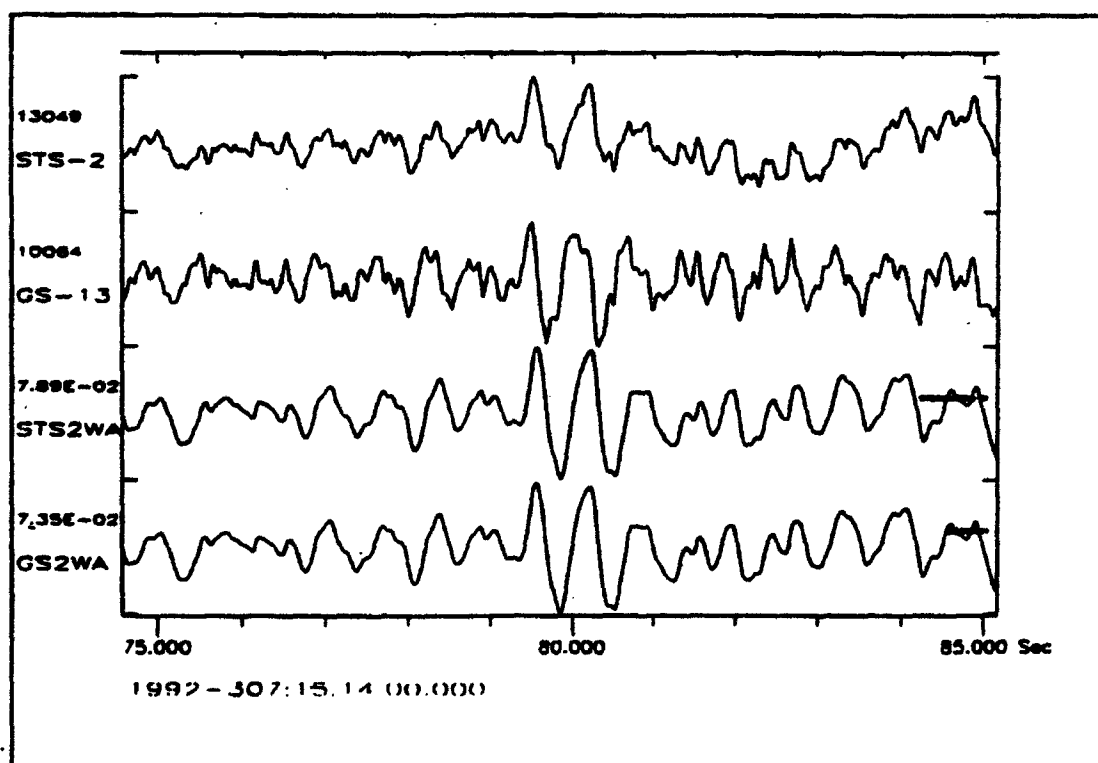
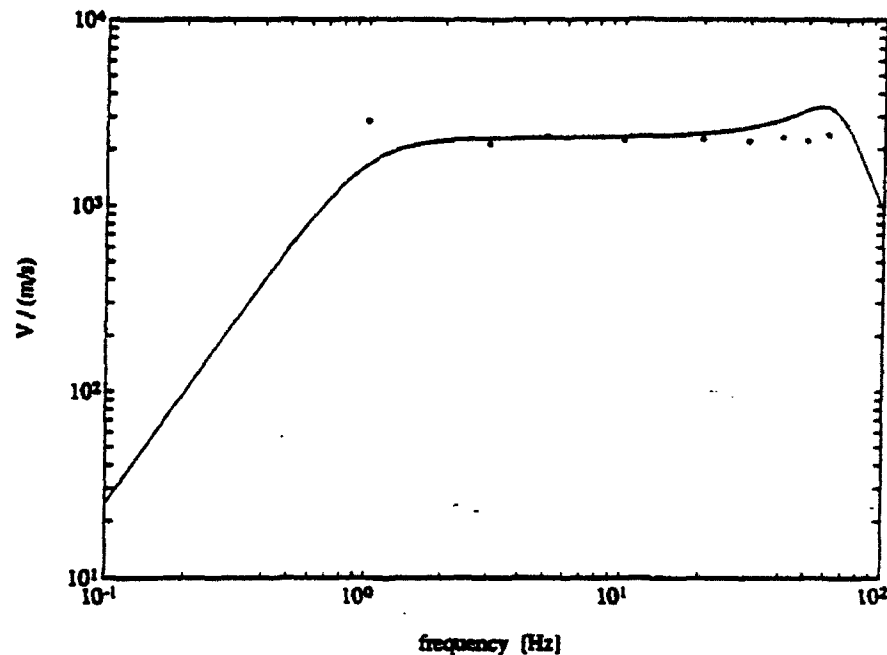


Figure 2-7: GS13 sensitivity measured on shaking table without output network



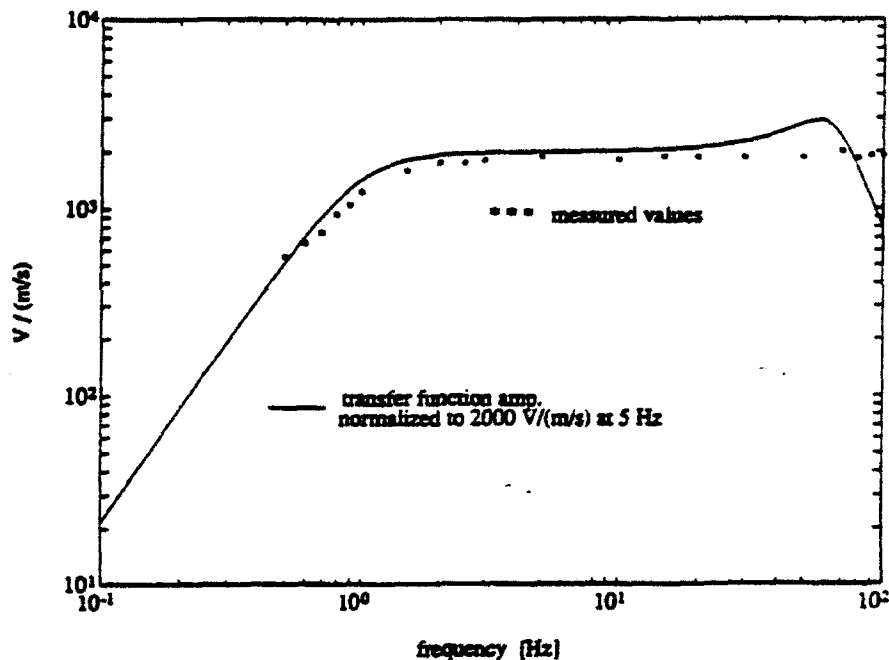
there is a difference in measured zero-to-peak maximum amplitude in mm, the trace simulated from STS2 yielding a value approximately 7% higher. Even before the substitution of the STS2 for the original GS13 instrument on C2_hz, this channel yielded approximately 10% higher amplitude values in seismograms, an effect which was not observed in electrical calibration. It is concluded that the performances of STS2 and GS13 reciprocally support each other and that the generator constants of the two instruments are within 10% of specifications.

2.8 Shaking table experiments

The vertical GS13 seismometer with serial No. 181, formerly deployed in vault GEA2, was shipped to Bochum and subjected to some shaking table tests. Setup and performance of these experiments followed Hinzen (1979). By means of the shaking table it is possible to determine seismometer output as a function of ground movement, i.e. perform a seismic calibration. In our case, output voltage maximum amplitude was set in relation to ground velocity maximum amplitude. This velocity sensitivity has the unit $V/(m/s) = Vs/m$ and is identical to the seismometer generator constant in the plateau well above the natural frequency.

In the first series of tests the seismometer coil output was measured directly, not using the resistor network normally employed (Figure 2-7.) The

Figure 2-8: GS13 sensitivity measured on shaking table with output network

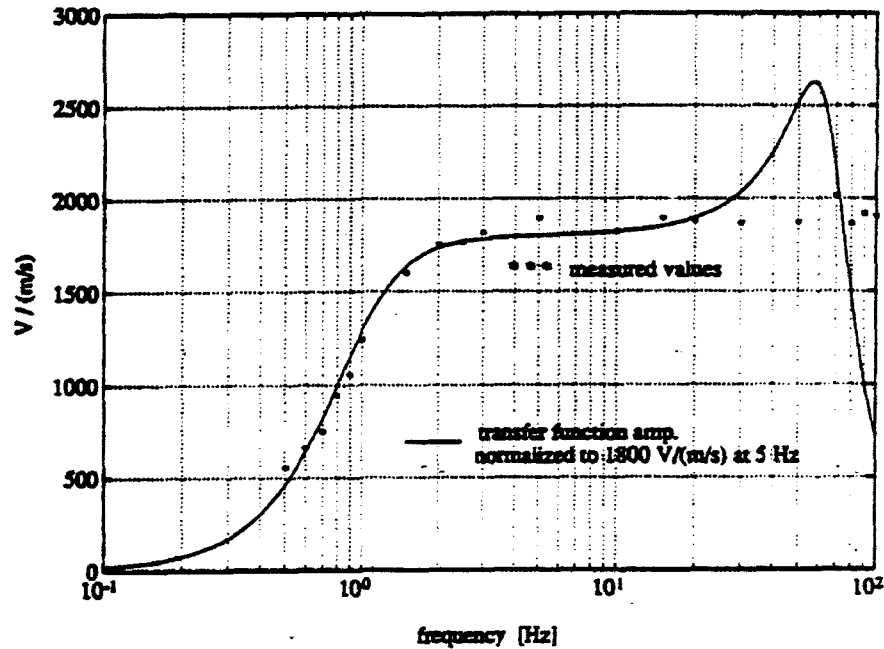


system is underdamped, but values to the right of 1 Hz lie well on the theoretical curve calculated using the GS13 transfer function and the "native" generator constant of the instrument No. 181, $G_k = 2316 \text{ Vs/m}$ (Horn. 1990). Note that the broad resonance at 57 Hz is not observed.

The function of the output resistor network is to normalize both effective damping λ_r and effective generator constant G_e to convenient values for all instruments in a set (Teledyne 1988, page 628/19.) According to Horn (1990), the effective values for all GERESS GS13 seismometers are set to $\lambda_r = 0.775 \cdot \text{critical}$ and $G_e = 2000 \text{ Vs/m}$ respectively. In the second series of tests the seismometer coil was connected via the output resistor network. Figure 2-8 shows that the measured values lie significantly below the theoretical curve calculated using $G = 2000 \text{ Vs/m}$. A reasonable fit is achieved assuming $G = 1800 \text{ Vs/m}$ as shown in Figure 2-9 in linear scale. Neither the substantial resonance at 57 Hz nor the sharp drop at 80 Hz are observed. There are hints of small resonances at 5 and 70 Hz , but this question should be addressed in more detail after some imperfections of the experimental setup have been removed.

It is concluded, that the sensitivity to ground velocity of the seismometer under study follows the amplitude of the transfer function specified by the manufacturer below 20 Hz . Above 20 Hz the sensitivity remains flat to velocity contrary to the transfer function supplied by the manufacturer, which has a broad resonance peak between 30 and 70 Hz . The measured effective generator constant is 10 % below specification.

Figure 2-9: GS13 transfer function amplitude fitted to measured sensitivity values



2.9 Electrical excitation

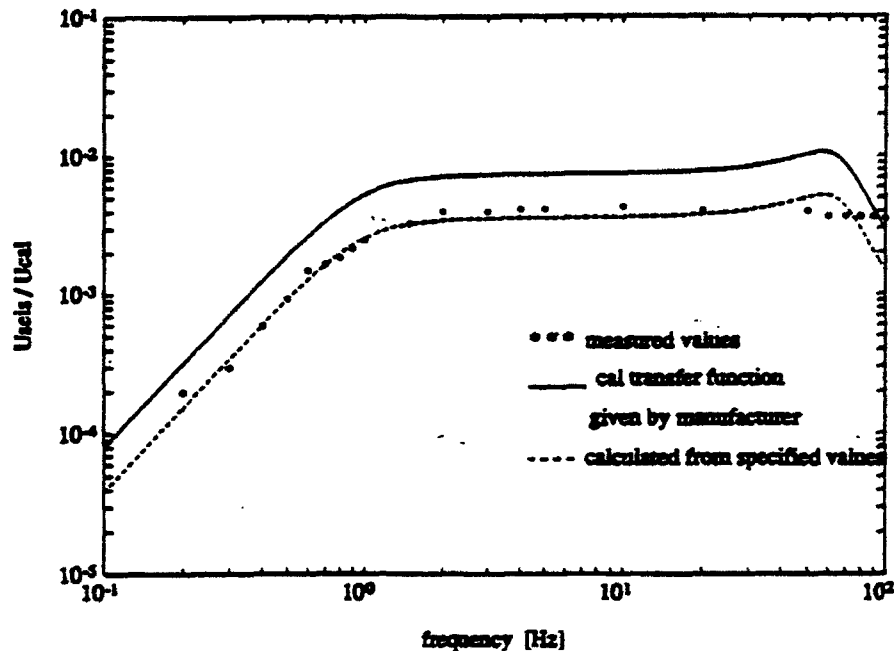
In order to prove the hypothesis on the calibration transfer functions in section 2.5, the functionality of the calibration coil was tested independently of the RDAS calibration signal generator. The calibration coil is driven in series with a $2 \mu F$ capacitor, which makes the velocity of the seismometer mass induced by the calibration coil proportional to the applied calibration voltage. The proportionality constant calculated according to Teledyne (1988, page 628/10) is

$$VELSENS = \frac{C \cdot M_c}{m} = \frac{2.0 \mu F \cdot 4.5 \frac{N}{A}}{5 kg} = 1.8 \frac{\mu m/s}{V}$$

with the capacity C , the calibration coil motor constant M_c and the suspended mass m .

Now the seismometer can be excited applying sinusoidal signals of various frequencies with an amplitude of U_{cal} , seismometer output amplitudes U_{seis} are measured. Ratios U_{seis}/U_{cal} thus determined can be compared to theoretical ratios obtained using constant $VELSENS$ and the seismometer transfer function on one hand and the calibration transfer function on the other hand. Figure 2-10 shows, that the measured values follow the first curve (dashed line) reasonably well, while the latter curve (solid line) is definitively too high by a factor of 2. Note that again the resonance at 57 Hz is not observed.

Figure 2-10: GS13 electrical excitation, voltage ratio measured and calculated



Thus it has been confirmed that the calibration transfer function supplied by the manufacturer must only be used in connection with the excessive RDAS cal signal amplitudes. The problem must be born in mind in case the RDAS is used to calibrate a different seismometer, or the GS13 is calibrated without the RDAS. This peculiarity has no effect on earthquake magnitude determinations.

2.10 Calibration Irregularities

The channels D8.sz and D9.sz were found to be drastically off in routine calibrations (see above 2.3.) RDAS signal generators, pre-amplifiers and A/D-converters could be excluded as sources of the problem (above under 2.5 and 2.6.) In the case of D9 the problem (amplitudes too low) disappeared when the seismometer was exchanged with the one previously deployed at A2.sz. When opportunity arises, the seismometer should be checked at Bochum and sent to the manufacturer for repair, if no fix can be found. In the case of D8 (amplitudes too high) the problem persisted even after the exchange of the seismometer. Here the reason could be, that the RDAS does not make the necessary internal connection, which corresponds to a jumper connection between pins H and U of the GS13 connector required in calibration mode (Teledyne 1988, page 628/10.) In this case the calibration coil would be driven directly by the signal generator without a capacitor in series. An

exchange of the appropriate RDAS board should fix the problem. The irregularities described occur in calibration mode only and are irrelevant for magnitude determination.

2.11 Conclusions

The following is a resumé of findings encountered in the check on GERESS instrument calibration:

1. Only 13 of 33 channels are within 1% of specification on overall sensitivity at 1 Hz, another 14 channels are within 5%. 4 channels are seriously off, 2 channels are drastically off. In the case of the latter, the problem is restricted to calibration mode.
2. The RDAS calibration signal generator produces sinusoidal signals with twice the nominal amplitude. Also, it cannot produce frequencies below 0.2 Hz.
3. Even though the calibration at 1 Hz is within specifications, a deviation of +6% has been observed at higher frequencies in one out of 2 channels checked.
4. In two spot-checks, LSB and pre-amplification factor were found to be within 2% of specification.
5. The effective generator-constant of the GS13-seismometer at GEC2.sz was found to be within 10% of specification by comparison with an STS2 seismometer, which was operated in parallel.
6. In a shaking-table experiment with the GS13-seismometer formerly installed at GEA2.sz, the effective generator constant G_e was found to be 10% below specification, although the "native" generator constant G_k was found to be as specified.
7. In an experiment driving the seismometer with a voltage applied to the calibration coil in series with a capacitor, the sensitivity of induced velocity to voltage applied was found to be as specified. The calibration transfer function supplied by the manufacturer gives excessive sensitivities by a factor of 2. This effect counteracts the elevated RDAS calibration signals mentioned above.
8. The resonance between 50 and 60 Hz and the sharp drop above 70 Hz in the amplitude of the GS13 transfer function given by Tele-dyne are not observed. Instead, the plateau extends to 100 Hz.

None of these findings justifies the assumption, that amplitudes are systematically diminished by the GERESS signal processing system to a degree necessary to explain the low local magnitudes.

Acknowledgements

Field measurements at the vaults were performed by Bernhard Klotz and Lothar Kühne. The latter and Andreas Müller assisted with the shaking table experiments. Their help is gratefully acknowledged.

References

Hinzen, Klaus-Günter (1979)

Untersuchungen zum Anwendungsbereich einer Schütteltischanlage bei der Kalibrierung von Seismometern und Geophonen unter Verwendung verschiedener Anregungsarten. Diplomarbeit, Institute of Geophysics, Ruhr-University Bochum, Germany, July 1979.

Horn, Charles (1990)

CD station channel transfer characteristics. Undated and unsigned manuscript contained in a letter by Charles Horn (Teledyne Geotech) to H.-P. Harjes (Institute of Geophysics, Ruhr-University Bochum) dated Sept 11 1990. The letter also contains data sheets on individual GERESS instruments.

Jost, Michael L. (1992)

Current status and results of the GERESS data center in Bochum. Proceedings of the GERESS symposium, Waldkirchen, June 22-24 1992.

Kradolfer, Urs (1992)

Recent seismicity in Switzerland as located by the Swiss network and the GERESS array. Proceedings of the GERESS symposium, Waldkirchen, June 22-24 1992.

Nicolas, M., Massinon, B., Mechler, P. & Bouchon, M. (1982)

Attenuation of regional phases in Western Europe. *Bull. Seis. Soc. Am.* **72** 2089-2106.

Teledyne Geotech (1988)

Operation and Maintenance Manual. Portable Short-Period Seismometer, Model GS-13. Stock No. 990-55400-9800, Teledyne Geotech, 3401 Shiloh Rd., Garland, Texas 75041, USA.

3. TELESEISMIC DETECTION AND LOCATION CAPABILITIES OF THE GERESS ARRAY

Johannes Schweitzer

3.1 Introduction

Since evaluation of the GSETT-2 experiment (Schweitzer, 1992; Schweitzer et al. 1992) in 1991, it is known, that GERESS is the most sensitive seismological station in Central Europe. In October 1991, the GERESS group in Bochum started to reanalyse teleseismic onsets detected automatically with the GERESS array. The reanalysed parameters were sent to international data centers (NEIC, EMSC) and to any interested seismic station. The reanalysis was necessary because the automatically picked onset times, phase identifications, and the results of the automatic fk-analysis (ray parameters and azimuth's) were often erroneous.

Since October 18, 1991, the GERESS onsets were associated to events by NEIC as seen in the weekly or monthly Earthquake Data Report's (EDR's) of NEIC. An evaluation of GERESS contribution gives some informations about the teleseismic detection capability of the array and the bias of observed parameters such as azimuth, ray parameter, onset time, and amplitude.

In the following, the GERESS contribution to the EDR's (monthly listings) from October 18, 1991 to August 1992 and to the EDR's (weekly listings) from September 1992 to February 1993 is evaluated. Fig. 3-1 shows all events for which NEIC associated a GERESS phase. The GERESS contributions can be compared with those of other arrays or stations which contributed routinely to NEIC. In this study, the contributions of the Yellowknife array (YKA) in Northern Canada and the contribution of the single seismic station Kašperské Hory (KHC) located in the Bohemian Massif in the Czech Republic in the vicinity (33 km) of GERESS were used for comparison.

3.2 GERESS detection capabilities

Every event in the range between 20° and 180° epicentral distance for which NEIC reported a body wave magnitude m_b was defined as an observable teleseismic event. (Note that for each station under consideration, the observable events are different.) On average, GERESS reported 44.6 %, YKA 59.3 %, and KHC 26.2 % of these events. The differences between GERESS and KHC can be explained by an increase of the signal to noise ratio (SNR) for small onsets due to

beam forming for the GERESS data and by the general better noise conditions at the GERESS site.

At first, the seasonal pattern was investigated. Fig. 3-2 shows, how the detection probability of GERESS and of YKA changed with respect to the day of year from October 18, 1991 to February 11, 1993. The detection capability was averaged for 10 days. The crosses show the detection capability of GERESS and the triangles the detection capability of YKA. The two arrays differ: YKA shows a decrease of its detection capability of about 25 % for the summer time, when the Great Slave Lake is open. In the late summer and early autumn, YKA is clearly less sensitive than GERESS, for which such a seasonal effect is not observable. The decrease of the detection probability of GERESS between the 70'th and 90'th day of the year was caused by a larger outage of GERESS. The single station KHC situated in the same geological unit as GERESS shows a similar pattern (Fig. 3-3).

Fig. 3-4 shows the percentage of events detected by the three seismic observatories with respect to epicentral distance. Once again, triangles are for YKA, crosses for GERESS, and circles for KHC. The decrease for GERESS and KHC for events between 60° and 70° epicentral distance around the North Pacific subduction zones is due to the large number of smaller events ($m_b < 4.5$). These events were detected by local and regional stations and NEIC could determine a m_b value. Clearly seen is the decrease in and around the Earth's shadow, but also the relatively high detection capability for PKP phases between 135° and 155° epicentral distance. Surprising, the highest detection capability in this plot can be found for PKP onsets at the GERESS site. This partly reflects the low network detection capability for smaller events ($m_b < 4.5$) in the South West Pacific. It also demonstrates, that sensitive seismic stations in epicentral distances around the PKP caustic can improve the detection capability drastically. GERESS reported many PKP phases in the investigated time range, which could not be associated to any event by NEIC.

At next, the detection capability of GERESS during the time of day was investigated. Fig. 3-5 shows the detection probability of GERESS (upper line) and of KHC (lower line) with respect to local time for the investigated time period. A decrease of the detection capability at daylight hours can be observed at both stations. This is the influence of an increase of man made noise and/or of the local and regional artificial seismicity which masks smaller teleseismic onsets. This interpretation of the observed effect is confirmed by Fig. 3-6, where the detection probability during the whole day is shown only for working days. Now a decrease of the detection probability of about 8 % for GERESS and about 5 % for KHC at daylight hours can be observed.

3.3 GERESS mislocation vectors

GERESS as a small aperture array (~ 4 km) has only a limited resolution for estimating slowness and backazimuth of teleseismic onsets. After association of the reported onsets to located events by NEIC, the reported values which include slowness (p) and backazimuth (BAZ), can be compared with the theoretical p and BAZ values. NEIC locations were used to calculate the epicentral distance and the theoretical BAZ . The IASP91 travel time tables (Kennett and Engdahl, 1991) were used to calculate the theoretical slowness of the first arrival (P , P_{diff} , PKP) from the theoretical epicentral distance and the reported depth (NEIC). To reduce the scatter all p and BAZ values of first arrivals with a travel time residual $|t_{obs} - t_{theo}| > 3.0$ sec and with a slowness mislocation vector in the slowness space of more than ± 4.0 sec/ $^\circ$ were omitted. With the first arrivals investigated during the GSETT-2 period (Schweitzer, 1992) and the onsets reported between October 18, 1991 and February 18, 1993, a total of 3330 slowness and backazimuth values could be compared with their theoretical values. The theoretical coverage of the slowness space of these arrivals can be seen in Fig. 3-7. This figure should be compared with Fig. 3-1 to locate well observed source regions in the slowness space.

Fig. 3-8 shows the observed mislocation vectors in the slowness space. The mislocation vectors have been averaged for bins with a width for p of 1 sec/ $^\circ$ and a width for BAZ of 10° . In the central part, the width of the bins for BAZ was increased to 20° and 30° . The theoretical value is always indicated by a circle. The mean slowness residual of all observations is $dp = -0.45$ sec/ $^\circ$ with a standard deviation $\sigma_{dp} = 1.15$ sec/ $^\circ$ and the mean BAZ residual is $dBAZ = 4.76^\circ$ with a standard deviation of $\sigma_{dBAZ} = 22.80^\circ$. Because of the large standard deviations, the data have to be reduced to the most significant observations.

Fig 3-9 now shows only mislocation vectors, which were estimated from at least 5 observations. It is obvious that the remaining mislocation vectors show systematic effects. The BAZ residuals change between positive residuals observed from $\sim 350^\circ$ to $\sim 30^\circ$ and from $\sim 90^\circ$ to $\sim 170^\circ$ and negative residuals from $\sim 40^\circ$ to $\sim 80^\circ$ and from $\sim 180^\circ$ to $\sim 340^\circ$. The observed slowness values are systematically too small with respect to IASP91. At the moment is not clear, how far the small p values are an effect of the Earth's structure or an artefact of the implemented fk-analysis, the array configuration, the local geology, and the topography at the array site.

Since January 1992, YKA and GERESS exchange regularly their phase readings via electronic mail. Therefore, the reported p and BAZ values of YKA are available at Bochum and we can compare them with their theoretical values respectively. Fig. 3-10 shows the YKA mislocation vectors of 3679 onsets for the time period between January 6, 1992 and February 18, 1993. The mean slowness error of YKA is 0.02 sec/ $^\circ$ with a standard deviation of $\sigma_{dp} = 0.46$ sec/ $^\circ$ and the mean BAZ error is 0.61° with a standard deviation of $\sigma_{dBAZ} = 5.31^\circ$. Contrary to GERESS, YKA had been calibrated and therefore only corrected p and BAZ

values were reported and its remaining mislocation vectors are much smaller than for GERESS. In addition, the resolution of the larger YKA array is much better.

Most of the mislocation vectors of GERESS in Fig. 3-9 are small with respect to their standard deviation. Therefore it is not useful, to correct the observed p and BAZ values with these mislocation vectors. Fig. 3-11 only shows the mislocation vectors for which the theoretical value is outside the error ellipses calculated with the standard deviations of these vectors respectively. At the moment, the number of the remaining mislocation vectors with "significant" deviations from the theoretical p and BAZ values is too small, to use them routinely in the daily reanalysis work. Until a more complete set of mislocation vectors becomes available, the mean standard deviations ($\sigma_{dp} = 1.15 \text{ sec/}^\circ$ and $\sigma_{dBAZ} = 22.80^\circ$) can be used to weight the GERESS slowness and backazimuth values in location routines, which use this additional information (e. g. IMS).

3.4 Travel time and amplitude residuals of GERESS

In this chapter, the observed bias of absolute onset times and amplitudes at GERESS are discussed. To calculate a mean travel time residual for GERESS, All events for which a GERESS arrival significantly contributed to the location must be omitted. Therefore only onsets of such events ($\Delta \geq 20^\circ$) were used, which had $m_b \geq 5.0$ (NEIC) and which were located with more than 19 defining P phases. Additionally, all onsets with an absolute value of the travel time residual larger than 3.0 sec were rejected. Then the mean travel time residual of 1235 GERESS phases was estimated at $t_{res} = -0.76 \text{ sec}$ with a standard deviation of $\sigma_{tres} = 0.80 \text{ sec}$. Several effects can explain this bias:

The sensitivity of a station is the most important contribution to the travel time residual which is demonstrated with Fig. 3-12: the mean travel time residuals of other arrays and some European stations around GERESS are shown. Residuals are plotted with respect to the percentage of observed EDR events. The comparison is based on the contribution of seismic stations in the time period from April 1990 to February 18, 1993. The calculated percentage of observed events gives a rough idea of the sensitivity of the stations. All estimated parameters are listed in Table 3-1. It is obvious, that all high sensitive arrays have negative travel time residuals and that the single stations show a similar trend: the more sensitive the more negative is the station's travel time bias. This observation is confirmed by Grand (1990), who showed that the travel time residuals of different stations in the ISC bulletins correlate with the amplification of the stations. This result leads to the conclusion, that eventually the source time of larger events is systematically biased to later times due to the large number of less sensitive stations which observed these events.

Finally the magnitude bias of GERESS will be discussed. The same events as in the travel time residual study have been used to calculate the mean magnitude residual for GERESS. Due to the large number of PKP onsets, the number of m_b values is only 784. For these amplitudes, a mean $m_{b, res}$ of -0.61 with a stan-

dard deviation of $\sigma_{mb\ res} = 0.34$ was estimated. This relatively large magnitude bias cannot easily be explained. At the moment, we assume that the GERESS m_b residual is a summation of different effects: GERESS has its best SNR for P onsets in the frequency range between 1.0 Hz and 3.0 Hz (Jost, 1992). Therefore, this narrow frequency band is often used to analyse a teleseismic arrival. It is important to note that many of these onsets would not be visible on a WWSSN short period instrument (mean frequency ~ 1.0 Hz) at the GERESS site. This narrow band filtering increases the SNR but decreases the mean amplitudes. Additionally, some signal loss can occur due to the beam forming. Finally at the GERESS key station GEC2, we do not observe any amplification due to a sedimentary layer. All these points tend to decrease the amplitudes observed at the GERESS site. We assume as the most important effect that GERESS amplitudes are measured at relative short periods with respect to most other stations.

Using $\log A/T$ instead of $\log A$ in the definition of m_b , should compensate for different instrumentation and observing periods. But the m_b residuals of all stations used in the travel time study suggest that this compensation is not sufficient. Fig. 3-13 shows the m_b residuals of different stations plotted with respect to the mean reported period T to compute $\log A/T$ (all parameters are given in Table 3-1). The stations with periods less than 1.0 sec show a negative m_b residual. Signal loss due to beam forming and reading parameters from a beam trace can have some additional effect so that most arrays have a negative m_b residual. All these data are influenced by the local geology, but if only stations are compared which are in the same geological unit, the main influence seems to be the period at which amplitudes are measured (e. g. GEC2, KHC, WET, BRG, PRU, MOX, VRAC).

3.5 Conclusion

In this report teleseismic phases detected at the GERESS array were evaluated with respect to the EDR bulletins. No seasonal effect of the detection capability for GERESS was found. As expected the detection capability of GERESS changes with epicentral distance; for events in the Earth's core shadow between 100° and 120° epicentral distance GERESS observed only 10 % to 20 % of all corresponding EDR events. In contrast, for PKP arrivals GERESS observed ~ 85 % of all EDR events due to the PKP caustic effect. The daily variation (~ 8 %) of the detection capability for GERESS could be associated with an increase of cultural and industrial noise during working hours.

Although GERESS with its small aperture has only a limited resolution in measuring slowness and backazimuth of teleseismic onsets, systematic mislocation vectors were found for GERESS.

Finally, travel time and amplitude residuals of GERESS were discussed. The negative travel time residual of GERESS can mostly be explained by the high sensitivity of the array. The negative m_b residual of GERESS seems to be a summation of different effects which all tend to diminish amplitudes with respect to

other stations. For both - travel times and amplitudes - the GERESS residuals are comparable with residuals from other high sensitive arrays.

Literature

Grand, St. P. (1990): A possible station bias in travel time measurements reported to ISC. *Geoph. Res. Let.* 17, 17 - 20.

Jost, M. (1992): GERESS P-wave detectability. In: Advanced waveform research methods for GERESS recordings. DARPA Annual Report No. AFOSR-90-0189, Scientific Report No. 2, PL-TR-92-2142, 13-24. ADA253686

Kennett, B. L. N. and E. R. Engdahl (1991): Travel times for global earthquake location and phase identification. *Geoph. J. Int.* 105, 429 - 466.

Schweitzer, J. (1992): The GERESS contribution to the GSETT-2 experiment 1991. In: Advanced waveform research methods for GERESS recordings. DARPA Annual Report No. AFOSR-90-0189, Scientific Report No. 2, PL-TR-92-2142, 25 - 49. ADA253686

Schweitzer, J., Jost M. L. and N. Gester mann (1992): GERESS - A new array for on-line monitoring the regional seismicity in Central Europe. *Cahiers du Centre Européen de Géodynamique et de Séismologie* 5, 1 - 10.

Table 3-1: Estimated travel time residuals (t_{res}) and magnitude residuals (m_b res) for different arrays and European stations with the number of observations (# of events, # of m_b , T). Also listed are the percentage of observed events with respect to the total number of events in the investigated time period (% of events) and the mean period of reported amplitude measurements to calculate m_b (mean T). Additionally given are the standard deviations (σ_t ; σ_{mb} ; σ_T) respectively.

Station	t_{res}	σ_t	% of events	# of events	m_b res	σ_{mb}	mean T	σ_T [sec]	# of m_b , T
AQU	0.73	0.73	10.1	407	-	-	-	-	-
BNS	0.28	0.37	11.4	924	0.14	0.26	1.40	0.26	115
BRG	1.01	0.22	47.5	1933	-0.03	0.22	1.36	0.37	1185
CLL	-0.11	0.23	51.7	2104	0.04	0.24	1.45	0.38	1215
EKA	-0.01	0.22	31.9	1300	-0.14	0.27	1.06	0.39	1034
ENN	0.27	0.33	28.0	1139	0.04	0.27	1.01	0.24	846
FIR	0.54	0.61	9.6	336	-	-	-	-	-
FUR	0.40	0.43	16.6	671	0.26	0.28	1.19	0.35	245
GBA	-0.30	0.44	33.9	1360	-0.24	0.36	0.87	0.26	798
GEC2	-0.76	0.80	70.7	1235	-0.61	0.34	0.85	0.23	784
GRF	0.45	0.47	42.3	1718	0.15	0.25	1.35	0.45	924
HFS	-1.06	1.06	45.0	1838	-0.10	0.41	0.74	0.33	1537
KAF	-0.84	0.85	45.1	1385	-0.09	0.32	0.69	0.22	934
KBA	0.08	0.24	24.3	987	0.08	0.28	1.11	0.36	708
KHC	0.24	0.30	51.1	2077	-0.29	0.24	1.19	0.20	910
KRA	0.08	0.22	32.7	1135	0.26	0.28	1.00	0.30	518
KSP	-0.04	0.16	46.2	1877	0.07	0.26	1.12	0.26	525
LJU	0.02	0.19	23.9	832	-	-	-	-	-
LOR	-0.32	0.37	44.0	1791	-0.06	0.24	1.02	0.26	1247
MLR	0.46	0.50	31.0	1251	-	-	-	-	-
MOX	0.25	0.32	41.7	1692	-0.01	0.23	1.61	0.36	964
NB2	-0.89	0.88	48.3	1690	-0.15	0.31	0.93	0.23	1272
OSS	0.22	0.32	19.6	794	-	-	-	-	-
PRU	0.19	0.27	44.8	1820	-0.14	0.24	1.40	0.44	678
PSZ	0.30	0.37	15.7	633	-	-	-	-	-
SOTA	-0.24	0.38	19.2	723	0.09	0.24	1.11	0.36	516
TNS	0.20	0.26	9.8	343	-	-	-	-	-
VKA	0.11	0.23	16.5	668	-	-	-	-	-
VRAC	-	-	-	-	0.38	0.32	1.89	0.89	76
WET	0.34	0.35	20.2	819	0.10	0.23	1.24	0.30	392
WRA	-0.72	0.74	46.4	1705	-0.28	0.45	0.76	0.27	1302
YKA	-0.79	0.80	61.9	2516	-0.44	0.38	0.86	0.20	2233

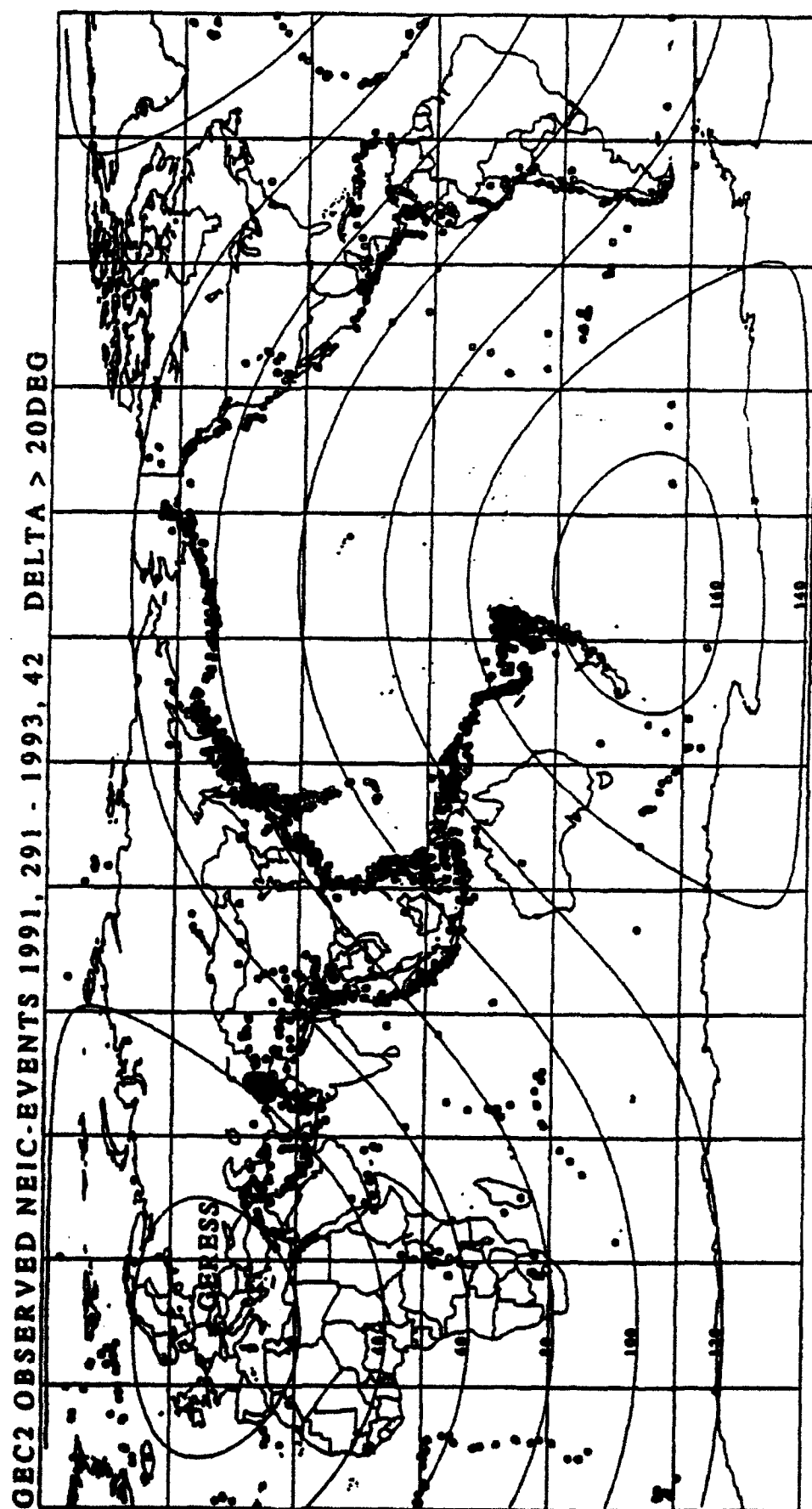


Figure 3-1: All events ($\Delta > 20^\circ$) for which NEIC associated a GERESS onset (October 18, 1991 - February 11, 1993).

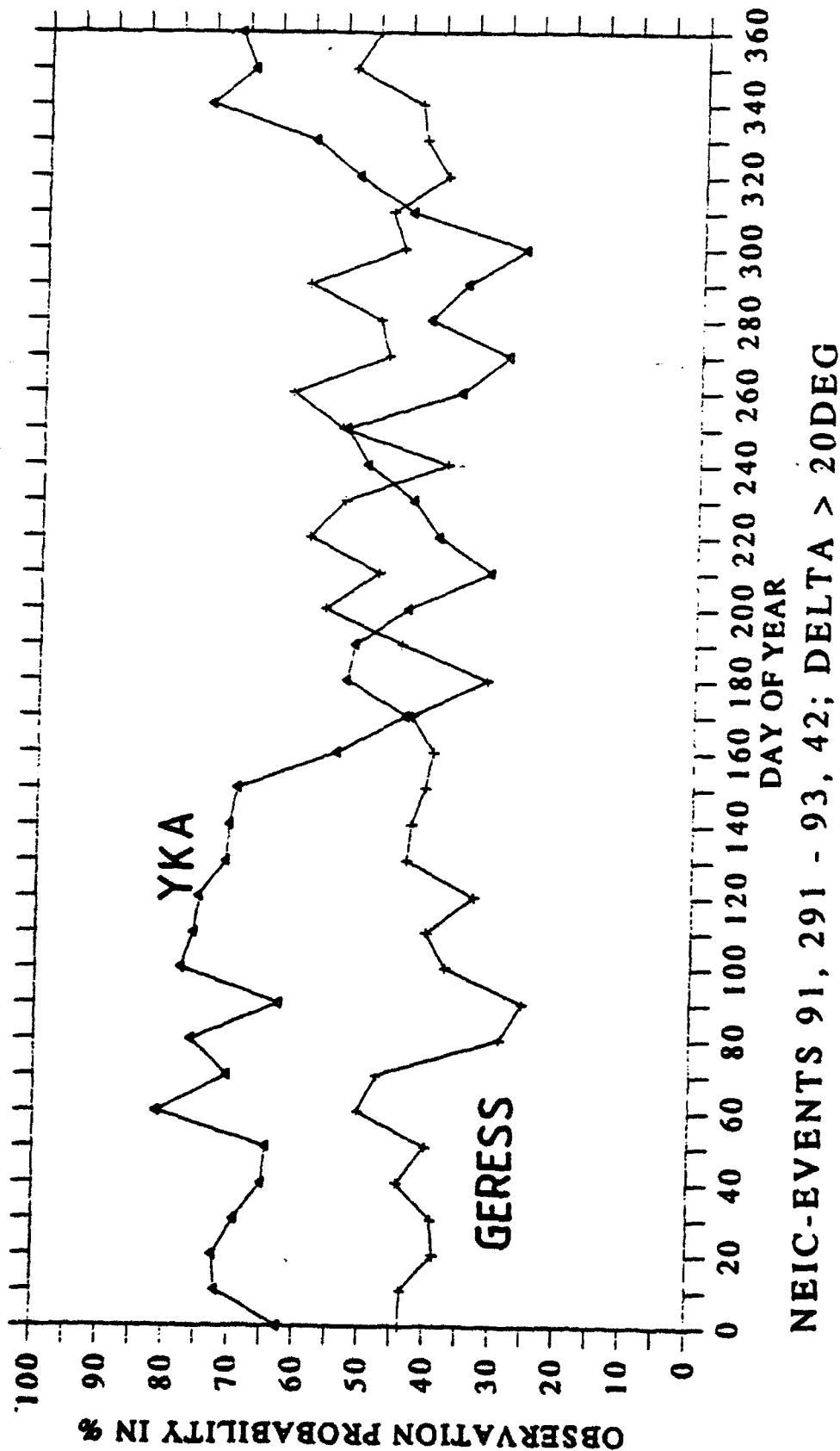


Figure 3-2: The probability to observe an EDR event ($\Delta > 20^\circ$) at GERESS (crosses) and at YKA (triangles) with respect to the day of the year in the investigated time period (October 18, 1991 - February 11, 1993).

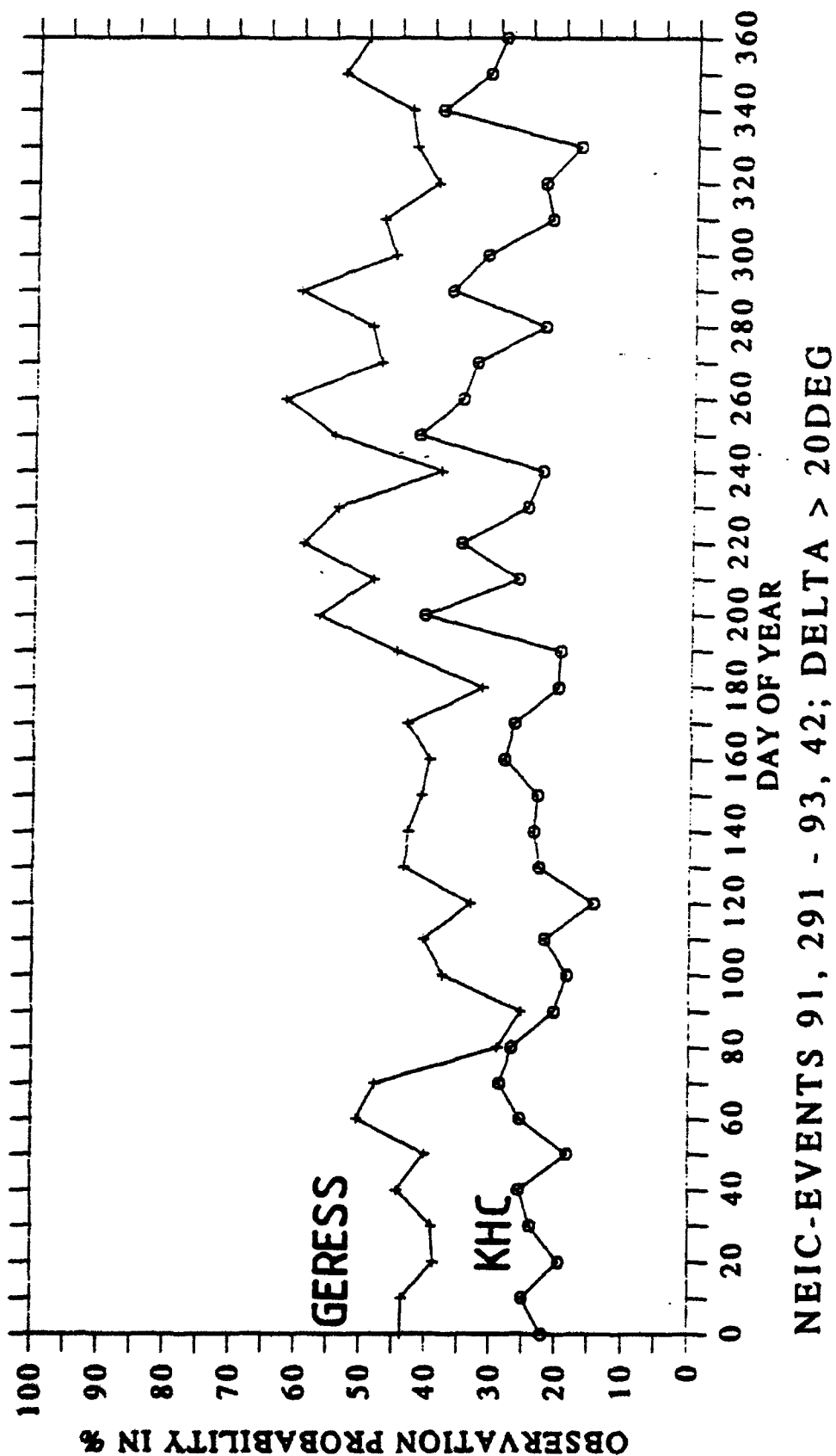
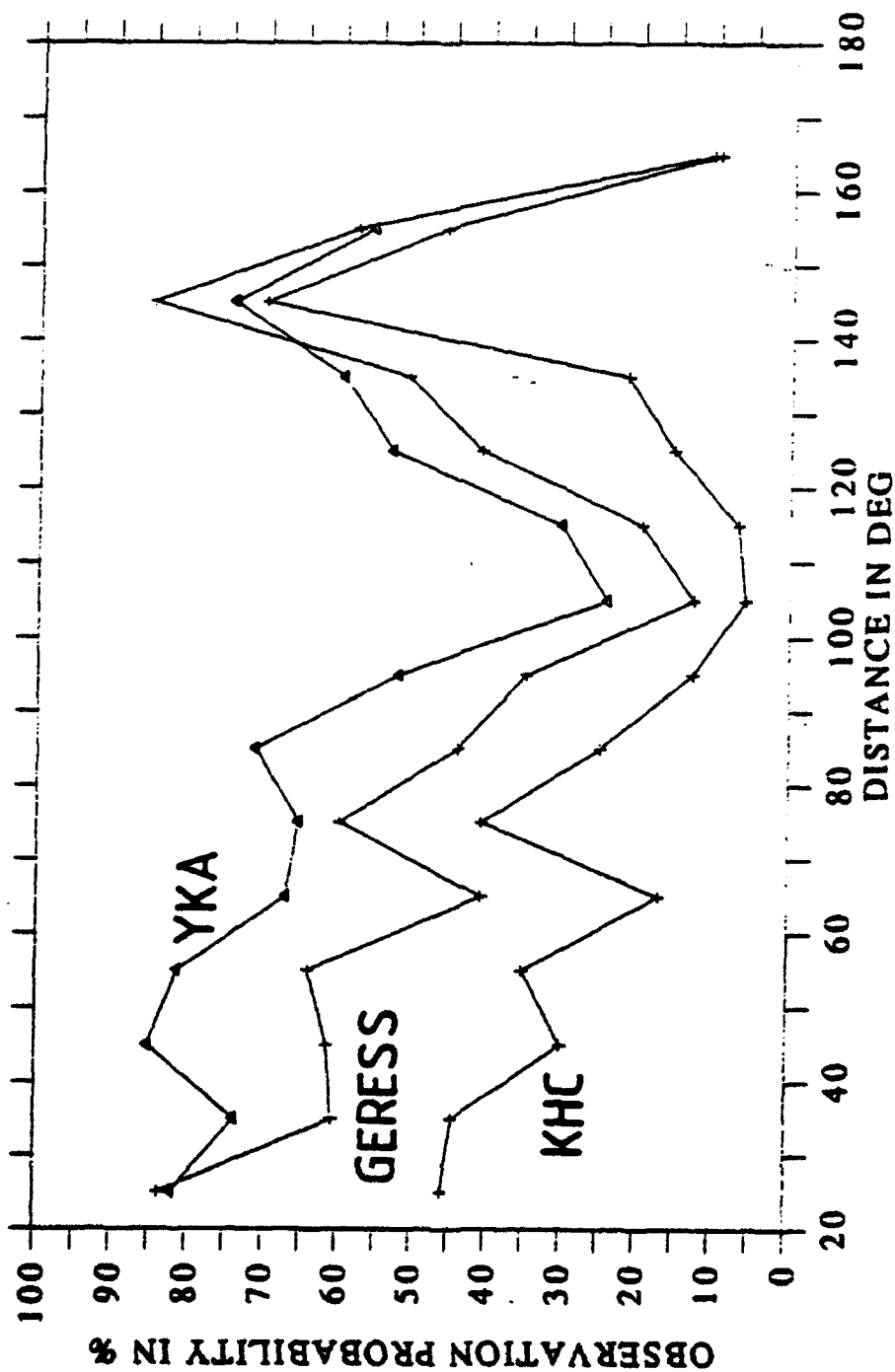


Figure 3-3: As Fig. 3-2, but for GERESS (crosses) and KHC (circles).



NEIC-EVENTS 91, 291 - 93, 42; DELTA > 20 DEG

Figure 3-4: The probability to observe an EDR event at GERESS (crosses), at YKA (triangles), and at KHC (circles) with respect to the epicentral distance in the investigated time period (October 18, 1991 - February 11, 1993).

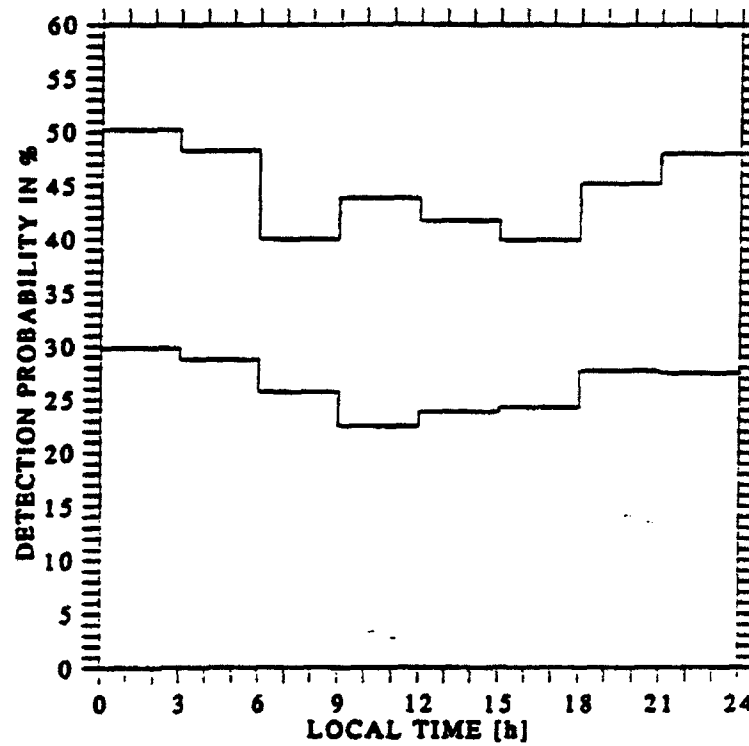


Figure 3-5: The probability to observe an event ($\Delta > 20^\circ$) during the time of day in the investigated time period (October 18, 1991 - February 11, 1993) for GERESS (upper line) and KHC (lower line).

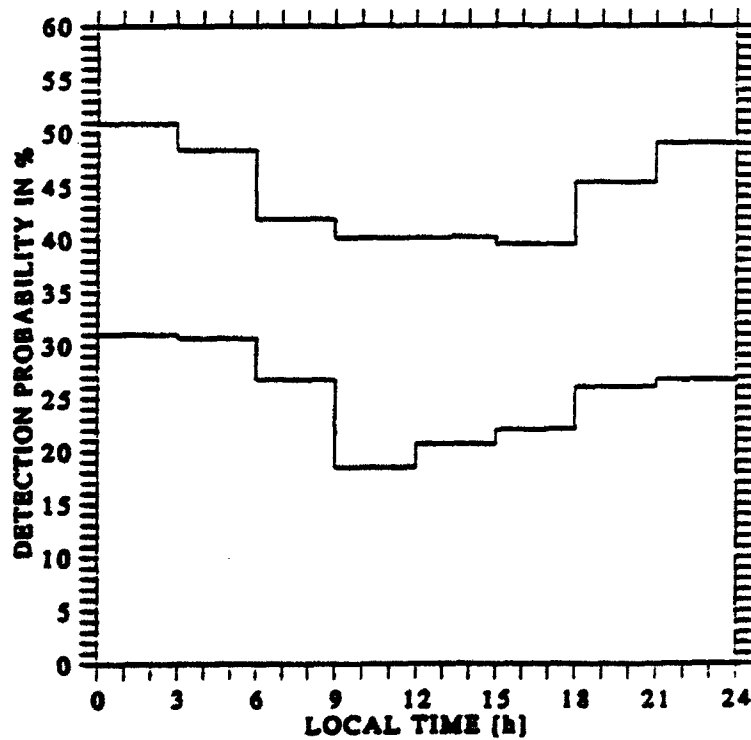


Figure 3-6: As Fig. 3-5, but only for working days in Germany.

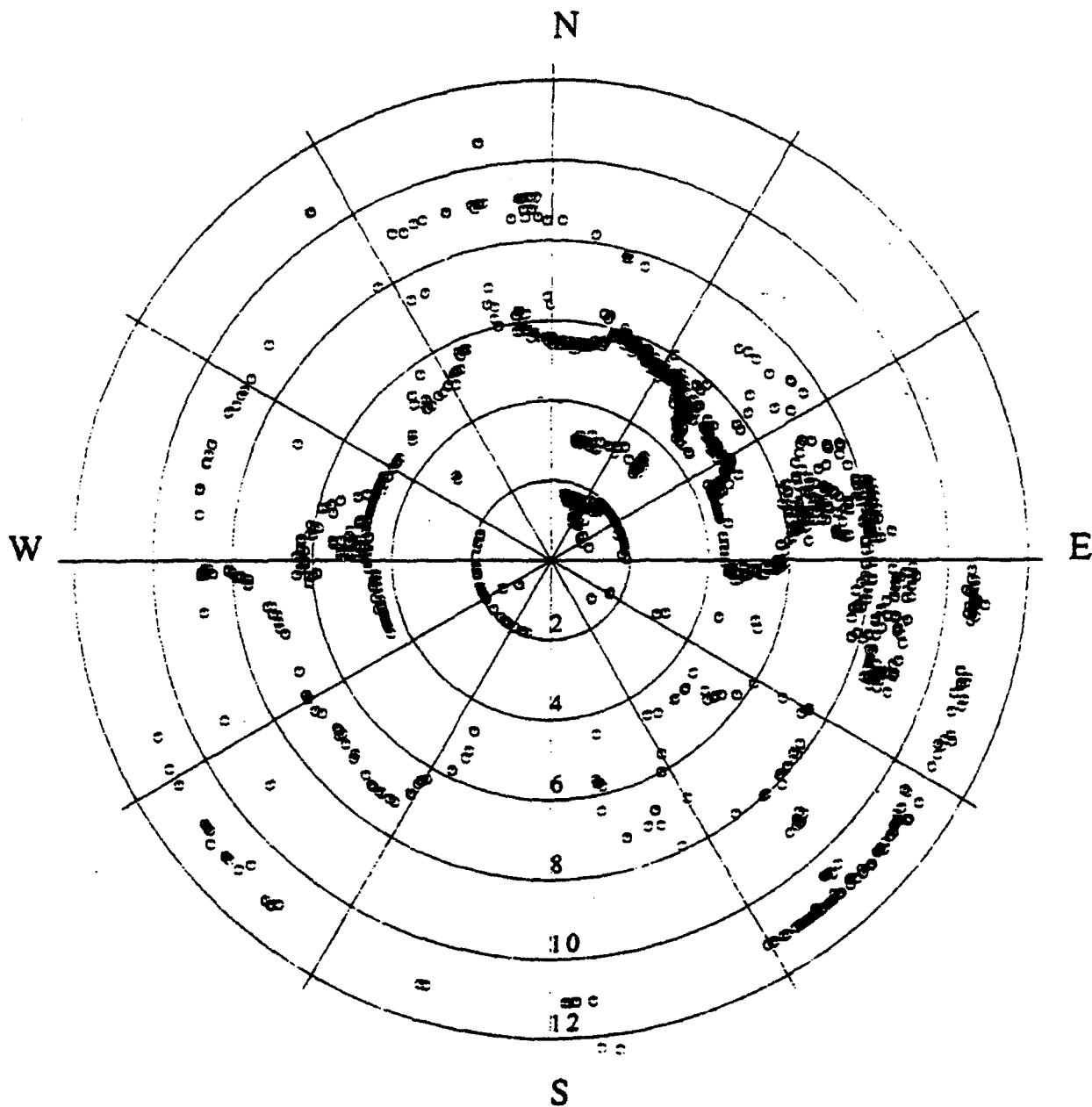


Figure 3-7: Theoretical slowness and backazimuth values of all onsets (April 22, 1991 - June 2, 1991; October 18, 1991 - February 18, 1993) used to estimate the GERESS mislocation vectors. The data are plotted in the slowness space; the distance between two circles is 2 sec/°.

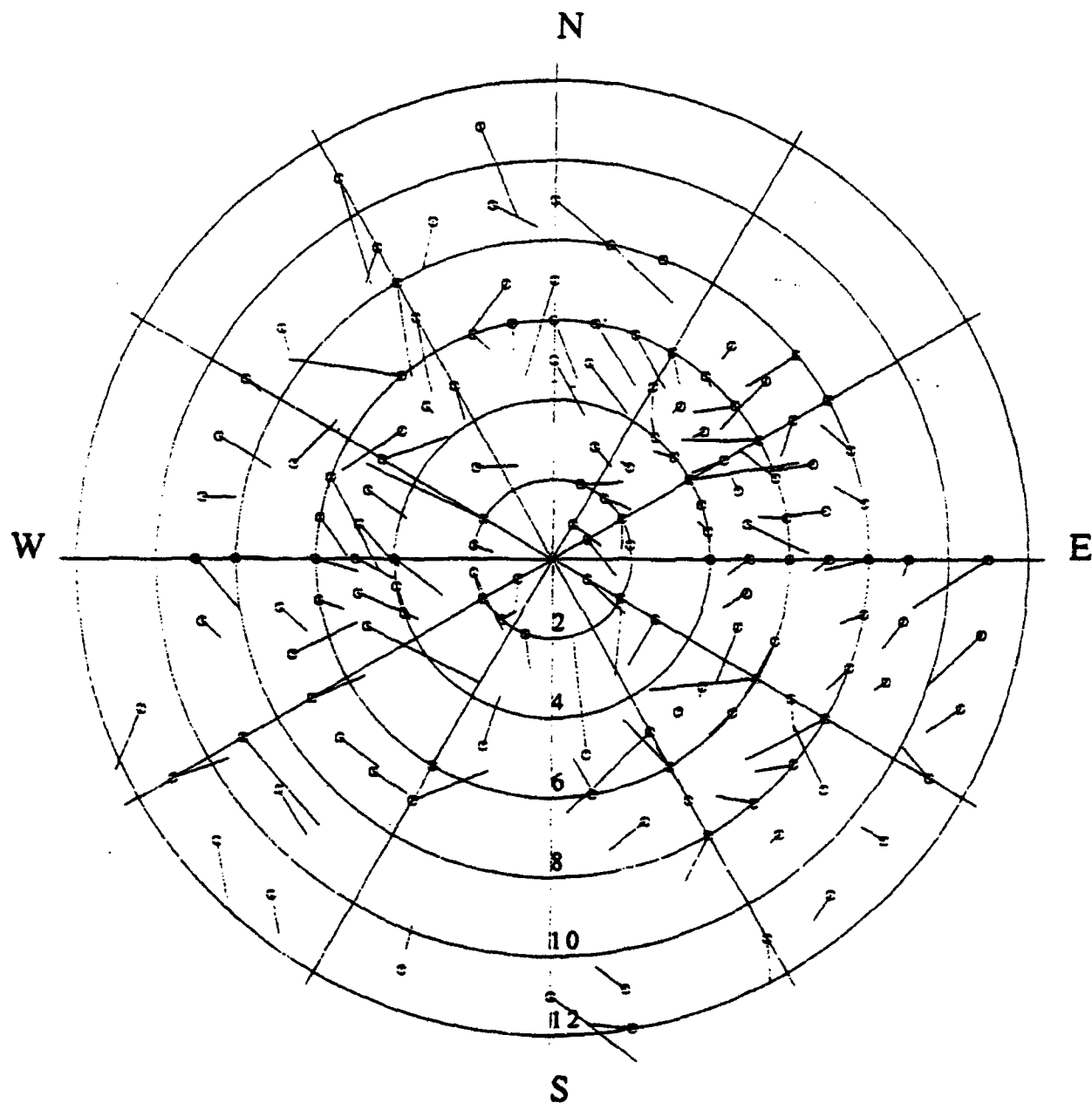


Figure 3-8: GERESS mean mislocation vectors. The symbols are plotted at the theoretical value. For further details see the text.

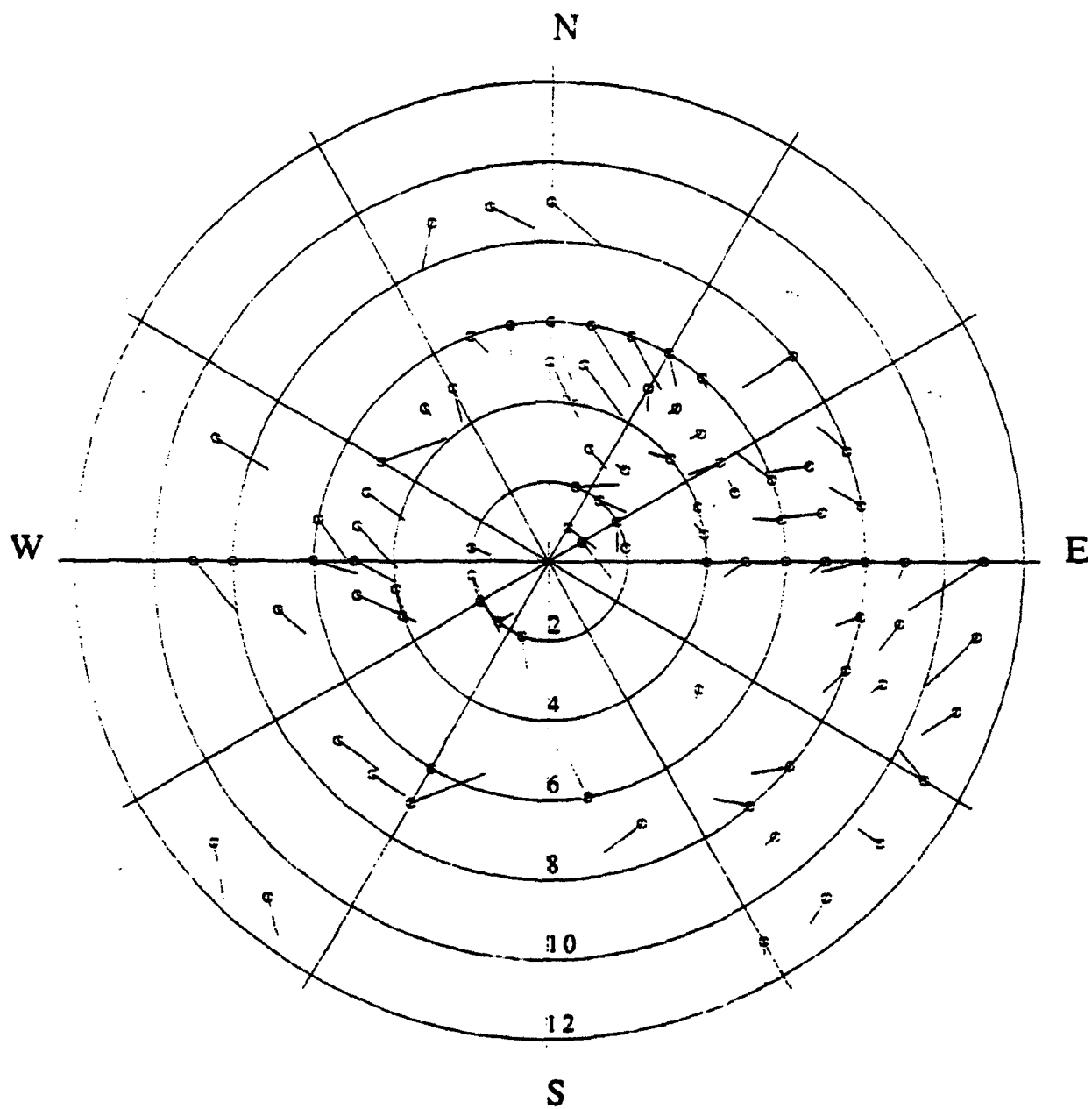


Figure 3-9: As Fig. 3-8, but only those mislocation vectors, which were calculated with at least 5 observations.

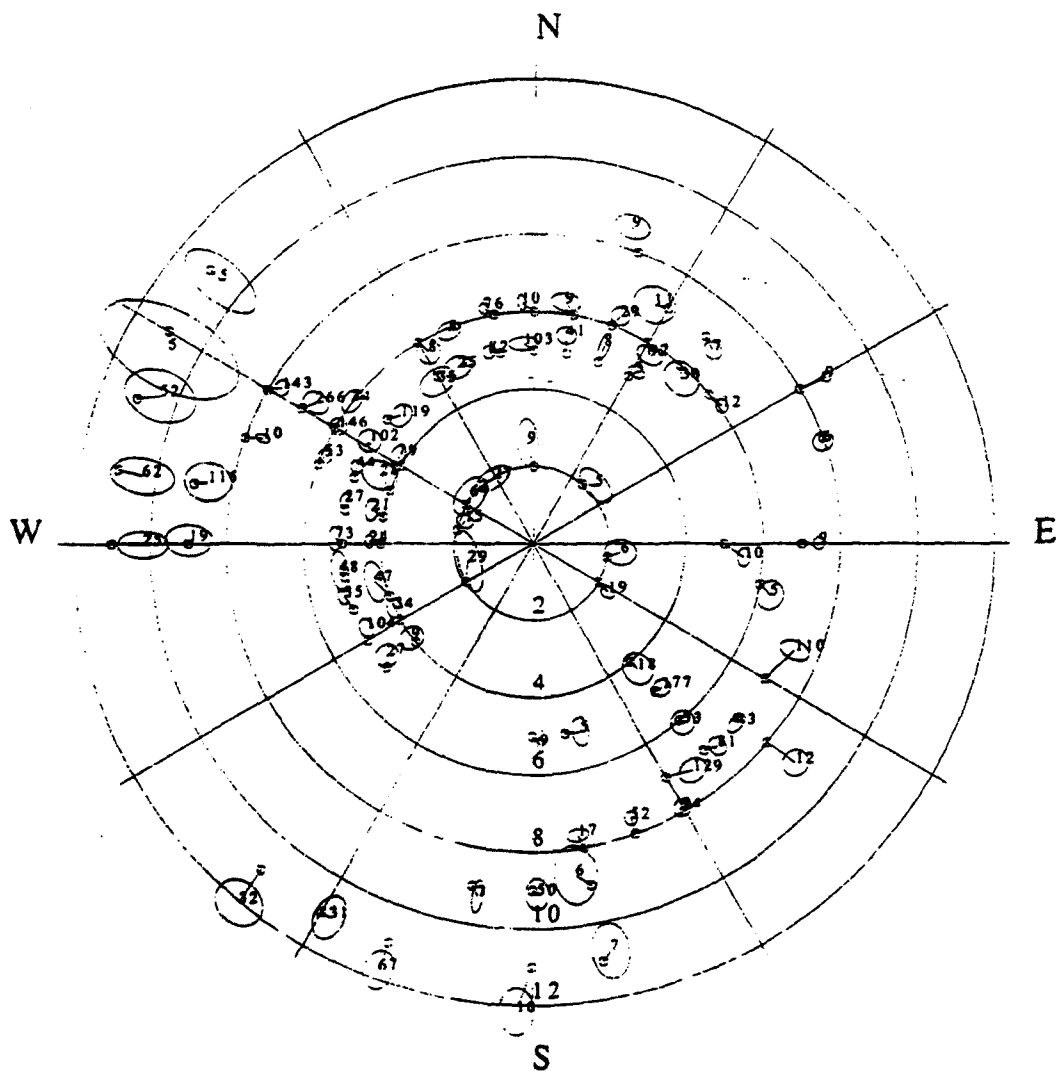


Figure 3-10: As Fig. 3-9, but for YKA. Given is the numbers of observations for the vector and the standard deviations are shown as ellipse.

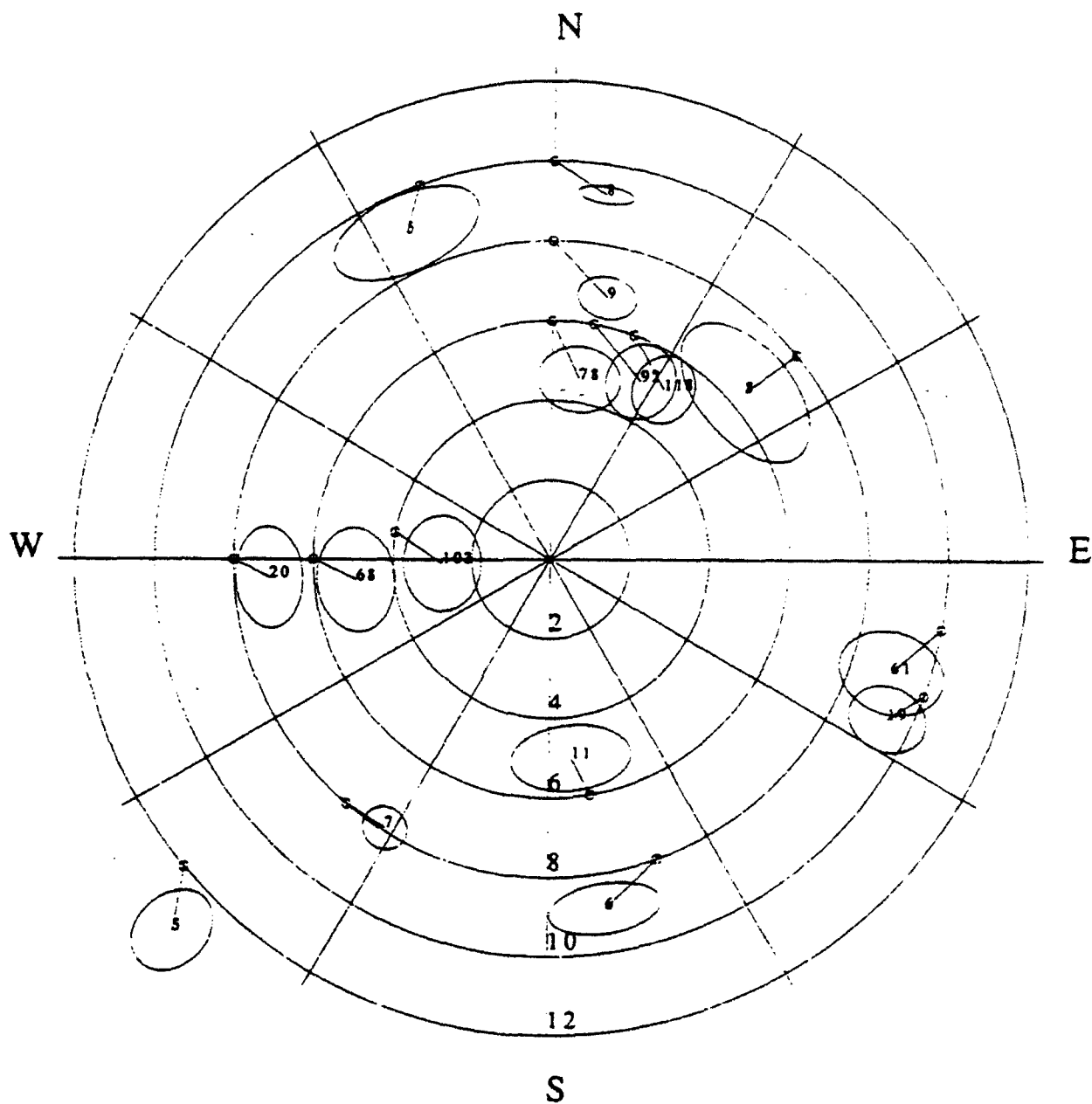


Figure 3-11: As Fig. 3-9, but only those mislocation vectors, for which the mislocation is larger than their standard deviation respectively. Additionally given is the number of observations and the standard deviation as ellipse.

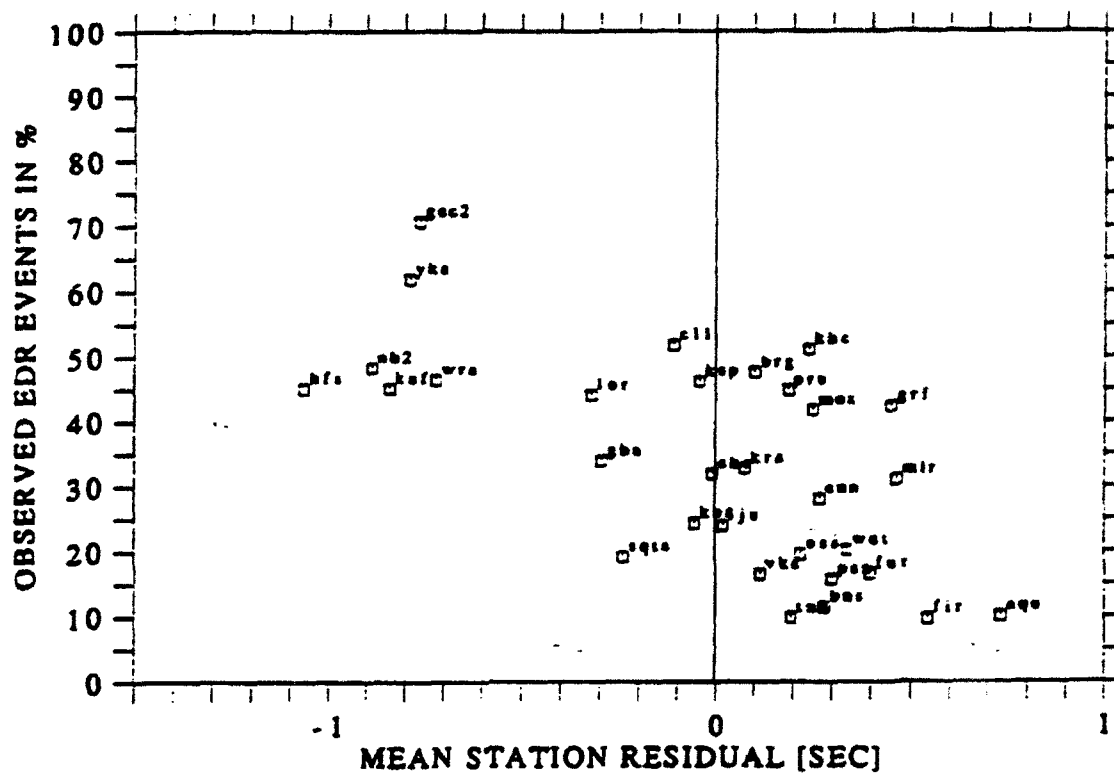


Figure 3-12: Percentage of NEIC events observed at different seismic stations versus the station travel time residuals respectively. For more details see text.

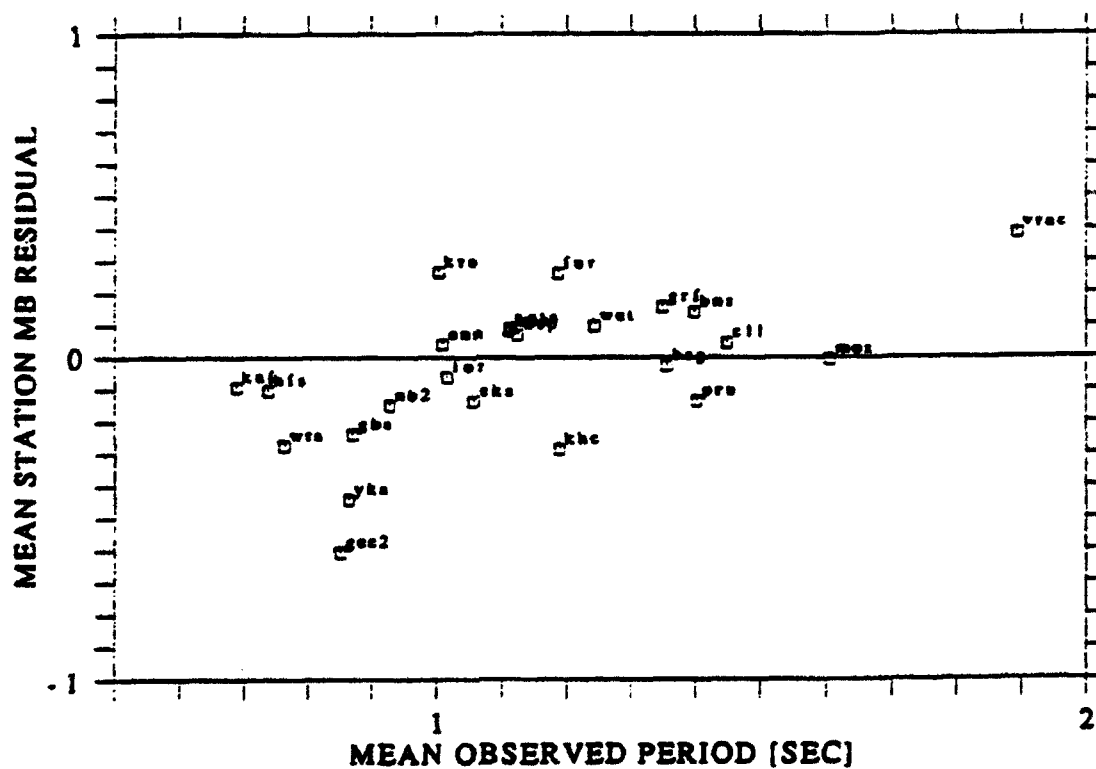


Figure 3-13: Mean m_b residuals of different stations plotted with respect to the mean measured periods.

4. STEEP ANGLE REFLECTIONS FROM THE EARTH'S CORE OBSERVED WITH THE GERESS ARRAY

Johannes Schweitzer

4.1 Introduction

The systematic search for unusual phases has found more interest in the last years. These observations can be used either to study the spherical structure of the Earth or serve as an additional information in tomographic studies. Detailed investigations of reported phases to the ISC and NEIC (Doombos et al., 1991; Hwang and Clayton, 1991) show, that many later arrivals in seismograms can be identified and analysed.

The scientific goal of the International Seismological Observing Period (ISOP) is to collect not only observations of high quality of the standard seismic phases but also to complete those parts of travel time curves, which are not yet confirmed with sufficient observations. Because these phases are often small and disturbed by other more dominant onsets, phase identification and interpretation has to be done very carefully. One way to distinguish between different onsets is the usage of array techniques.

Fig. 4-1 shows the theoretical travel time curves for a surface focus (IASP91 model, Kennett and Engdahl, 1991) and in Fig. 4-2 travel times reported to the ISC and accumulated for 10 years are shown (Doombos et al., 1991). The core reflections PcP and ScP are usually not observed or not reported at epicentral distances smaller than 20° and for PKiKP at epicentral distances smaller than 100° . In this study the most sensitive seismic station in Central Europe, the GERESS array, is used to search for such steep angle reflections from the Earth's core.

4.2 PcP observations in less than 35° epicentral distance

In a search for steep angle PcP phases, the GERESS data base from April 1990 to February 1991 was analysed. The selecting criteria were a m_b value of larger than 5.0 (NEIC) and an epicentral distance less than 35° . For this chosen time period, 25 events were found in the GERESS data base. The source parameters are summarised in Table 4-1 and the locations of the events are shown in Fig. 4-3. Only in three cases (filled triangles), a clear PcP onset was found. In one case a small onset could be observed but this onset could not be identified

Table 4-1: Events used in this PcP study. All parameters for events in 1990 are from the ISC bulletins, for the 1991 event from NEIC.

DATE	TIME	LAT [°]	LON [°]	DEPT H [km]	m_b	Δ [°]	PcP
1990 Apr 20	23:30:05.1	40.12 N	40.07 E	22	5.0	20.7	---
1990 May 05	07:21:29.6	40.74 N	15.74 E	9	5.1	8.2	---
1990 May 30	10:40:06.4	45.85 N	26.66 E	89	6.4	9.3	---
1990 May 31	11:17:48.2	45.81 N	26.77 E	90	5.9	9.4	---
1990 Jun 09	17:24:52.6	40.16 N	29.71 W	10	4.9	31.5	---
1990 Jun 16	02:16:21.1	39.27 N	20.55 E	32	5.5	10.8	---
1990 Jun 21	09:02:14.8	36.65 N	49.83 E	11	5.1	28.9	yes
1990 Jun 21	12:17:32.2	36.94 N	49.48 E	41	5.8	28.5	---
1990 Jul 06	19:34:54.3	36.91 N	49.30 E	45	5.2	28.4	---
1990 Jul 09	11:22:18.1	34.94 N	26.63 E	41	5.0	16.9	---
1990 Jul 24	17:59:50.7	32.84 N	48.22 E	24	5.3	30.3	?
1990 Sep 09	06:24:57.8	56.59 N	34.39 W	19	5.1	29.6	---
1990 Sep 09	06:35:22.7	56.48 N	34.44 W	10	4.9	29.6	---
1990 Sep 10	12:17:37.0	70.75 N	13.80 W	10	5.0	25.5	---
1990 Sep 15	23:07:43.2	64.75 N	17.50 W	18	5.3	23.0	---
1990 Oct 08	23:42:42.5	44.11 N	19.32 E	10	---	6.1	---
1990 Oct 24	14:57:58.2	73.36 N	54.67 E	0	5.7	30.4	yes
1990 Nov 12	16:00:49.6	40.31 N	51.63 E	44	5.2	28.1	---
1990 Nov 27	04:37:57.0	43.87 N	16.67 E	19	5.2	5.4	---
1990 Nov 27	04:51:36.5	43.90 N	16.65 E	10	5.0	5.4	---
1990 Dec 13	00:24:25.7	37.31 N	15.43 E	11	5.3	11.6	---
1990 Dec 14	03:21:26.9	39.35 N	15.39 E	275	4.9	9.6	yes
1990 Dec 16	15:45:40.3	41.37 N	43.72 E	28	5.3	22.4	---
1990 Dec 29	15:34:17.2	32.59 N	47.86 E	34	5.1	30.2	---
1991 Feb 26	07:25:47.2	40.17 N	13.82 E	401	5.5	8.7	---

obviously as PcP. For all other events no PcP onsets were found. This illustrates again the difficulties to observe PcP under steep angle conditions.

The most prominent PcP observation was from the nuclear test at Novaya Zemlya on October 24, 1990. The seismograms (Fig. 4-4) are dominated by approximately three minutes of large amplitudes after the first onset and an additional sharp onset after about 200 seconds. The observed P coda is mostly due to the mantle triplication's, P energy reflected multiply at the Earth's surface (e. g. PP, pPP, sPP, PPP, ...), and energy scattered at lateral heterogeneities in upper mantle and crust. The sharp onset is the PcP phase, which can be identified even on single unfiltered traces of the GERESS array. Fig. 4-5 exhibits PcP in more detail with the GERESS PcP beam trace on the top. PcP has the classical simple pulse form as expected from an explosion source contrary to the complex seismogram of the P onset (Fig. 4-6). Because of the simple PcP pulse form the complex P pulse form can only be explained with heterogeneities along the P ray path from Novaya Zemlya to GERESS.

Fig. 4-7 shows the seismograms of an event in Western Iran (June 21, 1990) with similar strength and epicentral distance as the last nuclear test of the Soviet Union. The seismograms again show a clear PcP onset on all GERESS single traces but the P coda is much smaller. However, additionally clear depth phase energy (pP, sP) can be seen (source depth 41 km). The energy increase after PcP can be explained as pPcP and sPcP energy. Fig. 4-8 shows the Butterworth band pass (0.5 Hz - 4.0 Hz) filtered GERESS beams for P and PcP.

Some days later (July 6, 1990) another event occurred in the same source region. The seismograms (Fig. 4-9) show - as in the case of the nuclear test - a larger P phase coda and significant energy for the surface reflections. Once again, an onset at the presumed PcP arrival time can be observed at the GERESS array. But the fk-analysis of this onset yields a phase velocity which is too low to be explained as a phase reflected from the Earth's core. This example demonstrates again the advantage to use an array to identify arrivals. The observed difference between the PcP observations from two events in the same source region can only be explained by different focal mechanisms of the two events. Fig. 4-10.a shows the Harvard CMT solution (from the ISC bulletin) of the first event and Fig. 4-10.b shows the Harvard CMT solution of the second event, respectively. The second event has a very small PcP radiation and the large P phase radiation (T-axes) in direction to GERESS. Both facts reduced the possibility to observe PcP.

It is not surprising, that PcP is difficult to observe in the cross over distance with the S phase in the vicinity of 20° epicentral distance. The PcP reflection coefficient (Fig. 4-11) at the core mantle boundary (CMB) decreases with decreasing epicentral distance and the S energy of larger events normally dominates the seismogram on all 3 components at these distances. Another possibility to observe PcP exists at distances up to about 10° epicentral distance. In this case, the array technique can be used to suppress the S coda and surface waves by velocity filtering. The excitation of surface waves is normally small for intermediate or deep

events. In this study four of such events at regional distances were investigated and the data of two events are discussed in the following.

The first event was the large Romanian earthquake occurring on May 31, 1990 ($\Delta = 9.4^\circ$, $h_0 = 90$). The focal mechanism of this event (Fig. 4-12.a) shows a good PcP radiation but also good P and S phase radiation in the direction of the GERESS array. Consequently the observed seismograms show more or less constant amplitudes over several minutes (Fig. 4-13). Therefore it is very difficult to identify the PcP onset.

The last example in this PcP study is the event of December 14, 1990 ($\Delta = 9.6^\circ$, $h_0 = 275$ km). The focal mechanism (Fig. 4-12.b) compiled from the first motion data in the ISC bulletin shows clearly, that the P and S radiation in the direction to GERESS (*azimuth* = 353°) was relatively small. This is confirmed by the GERESS seismograms (Fig. 4-14). After the P coda, no significant S phase is seen and L_g waves or other surface waves are missing. In the theoretical time window of PcP a small arrival can be seen in the unfiltered seismograms (Fig. 4-15), which was also detected by the automatic GERESS data analysis. With a fk-analysis a ray parameter $p = 1.9$ sec/ $^\circ$ and a backazimuth (BAZ) of 118.8° could be estimated. Within the limited resolution of the GERESS array for higher velocities, these values are in agreement with the theoretical values ($p = 0.9$ sec/ $^\circ$, BAZ = 172.3°). Approximately 5 sec later a PP onset of an event in Taiwan ($m_b = 5.2$) can be expected at the GERESS array (theoretical values of $p = 8.2$ sec/ $^\circ$ and BAZ = 61.3°). With the result of the fk-analysis this hypothesis for the observed onset can be rejected and the onset can be clearly identified as a PcP observation in $\Delta = 9.6^\circ$.

4.3 ScP Observations in less than 20° epicentral distance

If the SV radiation of events in direction of the core is large enough, the SV to P converted reflection from the CMB (ScP) can be observed. The arrival time of ScP is approximately 200 sec after PcP and therefore less disturbed by S phases or surface waves. Additionally the reflection coefficient for ScP at the CMB is larger as in the case of PcP (Fig. 4-16), in the observed epicentral distance range from 12° to 18° the reflection coefficient of ScP is comparable with the PcP reflection coefficient between 23° and 35° epicentral distance. Without any systematic search for ScP in the GERESS data base some ScP observations can be shown in this report. The GERESS detector found onsets at the theoretical arrival time of ScP for three recent events in epicentral distances less than 20° (see Table 4.2). The results of the fk-analysis show, that these arrivals have the right BAZ and slowness as expected for ScP. Fig. 4-17 shows the Butterworth band pass filtered traces (0.7 Hz - 3.0 Hz) of these observations, once for the GERESS beam and once for the data of the GERESS reference site GEC2.

Table 4.2: The events used for the ScP study. The parameters are from NEIC weekly listings.

DATE	TIME	LAT [°]	LON [°]	DEPTH [km]	m_b	D [°]
1992 Nov 18	21:10:40.9	38.30 N	22.43 E	10	5.9	12.3
1992 Nov 21	05:07:22.8	35.93 N	22.44 E	70	5.9	14.4
1993 Jan 09	24:52:44.5	35.88 N	29.94 E	32	4.6	17.6

4.4 A PKiKP observation with the GERESS array in 51.4°

PKiKP is rarely observed at epicentral distances less than 90°. Due to the small reflection coefficient (Fig. 4-18) of PKiKP at the inner core boundary (ICB) of less than 5 %, only small amplitudes can be expected for such steep angle reflections, especially since the wave also has to penetrate additionally twice the CMB. The large Chinese nuclear test ($m_b = 6.5$) on May 21, 1992 at 05:00 UT allowed the analysis of this phase. Fig. 4-19 shows that the S phase radiation of this explosion was very small (as expected) and that the P radiation to the Earth's core was relatively good - as the clear PcP onset shows. The search for PKiKP onsets for this event at the Scandinavian arrays (ARCESS, FINESA, NORESS), at the Gräfenberg array (GRF), and at seven broad band stations in Central Europe (BFO, BUG, CLZ, FUR, KSP, TNS, WET) was not successful, only at the GERESS array a PKiKP onset could be identified.

The GERESS short period vertical traces were filtered with a Butterworth band pass filter (1.0 Hz - 3.0 Hz) since the GERESS array has the best signal to noise ratio (SNR) for P onsets (Jost, 1992) in this frequency band. On the single traces of the GERESS array, no clear onset is visible. But the fk-analysis (Fig. 4-20) of the PKiKP expected time window shows that at this time, energy arrived with the high phase velocity of 105.9 km/sec (1.05 sec/°) from the East (BAZ = 80.9°). The difference to the theoretical values (103.0 km/sec or $p = 1.09$ sec/° for the IASP91 travel time tables, BAZ = 68.0°) is surprisingly small with respect to the accuracy of slowness measurements of the GERESS array (see Chapter 5 in this report). Additional investigations with vespagrams and a moving window-fk analysis (Gestermann, 1992) to estimate slowness and azimuth of this onset confirmed the former result: very high velocities and a BAZ from the East. Fig. 4-21 shows the GERESS beam calculated with the results of the fk-analysis (Fig. 4-20) for the PKiKP onset in the middle. At the top, the SNR-trace (calculated as relation between the short time (1 sec) to the long time (30 sec) amplitude average) of the beam is seen, and at the bottom the GERESS reference station GEC2. Additionally, the theoretical PKiKP onset time of the IASP91 travel time tables is marked.

A PKiKP observation in this distance is not only interesting because of the travel time information for P phases travelling through the Earth's core, but the existence of steep angle observations of PKiKP also confirms that the ICB is a

sharp boundary. The amplitudes of PKiKP can be used to investigate the reflection coefficient at the ICB. Shearer and Masters (1990) systematically searched for PKiKP onsets through the GDSN data base. They found only two observations of this rare phase in a time period of 5 years. To discuss amplitudes of PKiKP with respect to the reflection coefficient they compiled PKiKP observations from the literature. To normalise the PKiKP amplitudes, it is best to give the PKiKP/PcP amplitude ratio. Therefore, the GERESS PcP beam of the Chinese nuclear test was processed similarly as the PKiKP beam (Fig. 4-22). The observed PKiKP amplitude at GERESS in $\Delta = 51.4^\circ$ is 3.2 % of the PcP amplitude. This datum has been added to the data of Shearer and Masters (Fig. 4-23). The new observation is in good agreement with their data.

4.5 Conclusion

The search for steep angle reflections from the Earth's core has demonstrated that small aperture short period arrays like GERESS can not only be used to investigate local and regional seismicity. Due to sites with high SNR conditions, due to beam forming techniques with a large number of seismic traces including some redundant informations, and due to fk-analysis for estimating the phase velocity and the BAZ, such arrays have great capabilities for other seismological purposes. The capabilities of the GERESS array can be also used to associate later arrivals (e. g. PP', PKKP, ...) to the appropriate events by using the BAZ information or to detect small events at teleseismic distances. Especially in connection with the ISOP project, the advantages of small aperture arrays like GERESS can be used to search for rare seismic phases, which normally cannot be detected or cannot be identified with single seismic stations.

Literature

- Doombos, D. J., E. R. Engdahl, T. H. Jordan, and E. A. Bergman (1991): International seismological observing period, preliminary science plan. USGS.
- Dziewonski, A. M. and D. L. Anderson (1981): Preliminary reference Earth model. *Phys. Earth Planet. Inter.* **25**, 297-356.
- Gestermann, N. (1992): Characteristics of regional phases recorded at GERESS. In: Advanced waveform research methods for GERESS recordings. DARPA Annual Report No. AFOSR-90-0189, Scientific Report No. 2, PL-TR-92-2142, 60 - 91. ADA253686
- Herrin, E. et al. (1968): 1968 seismological tables for P phases. *Bull. Seism. Soc. Am.* **58**, 1193 - 1241.
- Hwang, L. J. and R. W. Clayton (1991): A station catalog of ISC arrivals: seismic station histories and residuals. USGS Open File Report 91-295.

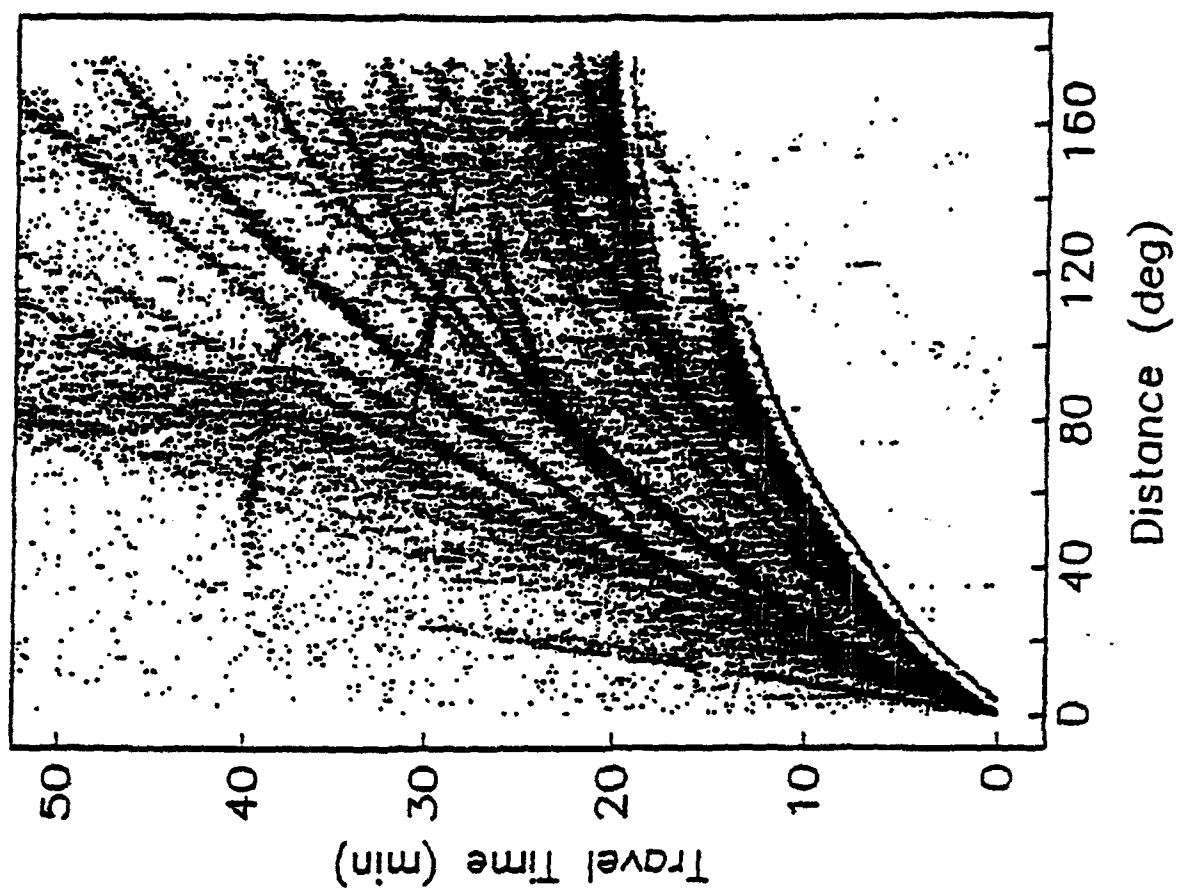
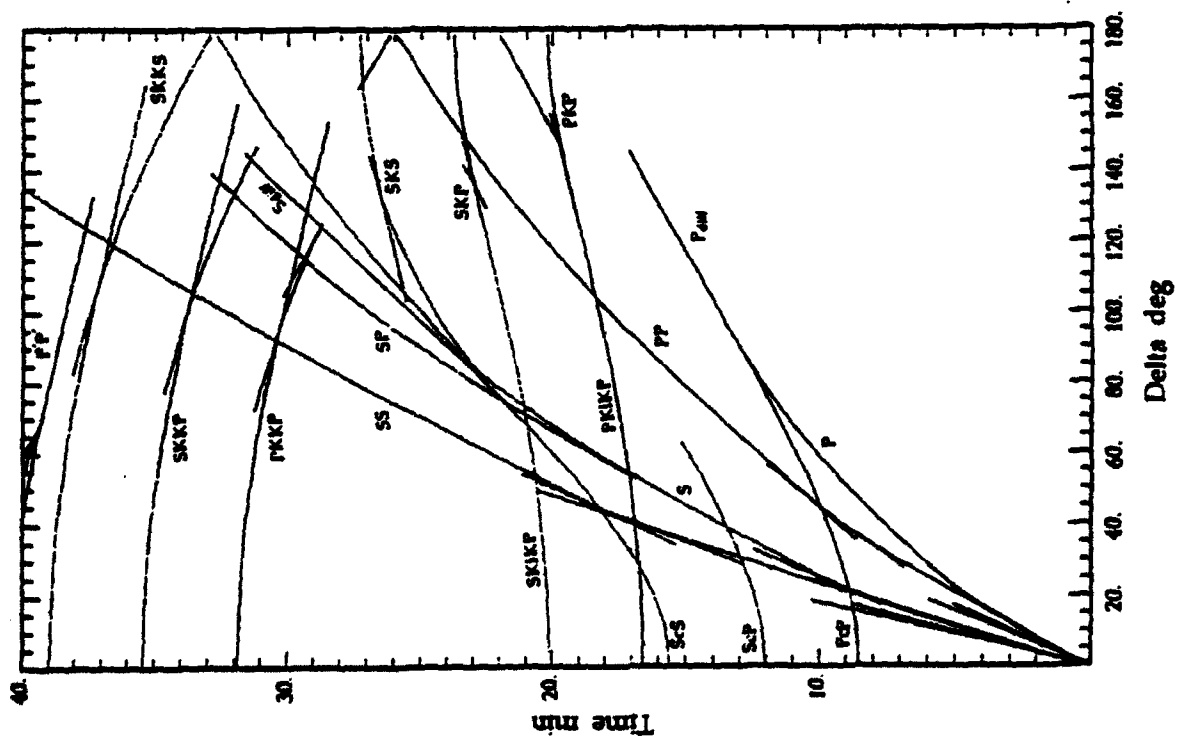
Jost, M. (1992): GERESS P-wave detectability. In: Advanced waveform research methods for GERESS recordings. DARPA Annual Report No. AFOSR-90-0189, Scientific Report No. 2, PL-TR-92-2142, 13-24. ADA253686

Kennett, B. L. N. and E. R. Engdahl (1991): Travel times for global earthquake location and phase identification. Geoph. J. Int. 105, 429 - 466.

Shearer, P. and G. Masters (1990): The density and shear velocity contrast at the inner core boundary. Geoph. J. Int. 102, 491 - 498.

Acknowledgement

I thank Michael Weber for reviewing this paper and the stimulating discussions about core reflections.



GERESS: Events ($\Delta < 35^\circ$, $mb > 5.0$)

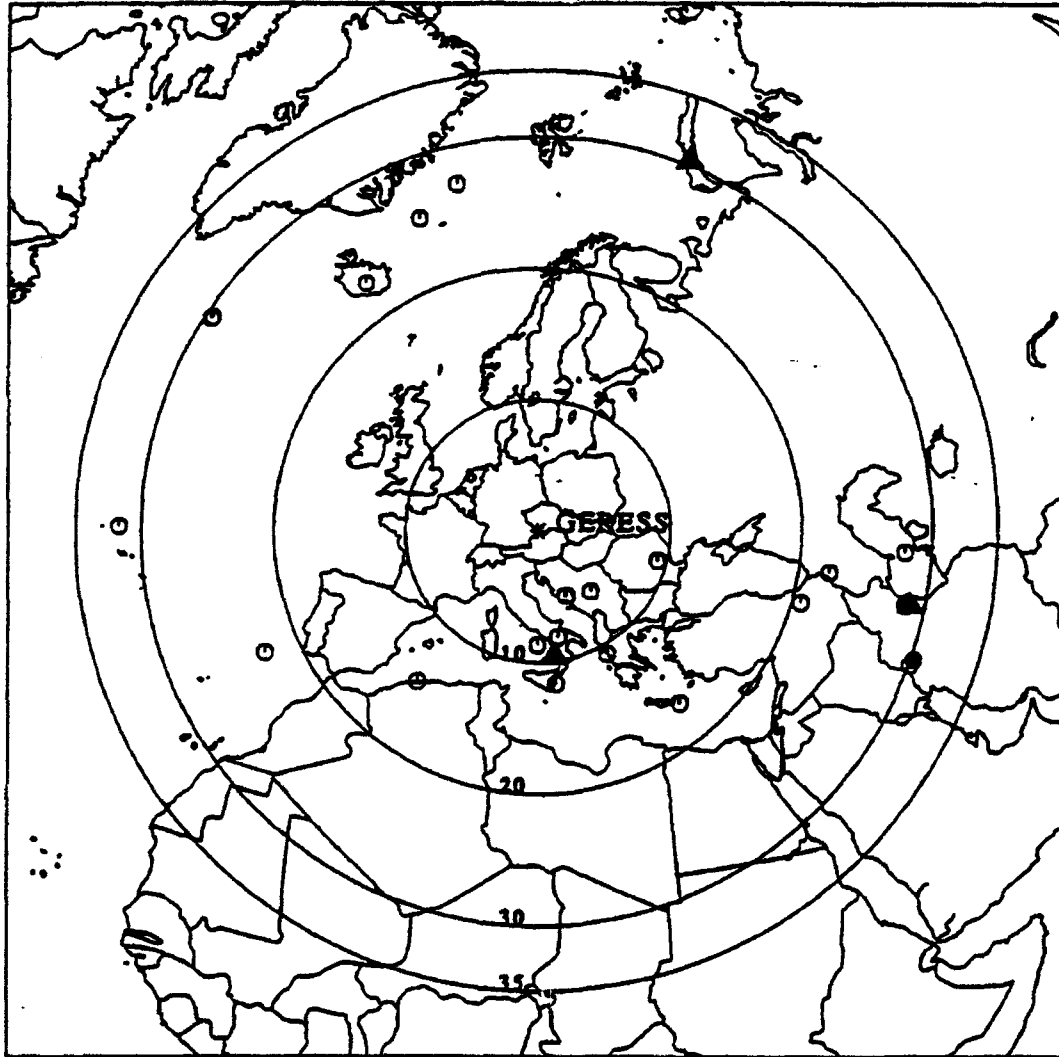


Figure 4-3: Location of events used in this study of PcP. For events with filled triangles GERESS observed a PcP onset. The event with the filled octaeder shows a questionable observation of PcP. For the events with open octaeders no PcP onset could be observed at GERESS. The map is an azimuthal equidistant projection with GERESS in the center. Distances with respect to GERESS are given for $\Delta = 10^\circ, 20^\circ, 30^\circ$, and 35° .

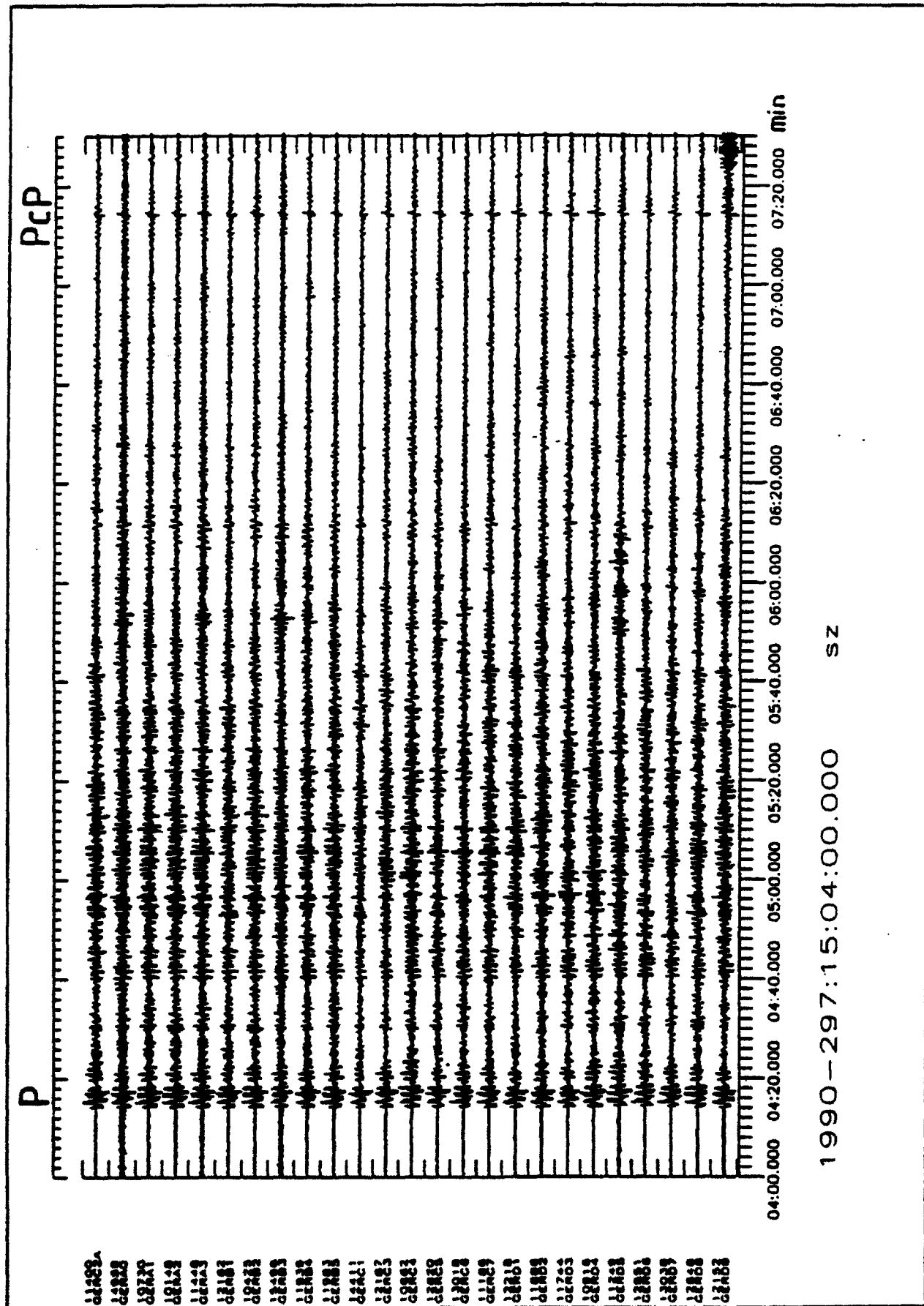


Figure 4-4: Unfiltered GERESS record of P phase and P coda group from the last Soviet Union nuclear test at Novaya Zemlya (October 24, 1990).

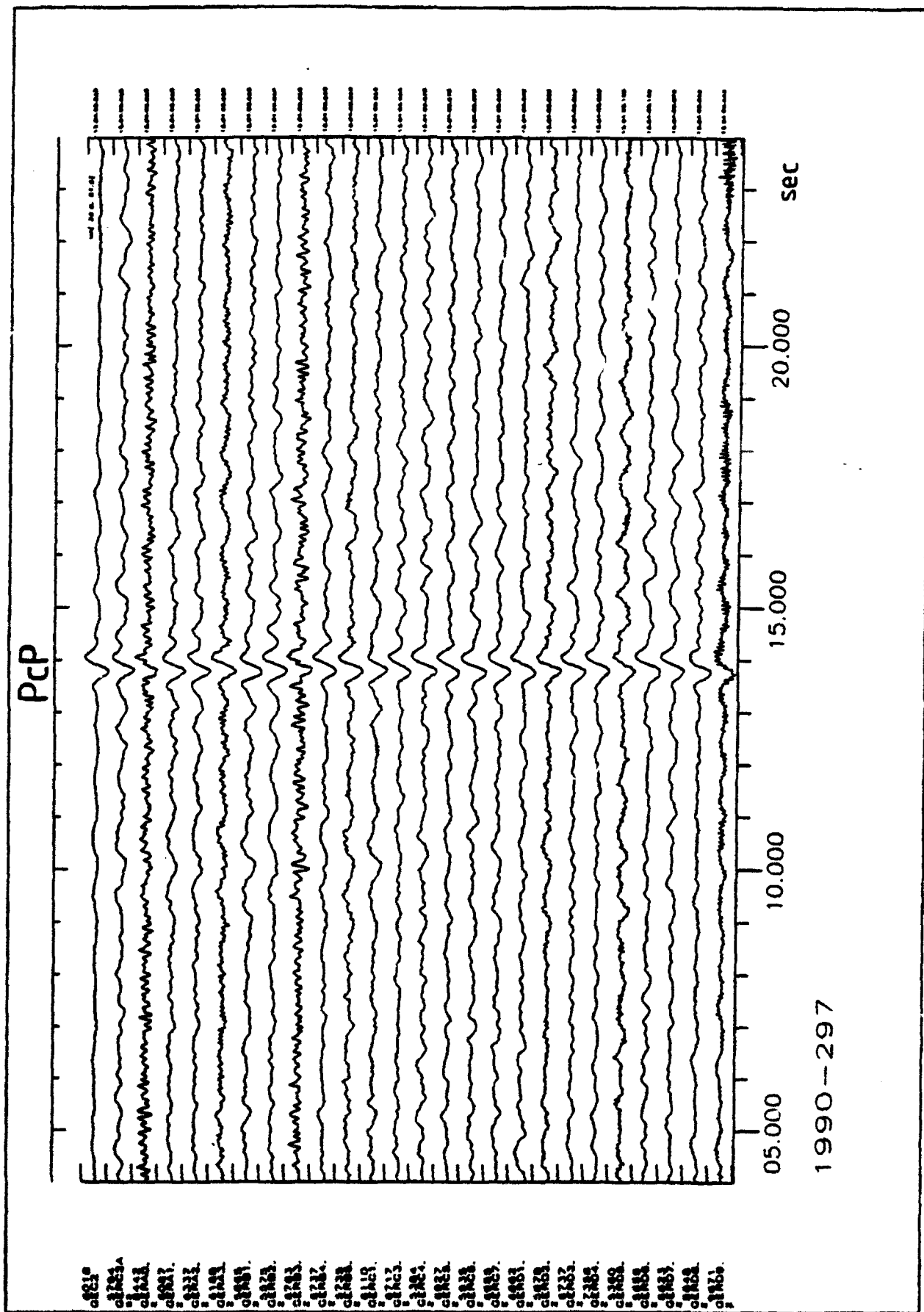


Figure 4-5: Unfiltered PcP phase from the Novaya Zemlya event (Fig. 4-4). At the top the best GERESS PcP beam ($p = 3.05 \text{ sec}^{-1}$, $BAZ = 21.5^\circ$).

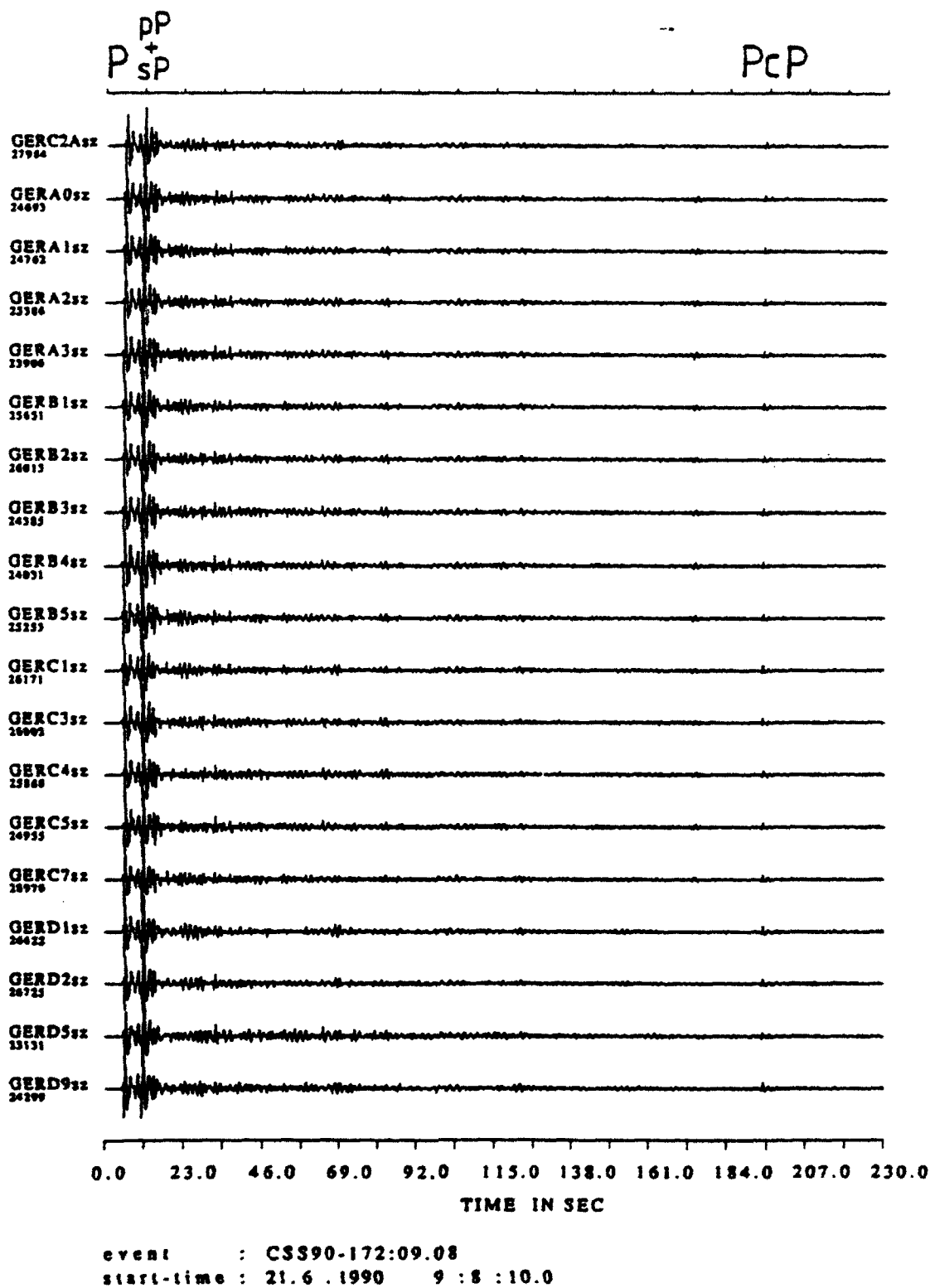


Figure 4-7: Butterworth band pass filtered (0.5z - 2.5 Hz) seismograms of the P, pP, sP, and PcP onsets from the Western Iran event (June 21, 1990).

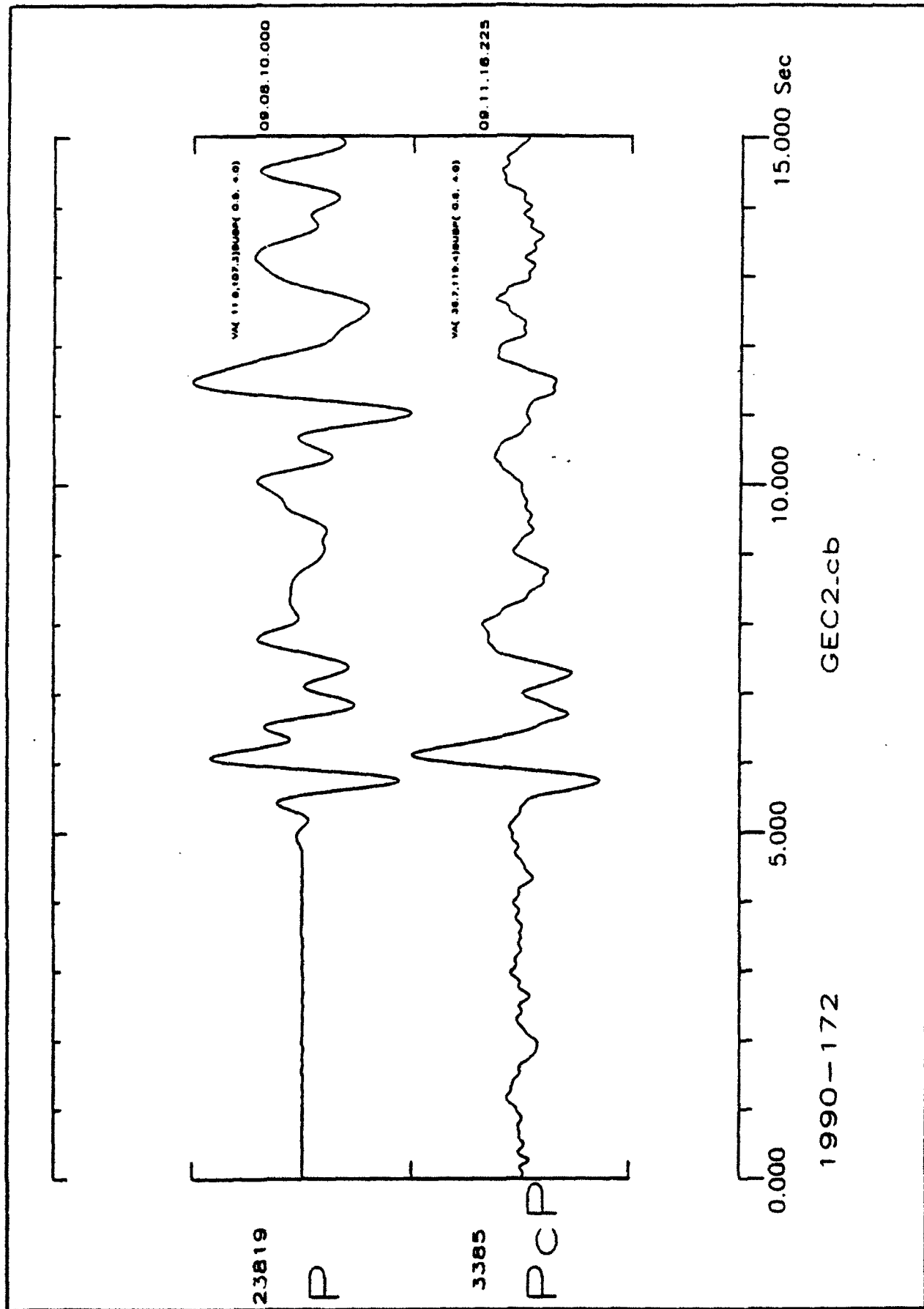


Figure 4-8: Filtered (0.5 Hz - 4.0 Hz) GIERESS beams of P ($p = 9.34$ sec $^{\circ}$, BAZ = 107.3 $^{\circ}$) and PcP ($p = 3.03$, BAZ = 119.4 $^{\circ}$) from the Western Iran event (June 21, 1990).

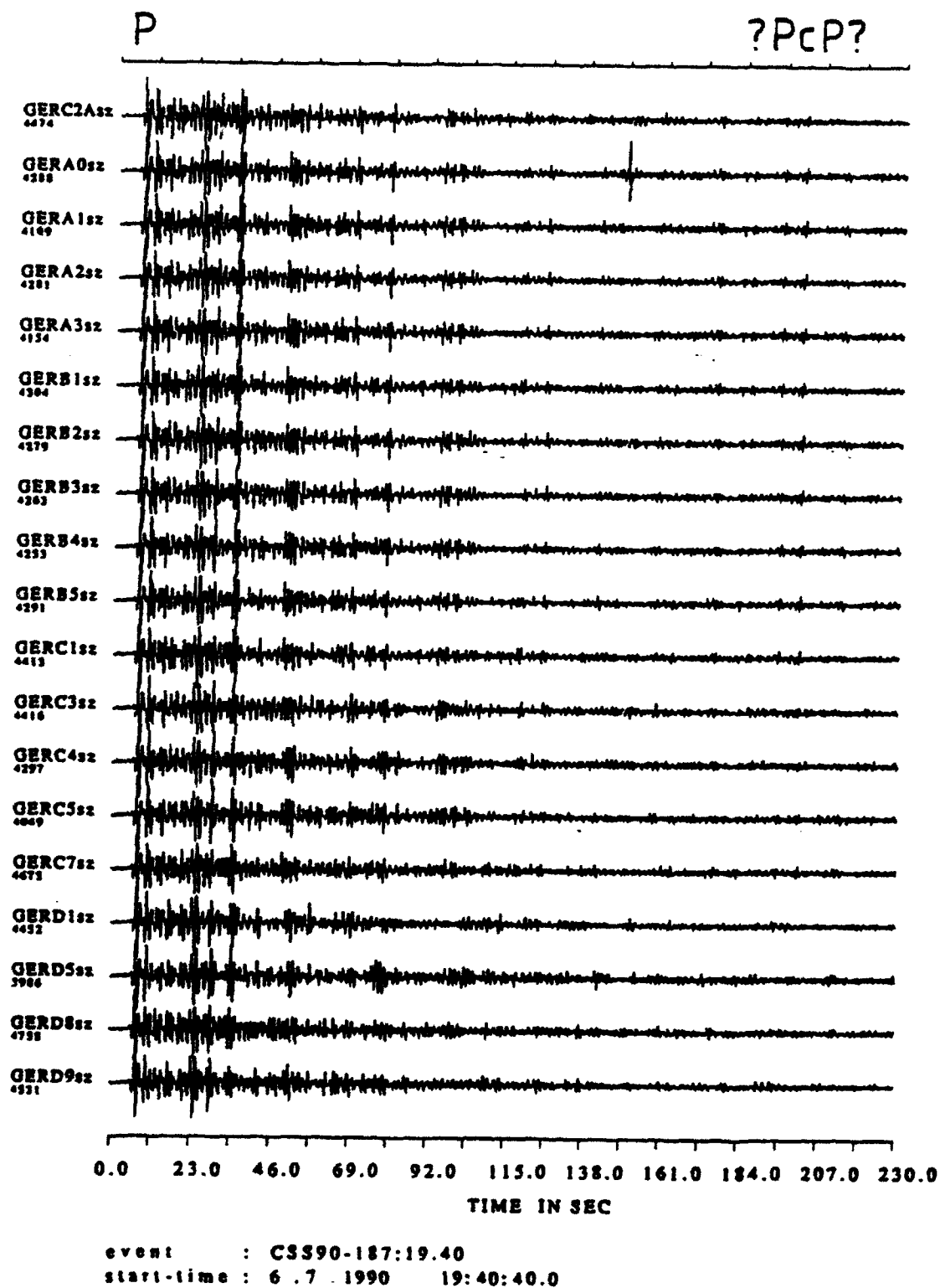


Figure 4-9: As Fig. 4-7, but for the Western Iran event on July 6, 1990. Note the larger P coda with respect to the seismograms in Fig. 4-7.

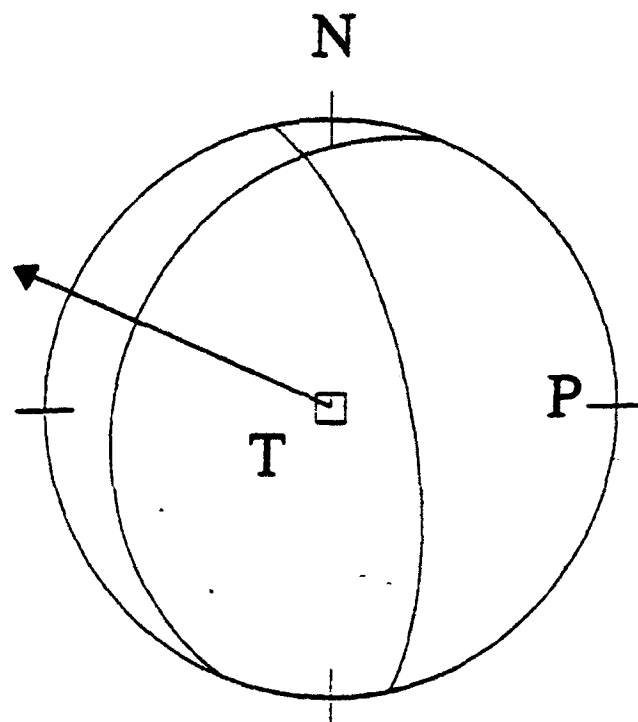


Figure 4-10.a: The Harvard CMT solution of the Western Iran event of June 21, 1990. The arrow shows the direction to GERESS.

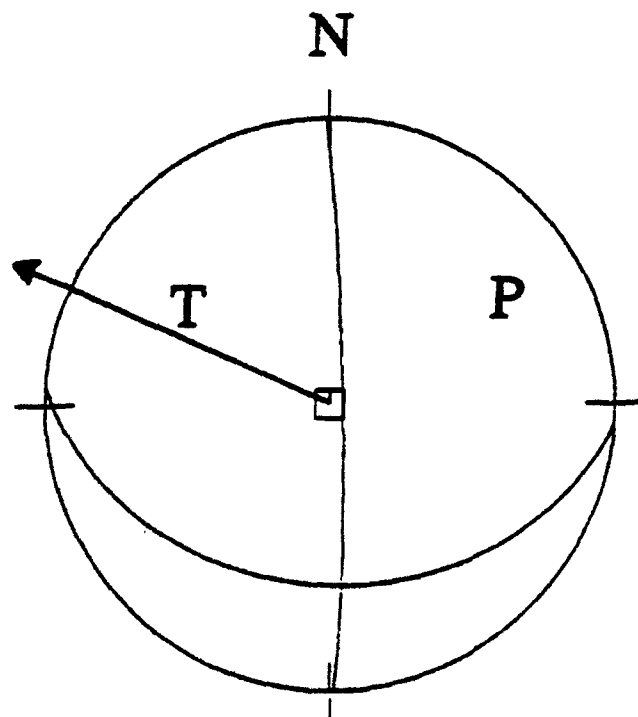


Figure 4-10.b: As Fig. 4-10.a, but for the Western Iran event of July 6, 1990.

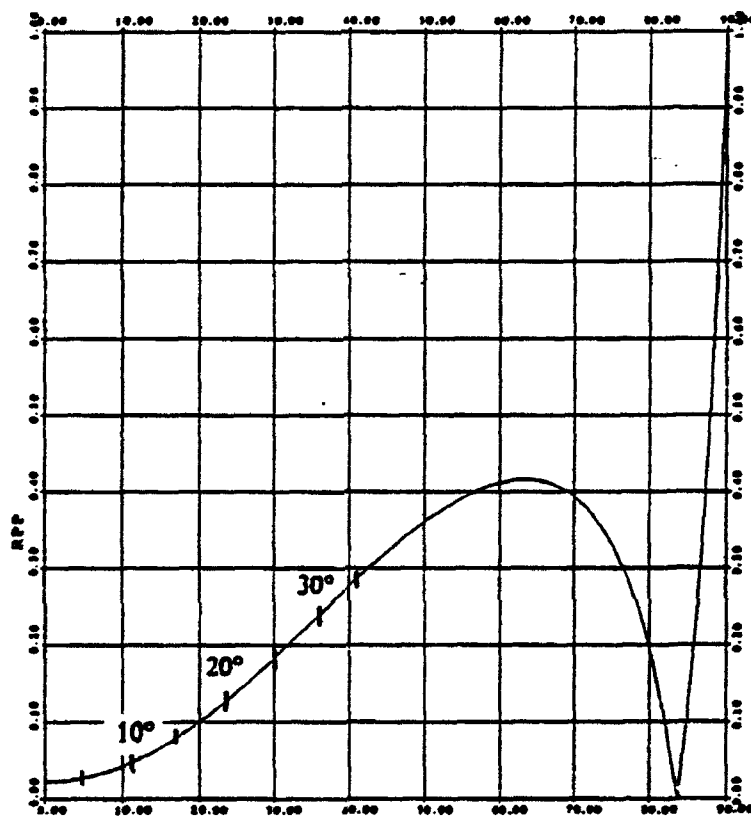


Figure 4-11: Absolute values of the plane wave PcP reflection coefficient at the CMB for PREM (Dziewonski and Anderson, 1981) as function of the angle of incidence at the CMB. Also noted are the epicentral distances corresponding to the angle of incidence.

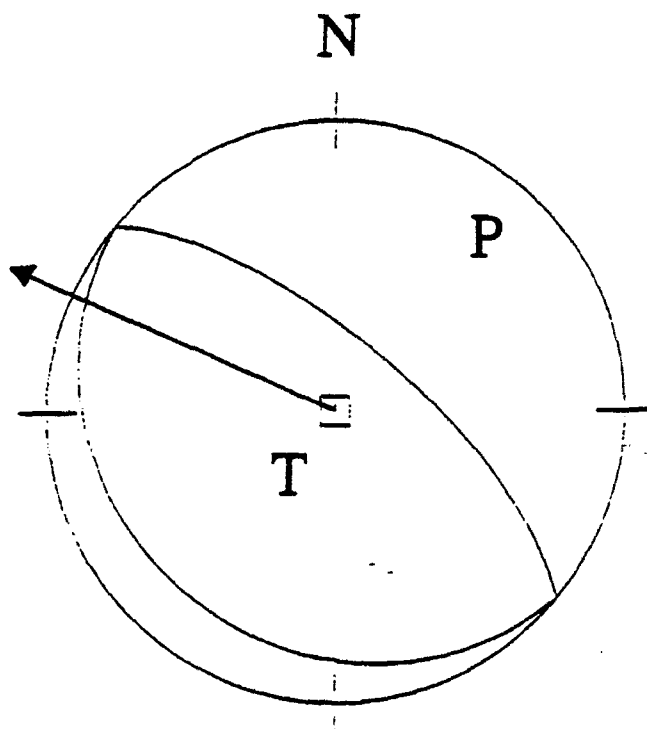


Figure 4-12.a: The first motion focal mechanism published by NEIC for the Romanian event on May 31, 1990

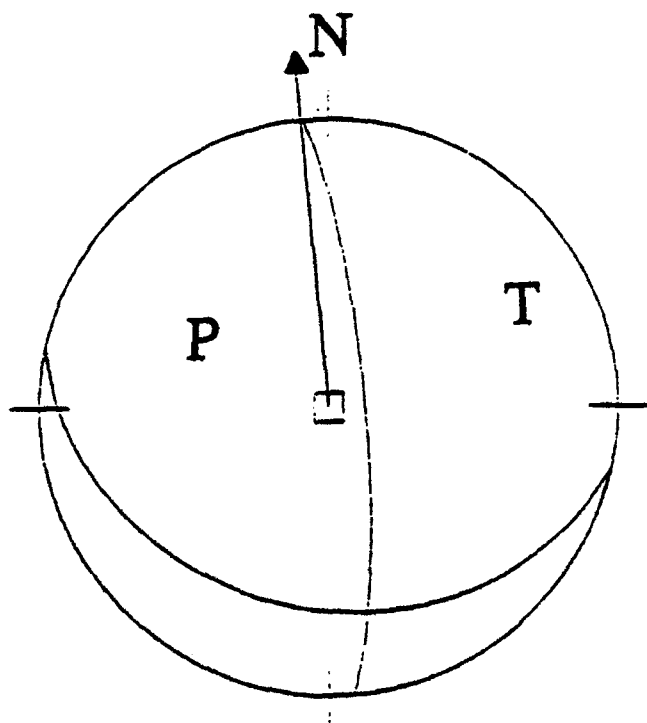


Figure 4-12.b: The focal mechanism for the event on December 14, 1990 calculated with the first motion data published in the ISC Bulletin.

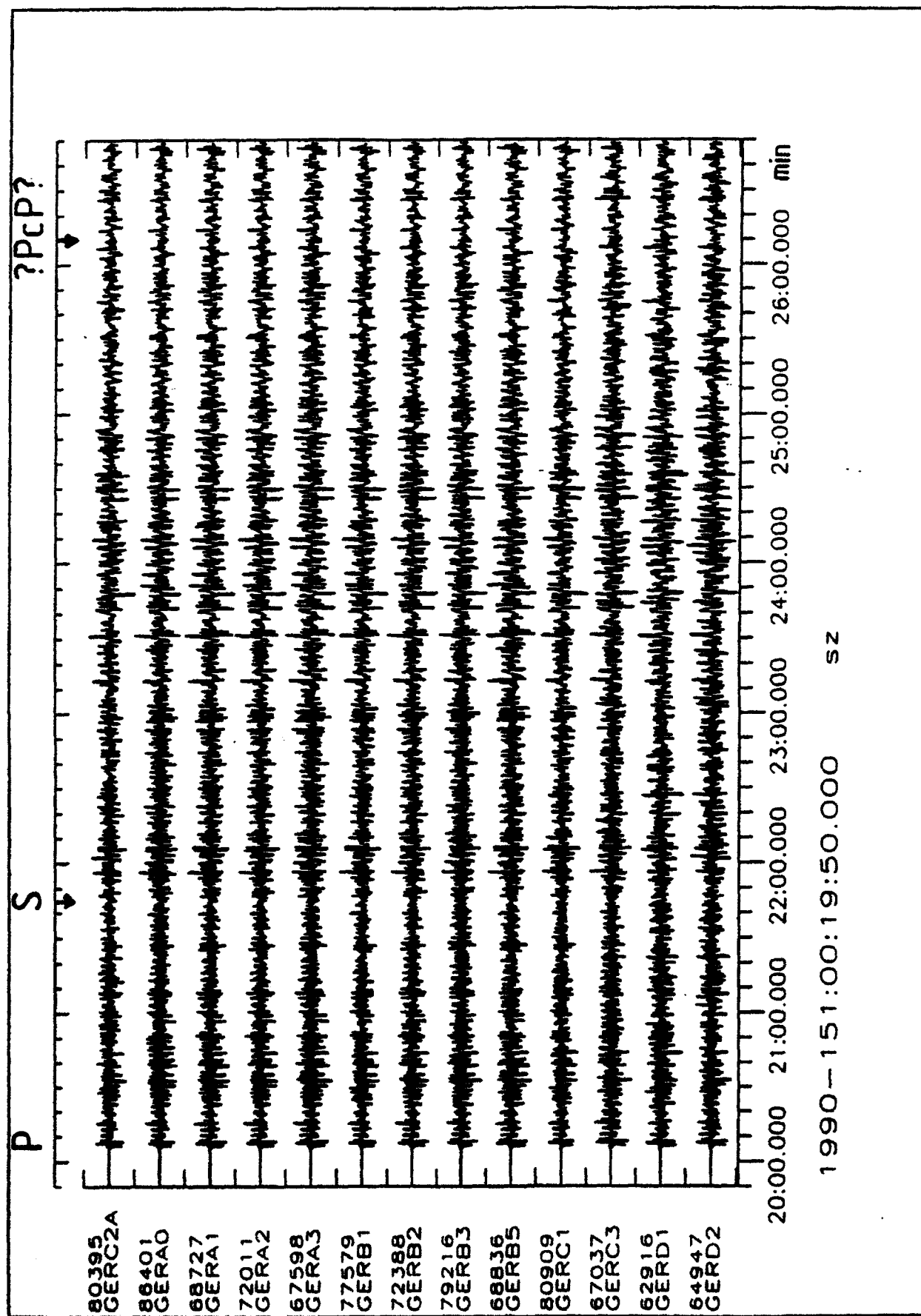


Figure 4-13: Unfiltered seismograms of the Romanian event on May 31, 1990 as recorded with the GERESS array.

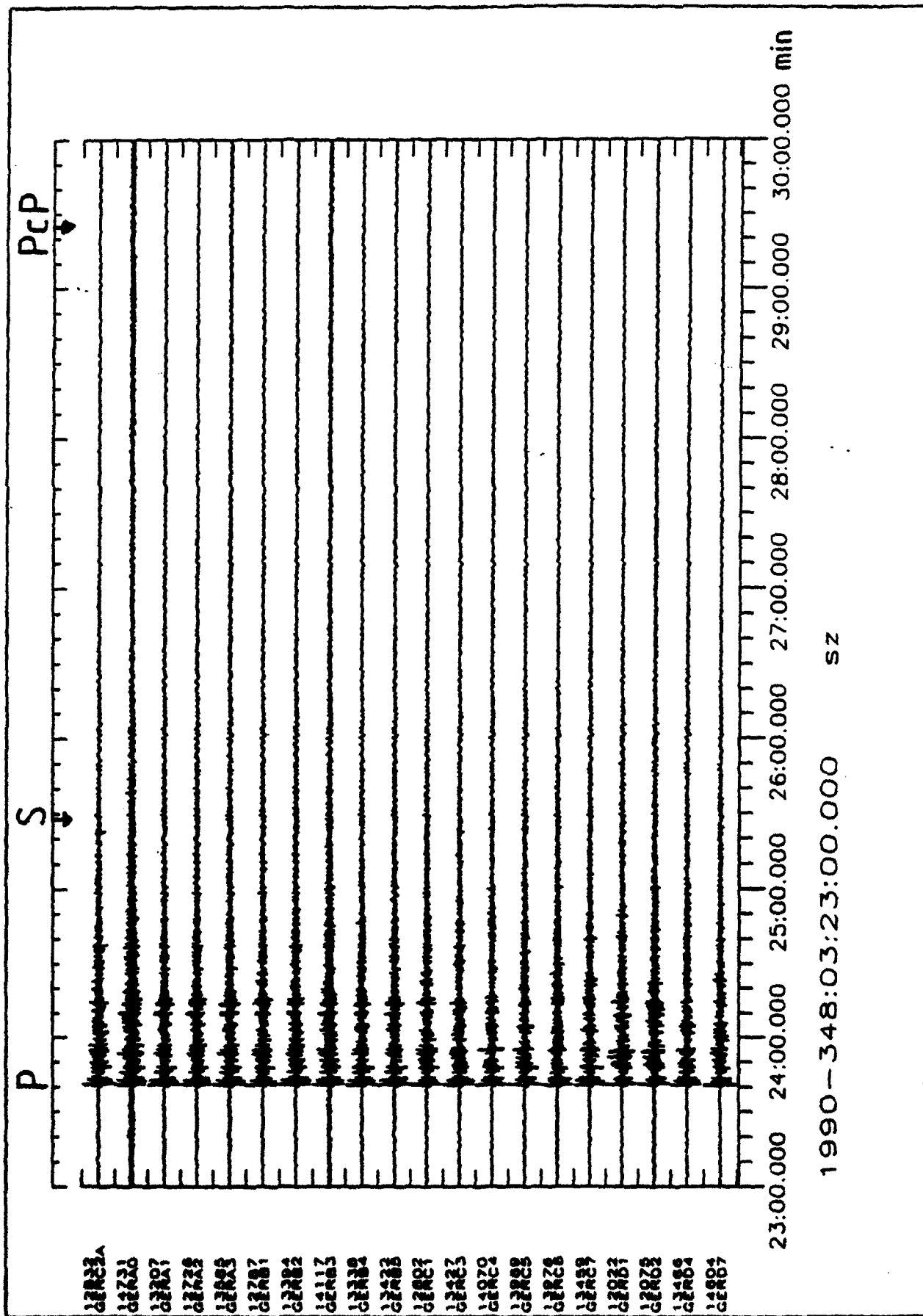


Figure 4-14: As Fig. 4-13, but for the Southern Italy event on December 14, 1990.

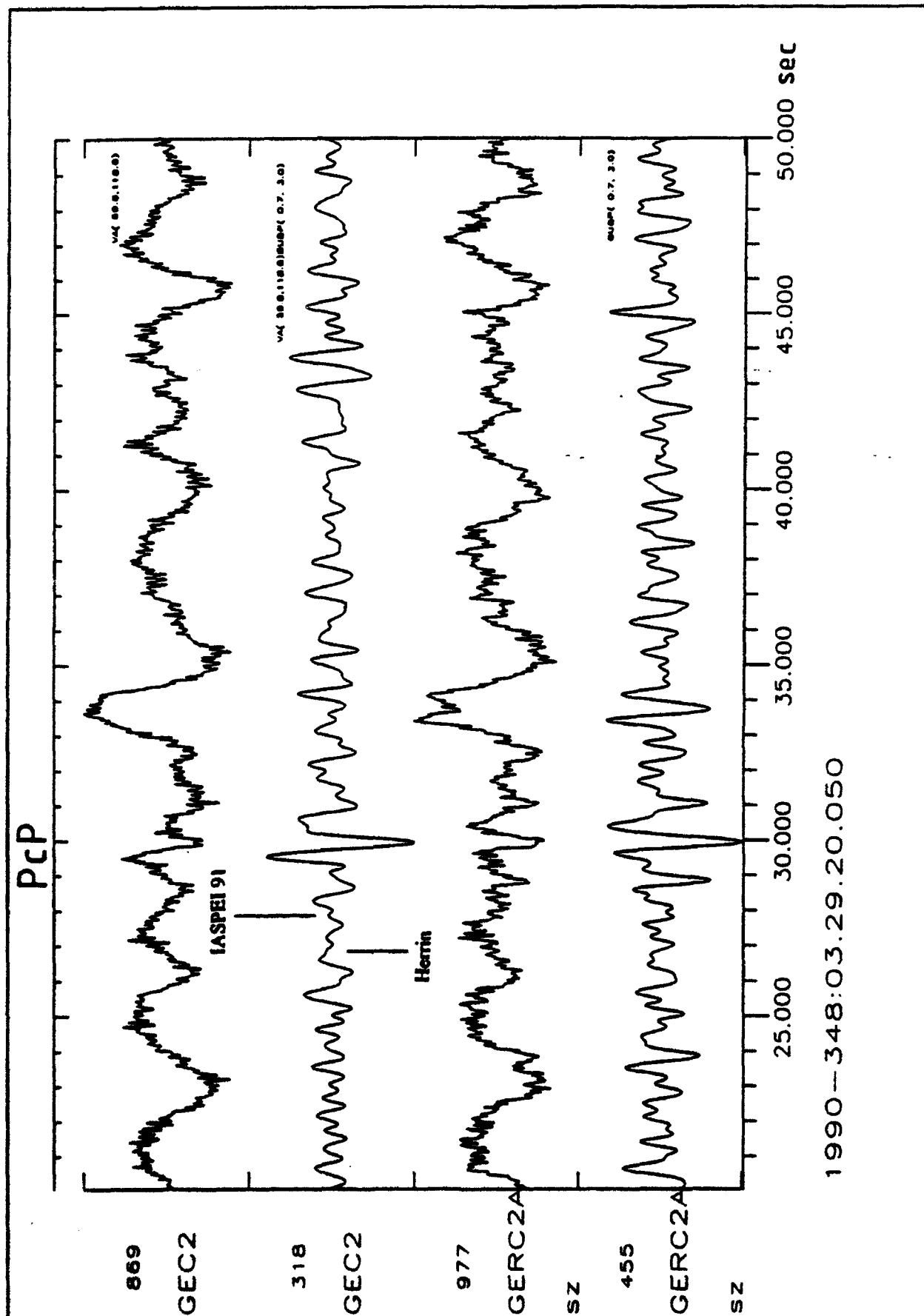


Figure 4-15: Seismograms of the PcP onset for the event of December 14, 1990. Two traces (at the top) show the GEPRESS PcP beam unfiltered and filtered (0.7 Hz - 3.0 Hz). The two lower traces show the record of the GEPRESS reference site GEC2 (unfiltered and filtered). Theoretical onset times for PcP are given relative to the direct P wave for the "1968 tables" (Herrin et al., 1968) and for the IASP91 tables (Kennett and Engdahl, 1991).

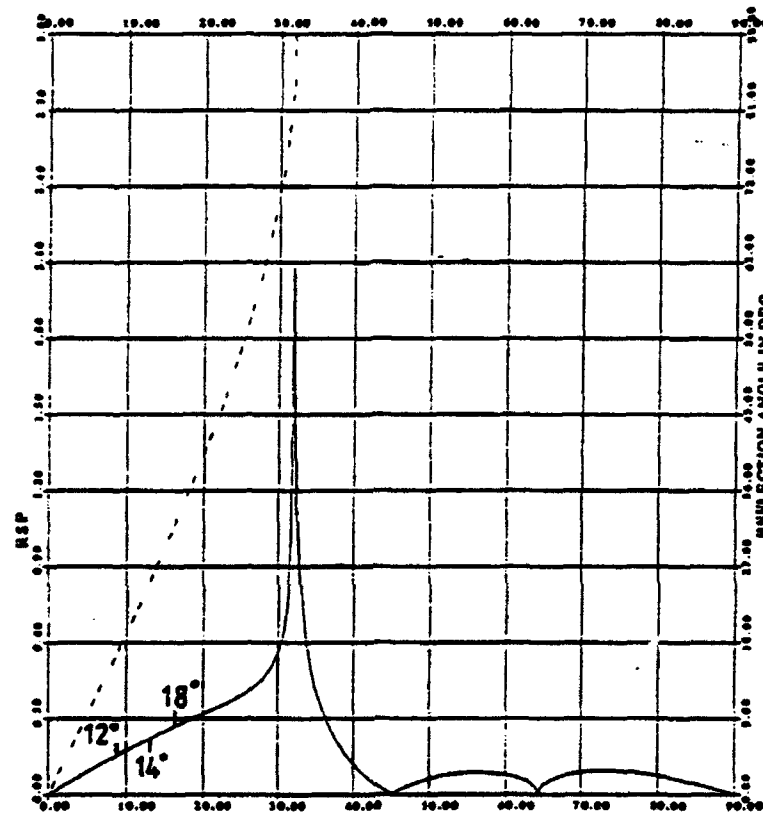


Figure 4-16: The absolute value of the plane wave reflection coefficient of ScP (left y-axis) at the CMB for PREM as a function of incidence. The broken line gives the angle of emergence at the CMB (right y-axis) and the corresponding epicentral distances are marked.

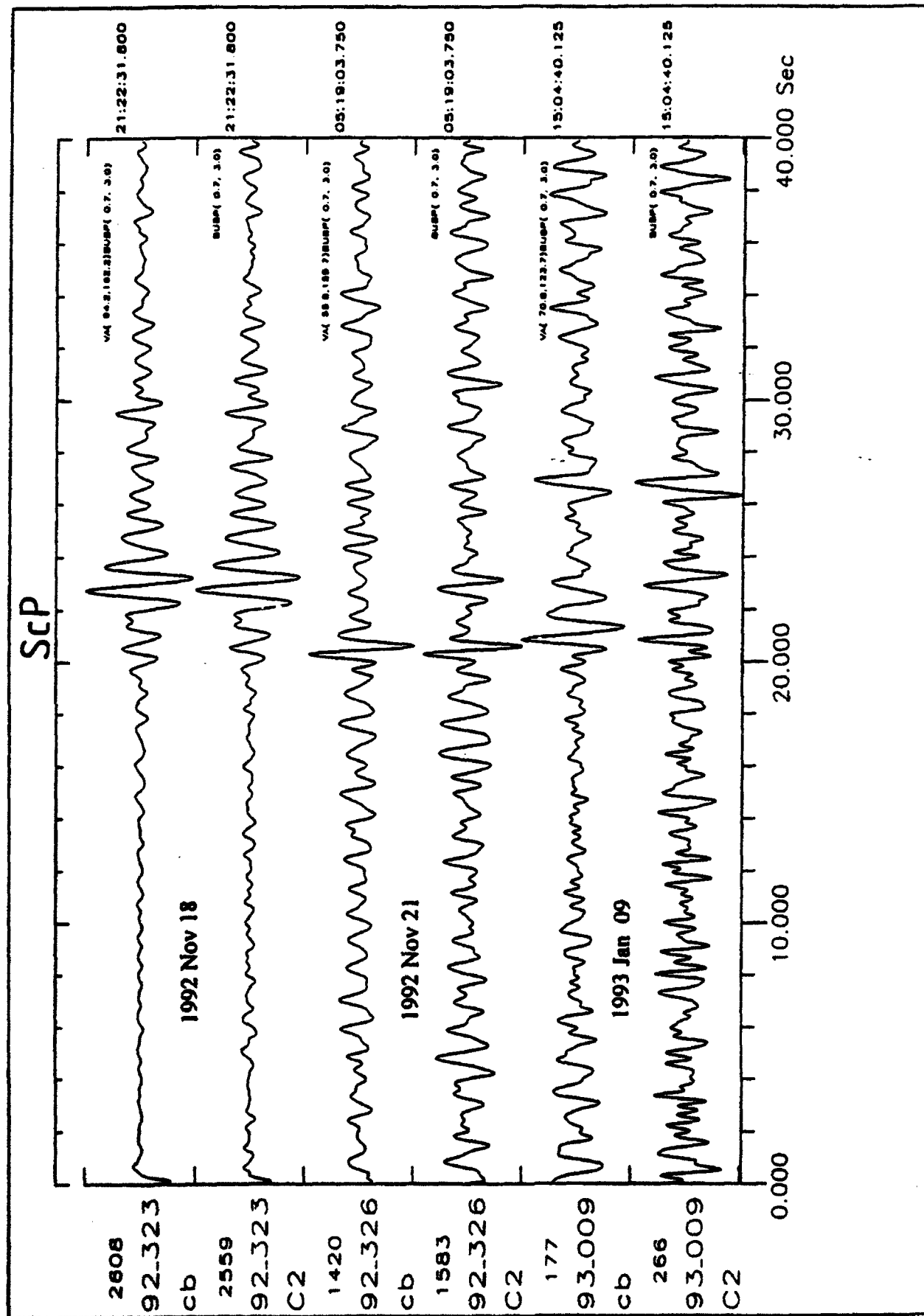


Figure 4-17: Butterworth band pass filtered (0.7 Hz - 3.0 Hz) GERESS beams (top) and scismograms at the GERESS reference station GEC2 (bottom) of the three ScP onsets.

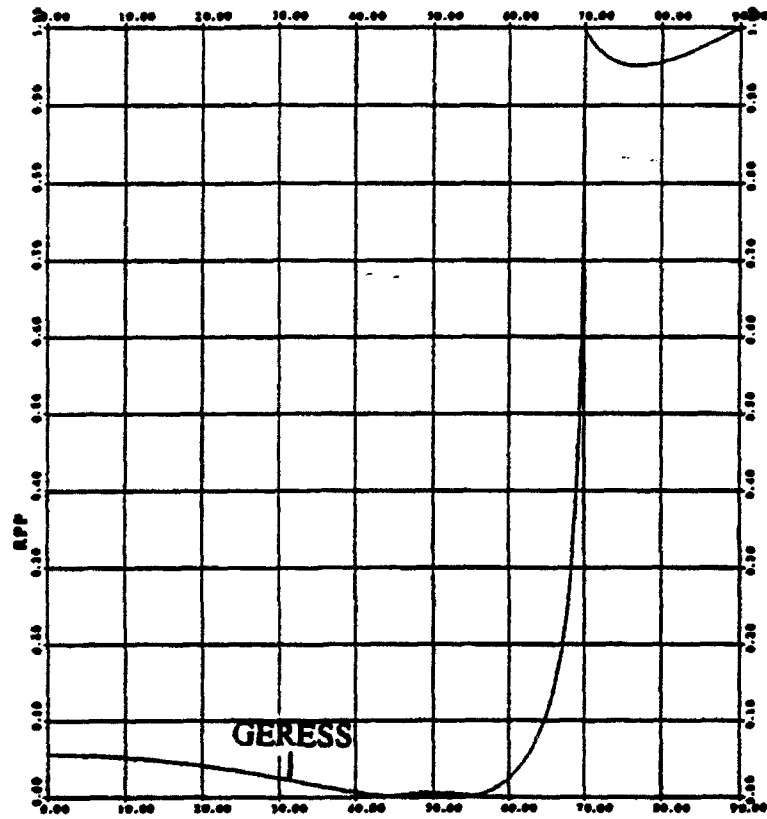


Figure 4-18: The absolute value of the plane wave reflection coefficient of PKiKP at the ICB for PREM. The incidence angle at the ICB for the observed PKiKP onset at GERESS is marked.

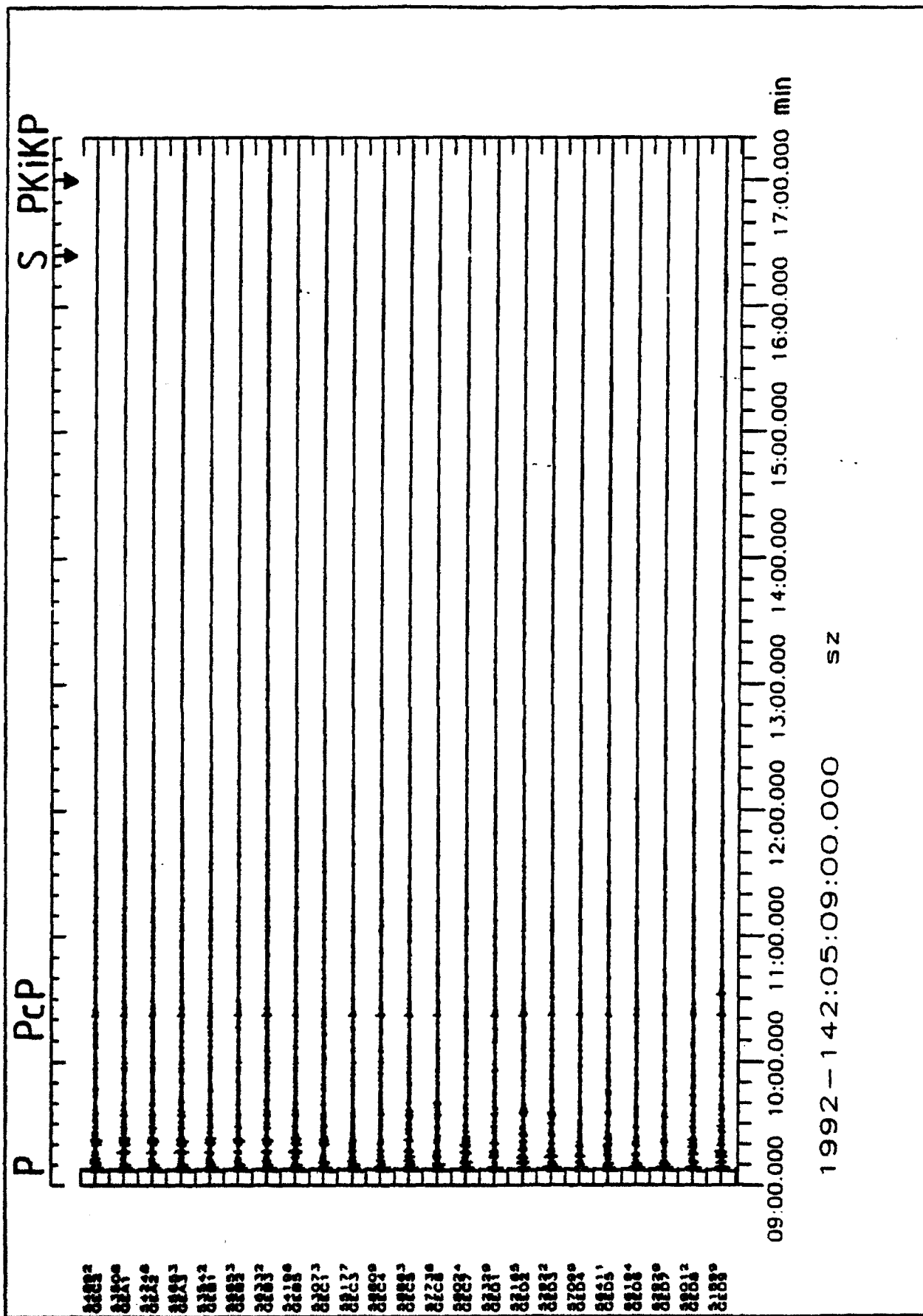


Figure 4-19: The GERESS seismograms of the Lop Nor nuclear test on May 21, 1992.

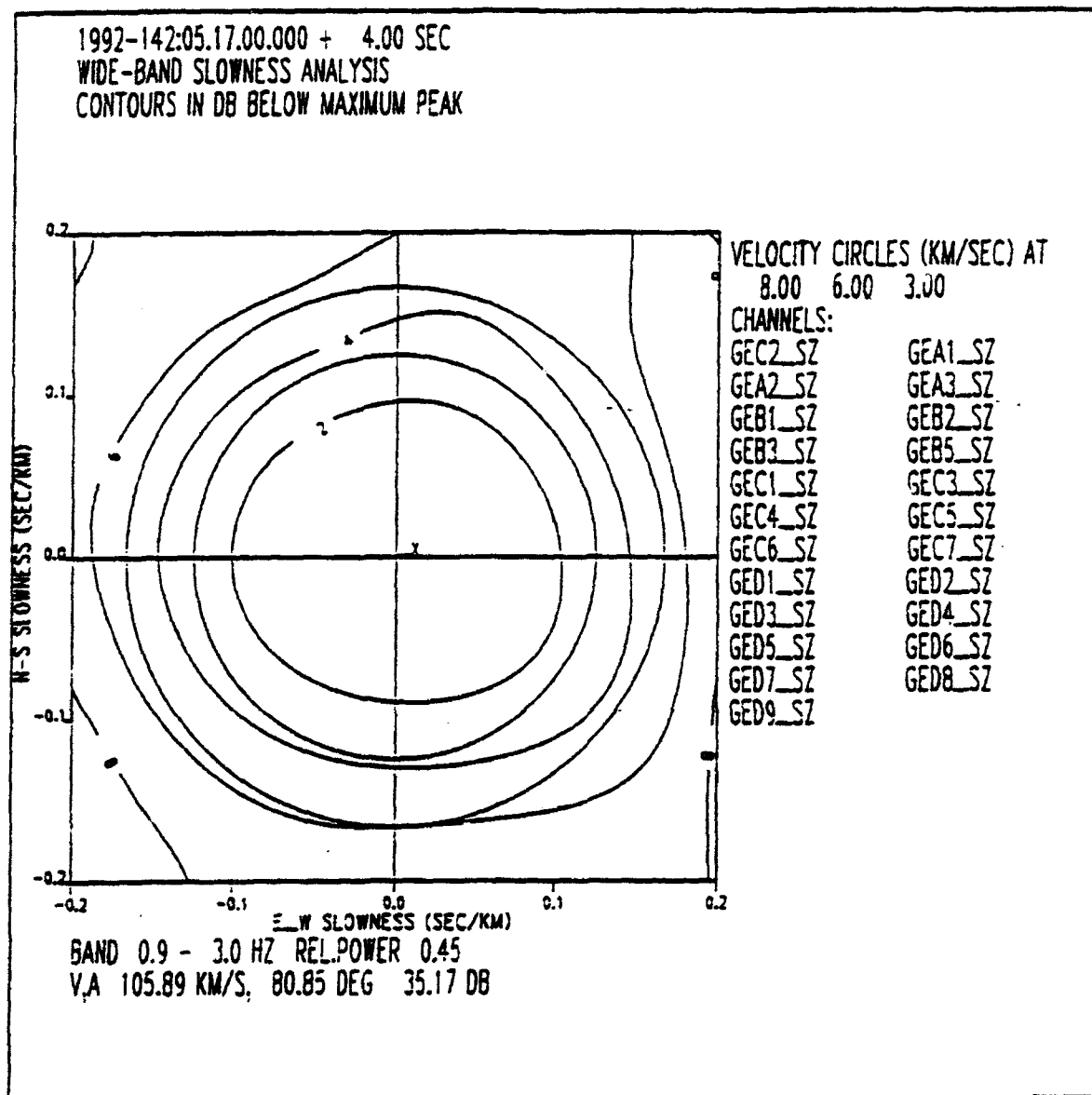


Figure 4-20: The result of the fk-analysis in the time window of the PKiKP onset.

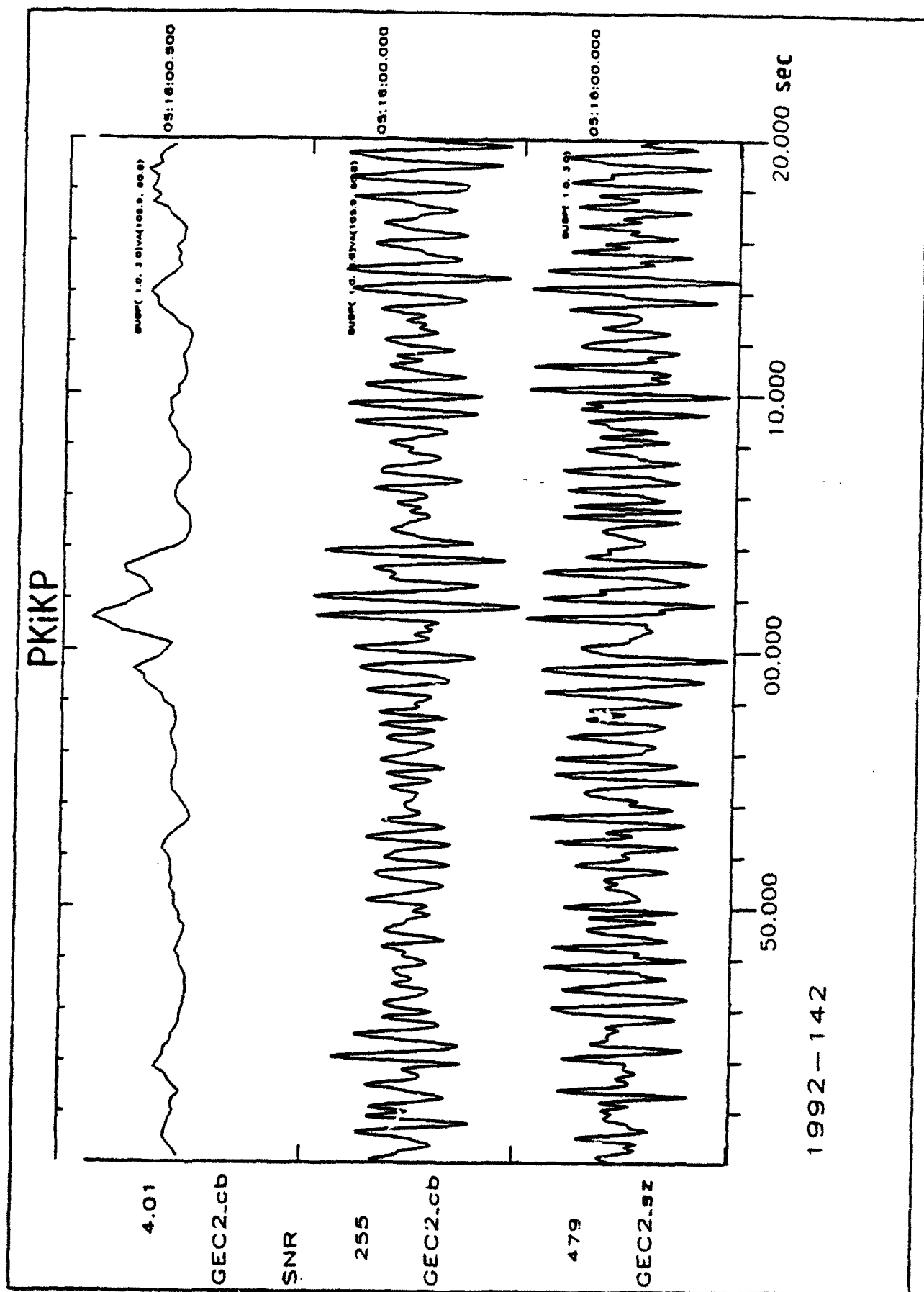


Figure 4-21: The PKiKP onset observed at the GIERISS array. The bottom trace shows the data of the GIERISS reference site GEC2, the trace in the middle shows the GIERISS beam of PKiKP onset, and at the top the SNR trace for the later is seen. The data are band pass filtered ($1.0\text{ Hz} - 3.0\text{ Hz}$).

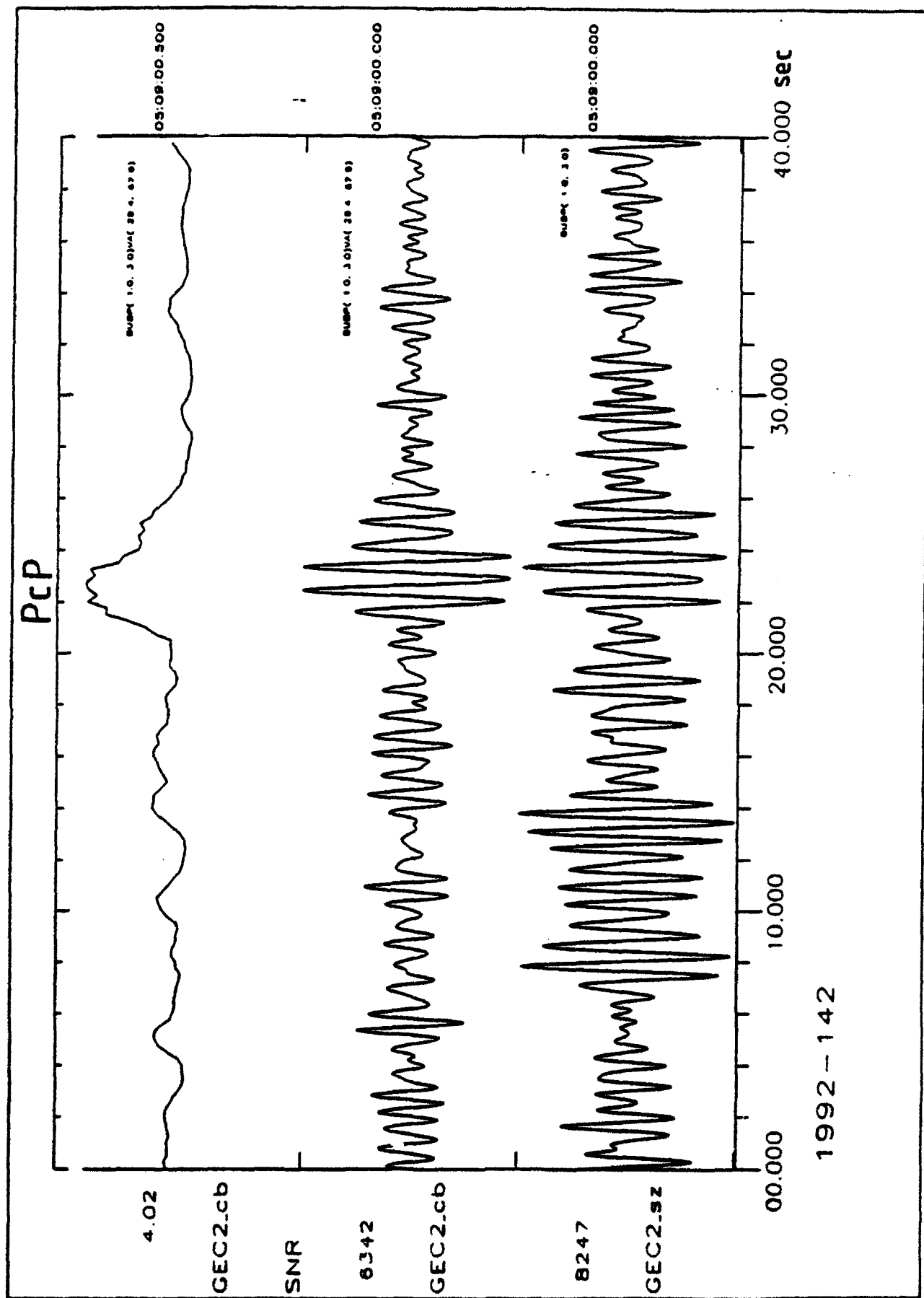


Figure 4-22: As Fig. 4-21, but for the PcP onset.

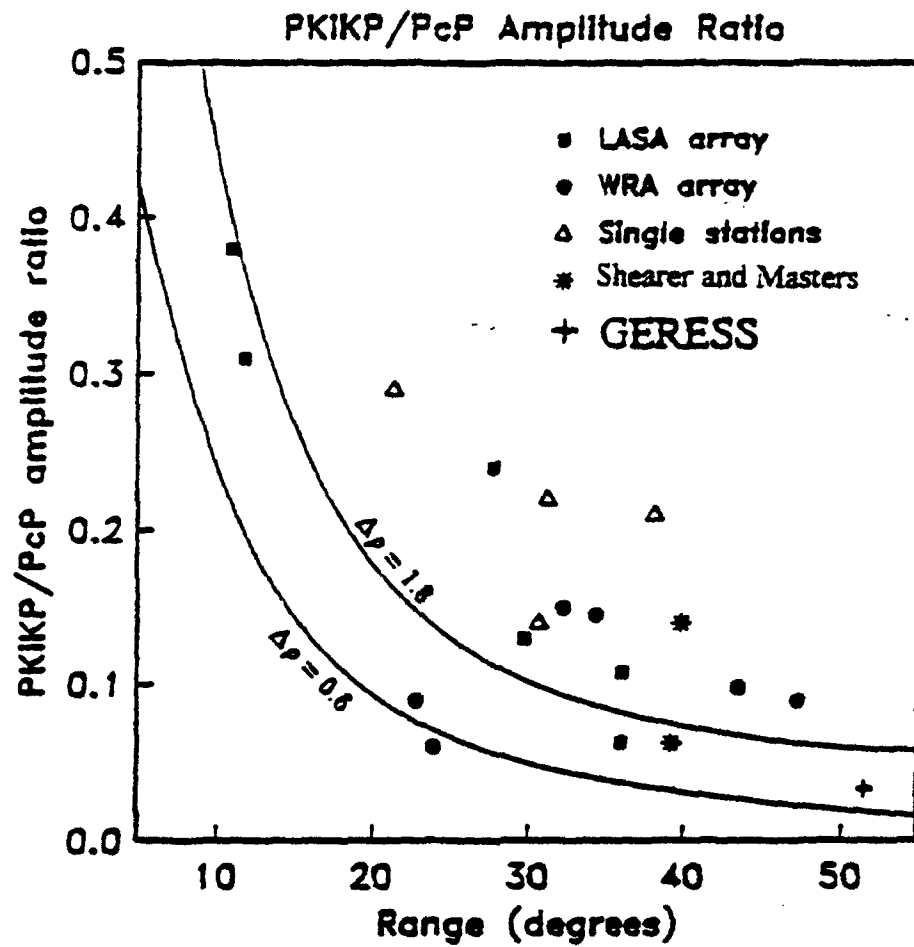


Figure 4-23: Comparison of the PKiKP/PcP observation at GERESS with other published values (modified after Shearer and Masters, 1990).

5. GERESS RECORDINGS OF PRESUMED NUCLEAR TESTS IN 1992

Johannes Schweitzer

5.1 Introduction

In 1992, presumed nuclear explosions were detected from only two test sites: Nevada and Lop Nor. This chapter is the continuation of former reports (Schweitzer, 1991; Schweitzer et al., 1992) on nuclear tests observed with the GERESS array. The known or presumed nuclear tests in 1992 are listed in the following Table 5-1.

Table 5-1: Presumed or confirmed nuclear tests in 1992 and the number of observations at the GERESS array sorted for the different test sites.

Country	Test Site	Epicentral Distance	# of Tests	# of GERESS Registrations
China	Lop Nor	51.4°	2	2
USA	Nevada	83.5°	6	2 (3)

The differences between the total number of tests (8) and events recorded with a clear onset (4) is caused by tests, which were too small to produce an observable signal at the GERESS site. All observed GERESS parameters of the 5 nuclear test in 1992 are listed in Table 5-2. In the following, the observed data will be shown test site by test site. As in former reports, all data are given with respect to the GERESS key station GEC2 and all parameters are measured on the GERESS beams.

Table 5-2: Observed parameters of presumed or confirmed nuclear tests as recorded at GERESS in 1992.

Location	Date	Onset Time	Amp [nm]	Period [sec]	SNR	m _b	BAZ [°]	p [sec/°]
Nevada	Mar 26	16:42:29.0	45.2	1.29	42.0	5.6	332.9	3.53
Lop Nor	May 21	05:09:06.3	334.8	0.84	364.0	6.3	65.8	7.23
Nevada	Sep 18	17:12:30.2	1.4	0.97	5.3	4.2	348.3	6.32
Nevada	Sep 23	15:16:30.8	< 0.6	0.71	1.8	< 3.9	(282.4)	(5.63)
Lop Nor	Sep 25	07:09:04.4	6.2	1.33	5.3	4.4	61.8	7.69

5.2 Lop Nor

In 1992, China continued again its nuclear test program. Two presumed nuclear tests occurred at Lop Nor, which both were observed with the GERESS array. With the observation of May 26, 1990, the GERESS data base now contains three explosions from the Chinese test site. The first explosion in 1992 (on May 21) was the largest explosion which was ever observed with broad band stations world wide. This initiated further seismological investigations, some results can be found in Chapter 4 of this report.

Fig. 5-1 shows the GERESS BB13 3-component registrations of the May 21 event. The horizontals were rotated using the theoretical backazimuth. Clearly seen is the large P phase amplitude which dominates the unfiltered seismograms (three top traces). Although for this event relatively large Love waves could be observed (see the three WWSSN simulated traces at the bottom), the classical m_b / M_s ratio ($6.3 / 5.2 = 1.2$) at the GERESS site still confirms the explosion source. To demonstrate the simple pulse form of relatively high frequency for this large event, Fig. 5-2 shows the deconvolved P and PcP onsets. In both cases a long periodic down swing after the first onset is seen, which can be addressed as an effect of the tectonic release related with this event (Gao and Wallace, 1992). Another effect of the tectonic release seems to be the large Love wave amplitudes.

Fig. 5-3 shows the band pass filtered data of the second Chinese nuclear test in 1992. The top trace is again the best GERESS beam. This very small event was detected only at few stations in Europe, as the contributions to the May 1992 EDR show.

5.3 Nevada

From the 6 announced nuclear tests at the Nevada test site in 1992, only two were detected by the GERESS automatic data analysis system. The 4 other tests were too small to get a detectable onset in Central Europe. In one case a small onset with a signal to noise ratio (SNR) of 1.8 became visible on the array beam. But it is very doubtful to claim this onset as an observation. Therefore the observed parameters of this onset are given as upper limits in Table 5-2 and the parameters for calculating the beam are given in brackets.

The data of the two detected Nevada test site events are shown in Fig. 5-5 and Fig. 5-6. The uncertain onset of the small explosion of September 23, 1992 can be seen in Fig. 5-5. Always shown are the band pass filtered traces of the GERESS array with the beam trace at the top.

After 3 years of monitoring the Nevada test site with the GERESS array, the GERESS data base now contains 11 observations in the magnitude range between $m_b = 4.3$ and $m_b = 5.7$.

Literature

Gao, L. and T. C. Wallace (1992): Seismotectonics of the Lop Nor region, Northwest China (abstract). EOS 73, 359.

Schweitzer, J. (1991): Nuclear tests observed with the GERESS array in 1990. In: Advanced waveform research methods for GERESS recordings. DARPA Annual Report No. AFOSR-90-0189, Scientific Report No. 1, PL-TR-91-2134, ADA239199, 56-78.

Schweitzer, J. and M. L. Jost and N. Gestermann (1992): Nuclear tests observed with the GERESS array in 1991. In: Advanced waveform research methods for GERESS recordings. DARPA Annual Report No. AFOSR-90-0189, Scientific Report No. 2, PL-TR-92-2142, 50-59. ADA253686

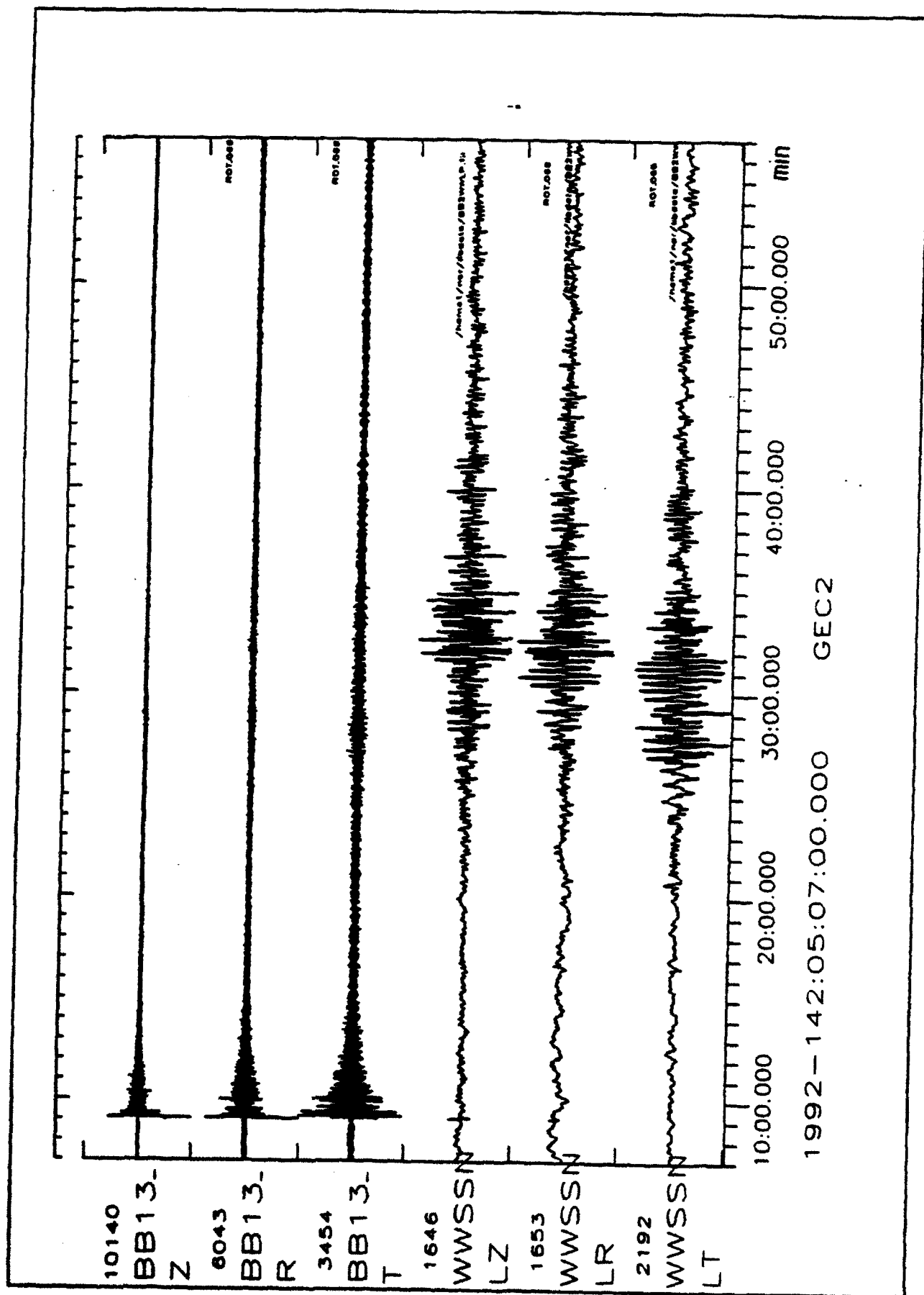


Figure 5-1: GERESS registrations of the Chinese nuclear test on May 21, 1992. Displayed are the original BB13 registrations after rotating the horizontals and the WWSSN simulations respectively.

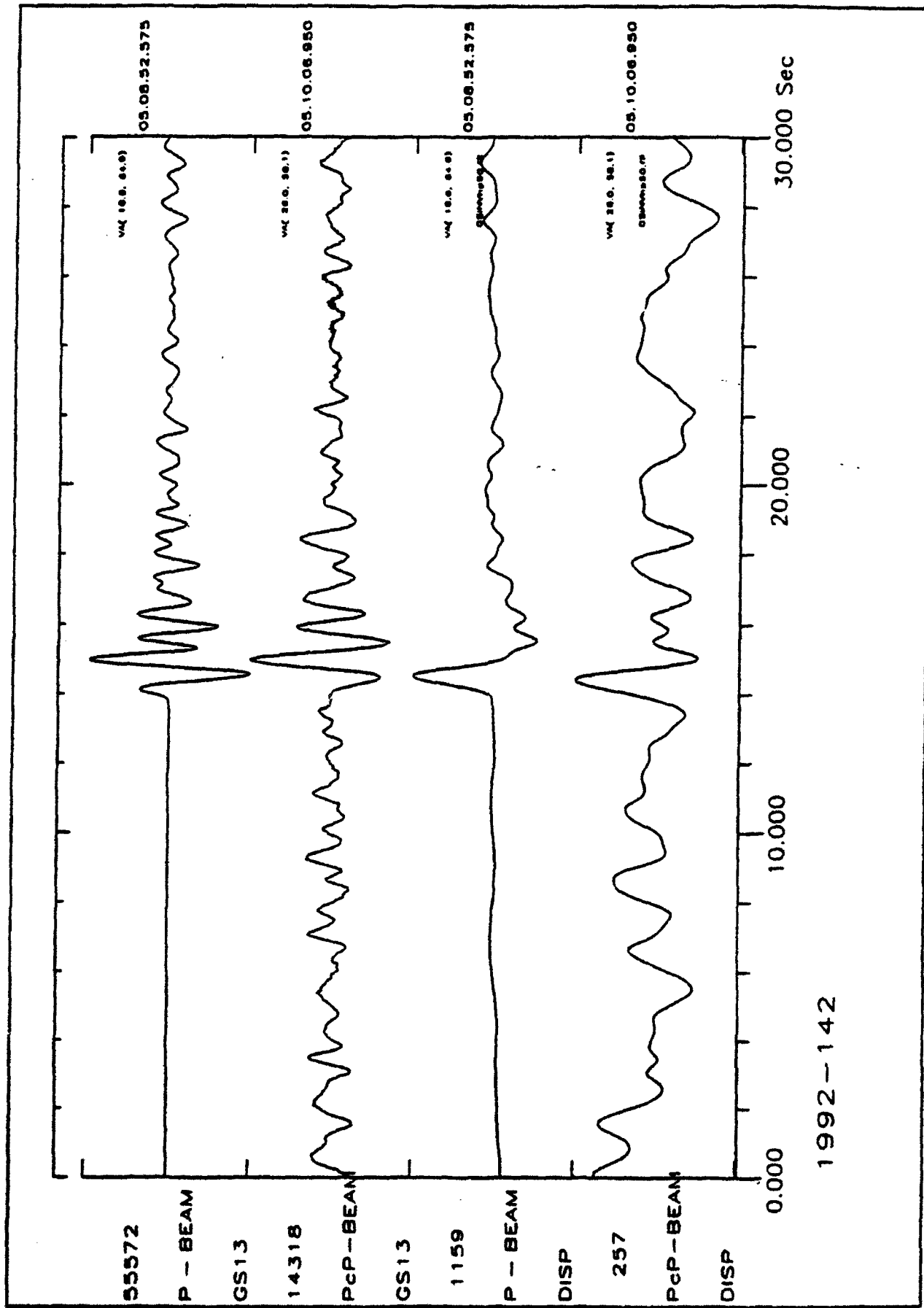


Figure S-2: The unfiltered beams of the P and the PcP onsets of the Lop Nor event on May 21, 1992. Additionally seen are the true ground motion simulations of the two onsets respectively.

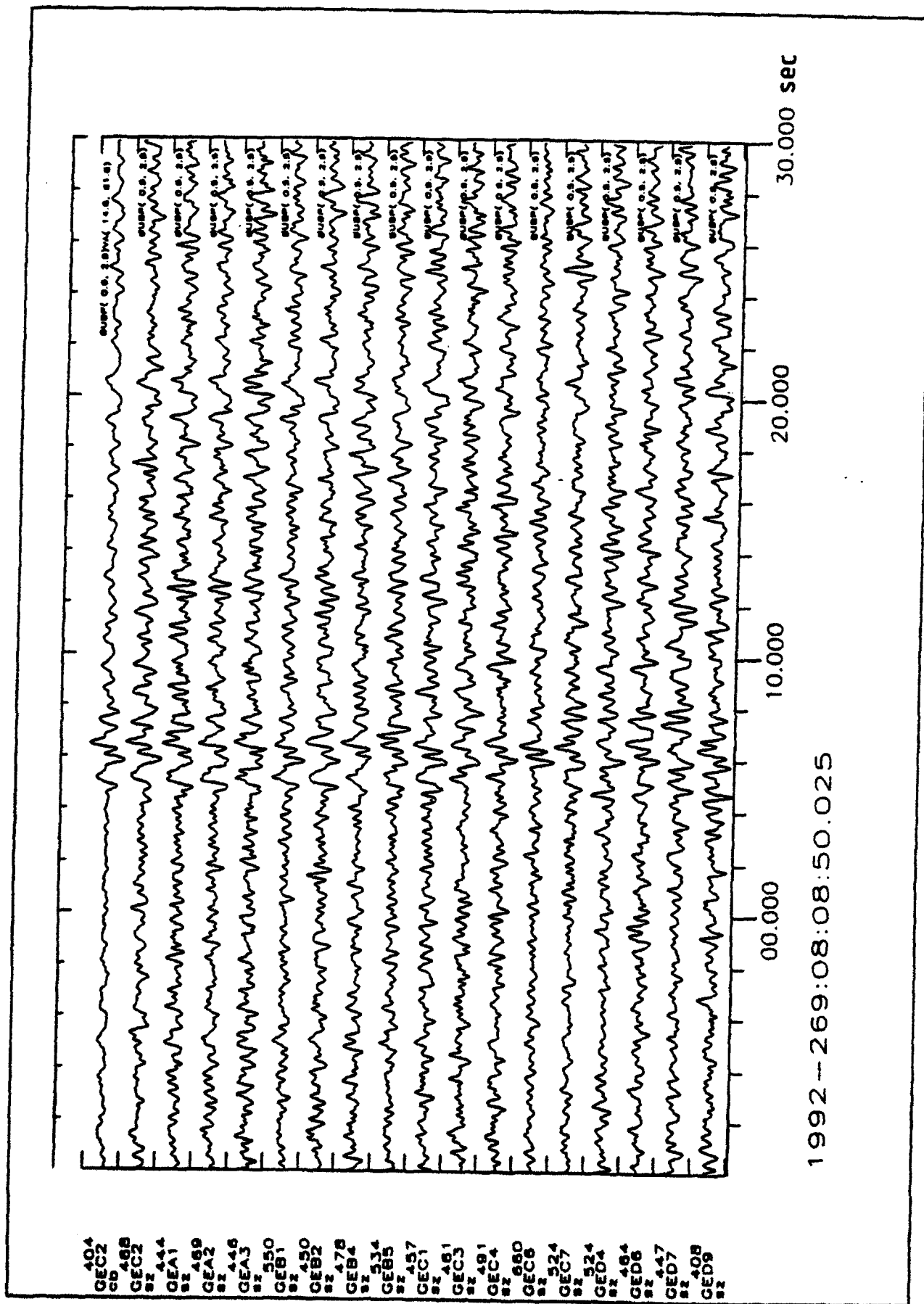


Figure 5-3: The Butterworth band pass filtered (0.5 Hz - 2.5 Hz) registrations of the nuclear test at Lop Nor on September 23, 1993 are shown with the GERSS beam trace at the top.

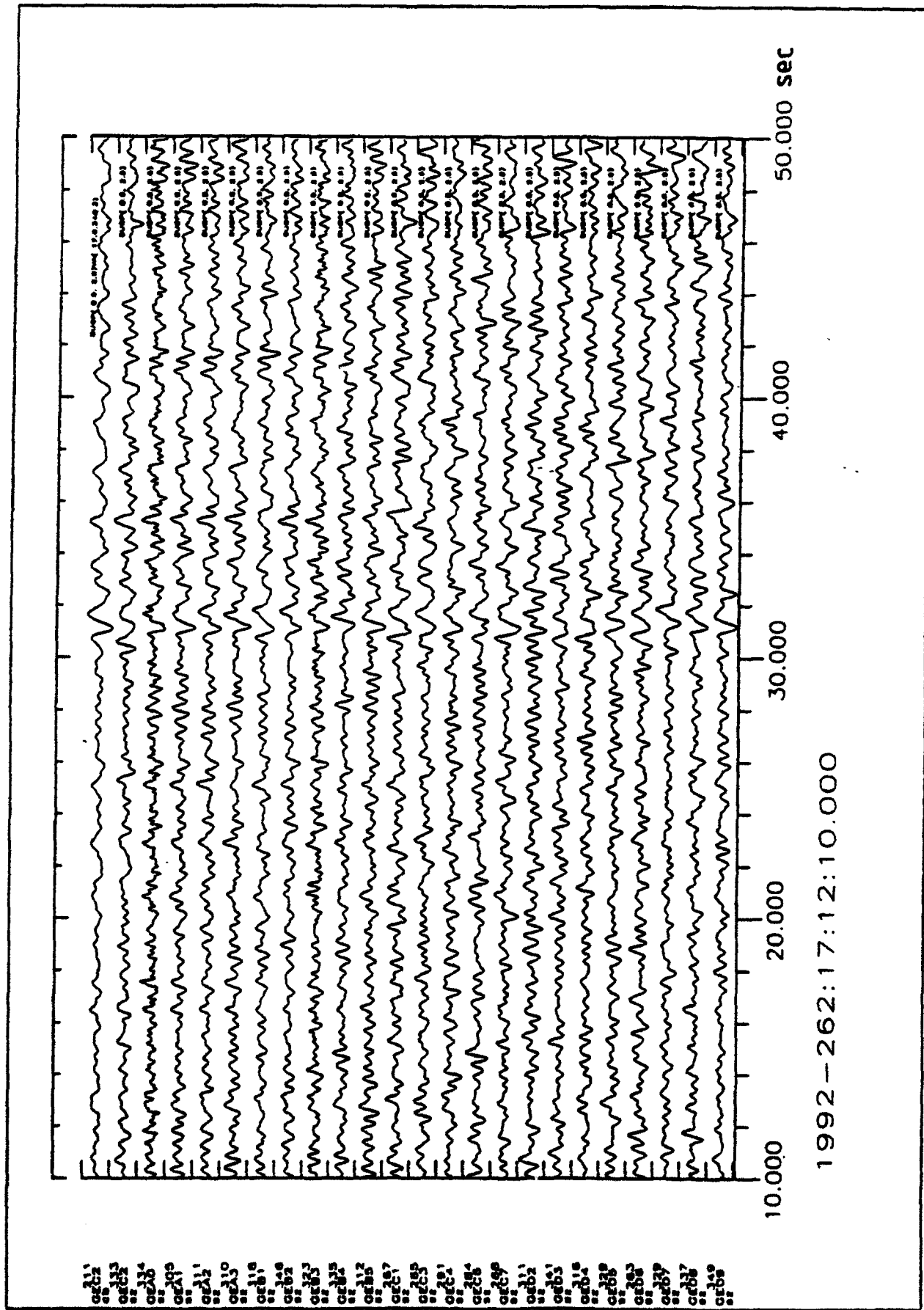


Figure 5-5: As Fig. 5-4, but now for the nuclear test at the Nevada test site on September 18, 1992.

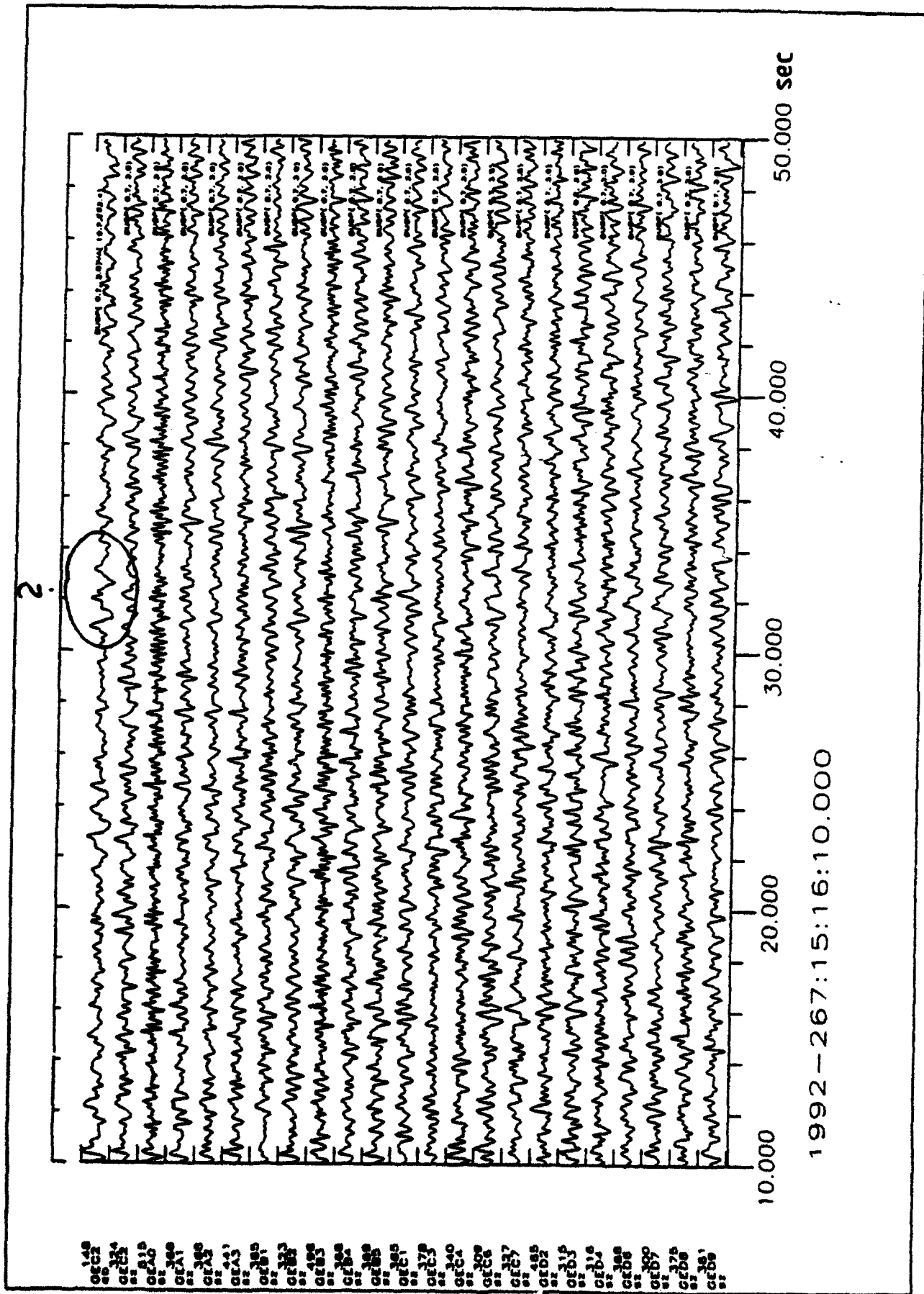


Figure 5-6: Butterworth band pass filtered ($0.7\text{ Hz} - 3.0\text{ Hz}$) registrations of the nuclear test on September 23, 1992 for the theoretical onset time at the GERESE array.

6. SYNTHESIS OF BROAD BAND DIS- PLACEMENT SEISMOGRAMS FROM BAND LIMITED DIGITAL REGISTRA- TIONS

Jan Wüster

6.1 Summary

With the advent of high resolution analog/digital converters, it is no longer necessary to use broad band seismometers in order to achieve complete coverage of the seismic spectrum. In this paper a method is presented, with which broad band records of true ground displacement can be synthesized using band limited digital registrations obtained from two or more different standard instruments at the same location. This process involves forward recursive filtering only and is thus suitable for on line real time application. Its usefulness is demonstrated in an application to the instruments at the GERESS reference station GEC2.

6.2 Introducing the method

At the beginning of the 1980s, the use of digital broad band seismograph systems was strongly advocated [Harjes, 1981] to achieve both international standardization of seismological records and equal coverage of the whole frequency range of seismic signals (about 0.005 Hz to 50 Hz) without loss of information due to the band limiting properties of standard analog seismic systems widely in use in the 1970s. This approach has led to the establishment of numerous broad band seismological stations and several broad band networks and arrays worldwide. The ORFEUS data center was founded in 1987 and dedicates itself exclusively to the collection and distribution of broad band digital records. Meanwhile, highly resolving analog/digital converters have become available, making the use of broad band seismometers no longer imperative in the pursuit of the goals mentioned above. In fact, broad band (BB) seismograms can be simulated, making use of band limited digital registrations from two or more different standard instruments at the same location, provided their combined pass bands cover the frequency range desired and the resolution of analog to digital conversion is sufficiently high.

The synthesis process involves:

1. Restitution of true (albeit band limited) ground motion by deconvolving system response for each instrument.
2. Adjustment of sample frequencies.
3. Compensation of time shifts.
4. Tailoring individual pass bands.
5. Arithmetic summation of traces.
6. Numerical differentiation in case a velocity or acceleration proportional BB seismogram is to be obtained.

The procedure described below was developed and implemented for instruments installed at the GERESS regional seismic array. It is performed exclusively in the time domain and uses forward recursive filtering only, which makes it potentially fast and suitable for on-line realtime applications.

6.3 An example

The German Experimental Seismic System (GERESS) array project is a cooperative research program, jointly undertaken by Southern Methodist University in Dallas, Texas and Ruhr-University Bochum, Germany [Harjes, 1990]. The GERESS array is located in the Bavarian Forest area in the southeastern part of Germany near the border with Austria and Czechoslovakia. The array consists of 25 stations with vertical component short period (1 Hz) Teledyne Geotech GS-13 type instruments sampled at 40 Hz. In addition, four of the sites include horizontal component instruments. At the key station of the array, GEC2 ($\lambda = 48.84511$ N, $\varphi = 13.70156$ E) there is a supplemental three-component set of GS-13's sampled at 120 Hz (high-frequency element) and a three-component set of broad-band seismometers (Teledyne Geotech BB-13) sampled at 10 Hz.

The broad band and high frequency recordings of an event from Romania were selected for this demonstration (see Figure 6-1.) This event displays a considerable signal to noise ratio over much of the frequency range considered (see Figure 6-2.) It is a "broad band event", which could not be recorded exhaustively with only one of the two instruments involved.

6.3.1 Restitution of true ground movement

Analog transfer characteristics for the two seismometer systems GS-13 and BB-13 are specified by the manufacturer stating poles, zeroes and gain factor of the transfer function in the Laplace-domain (see table 6-1.)

Figure 6-1: Original seismograms recorded at GERESS reference station GSC2, of a broad band event from Romania of July 12, 1991, NEIS PDE: $t = 10:42:21.3$, $\varphi = 45.357$ N, $\lambda = 21.052$ E, $m_b = 5.0$, Δ from GERESS 670 km.

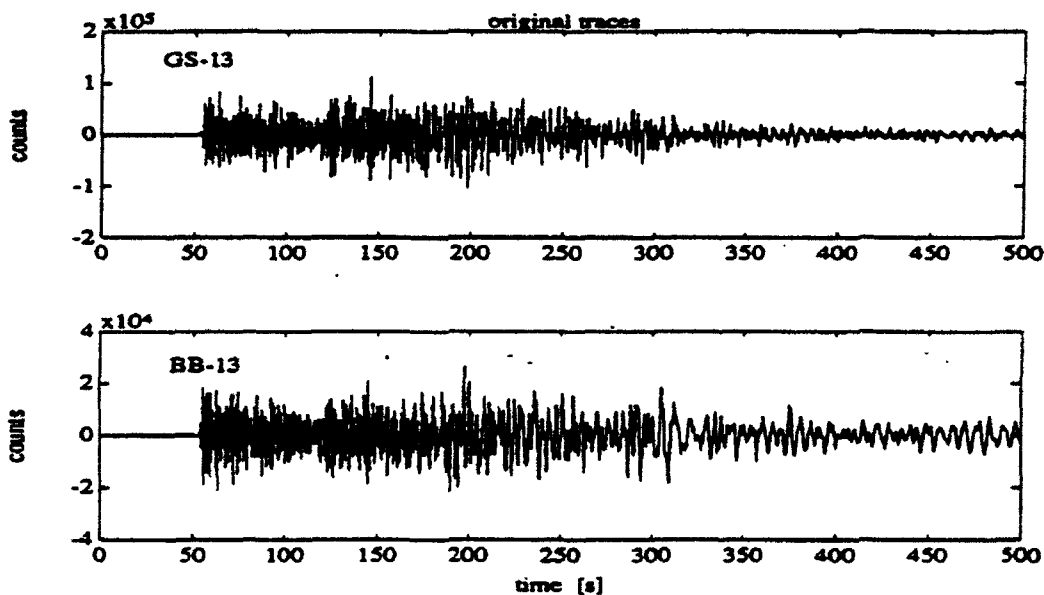


Figure 6-2: Smoothed power spectrum of the event from Romania (solid line) and of noise immediately preceding the event (broken line). Length of time window 660 s.

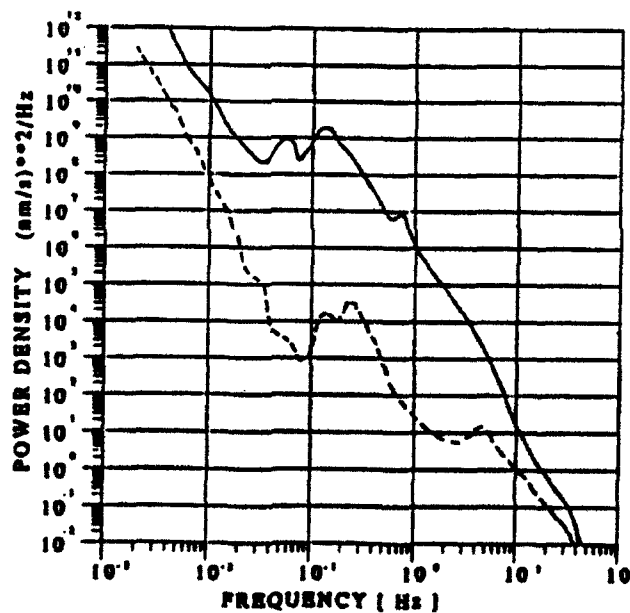


Figure 6-3: Amplitude (top) and phase (bottom) characteristics of the Seismometers GS-13 and BB-13, as specified by the manufacturer (solid lines) and approximated by poles and zeros below the Nyquist frequency (broken lines)

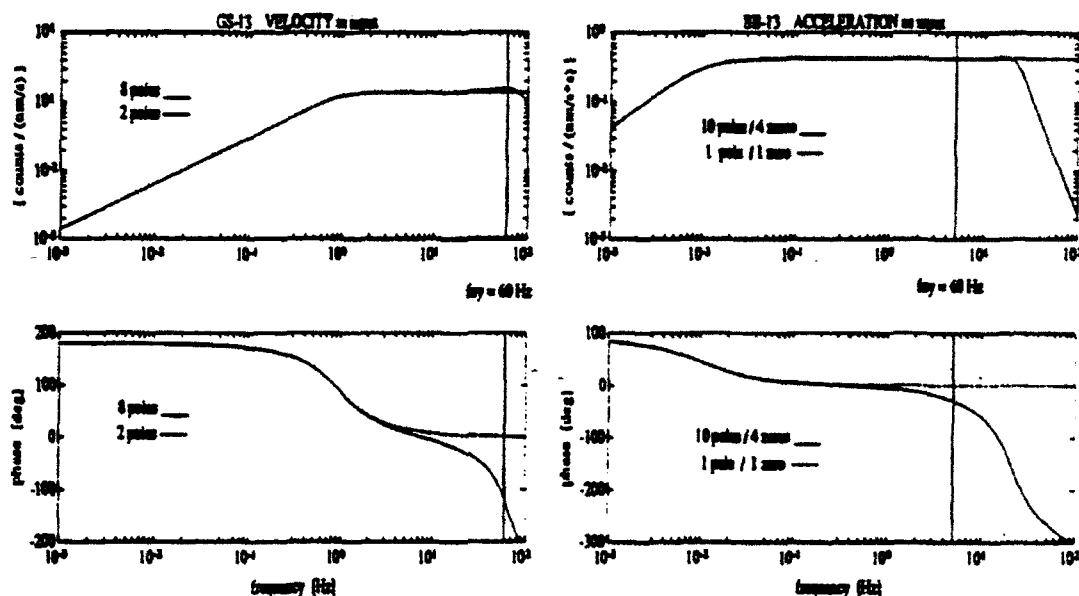
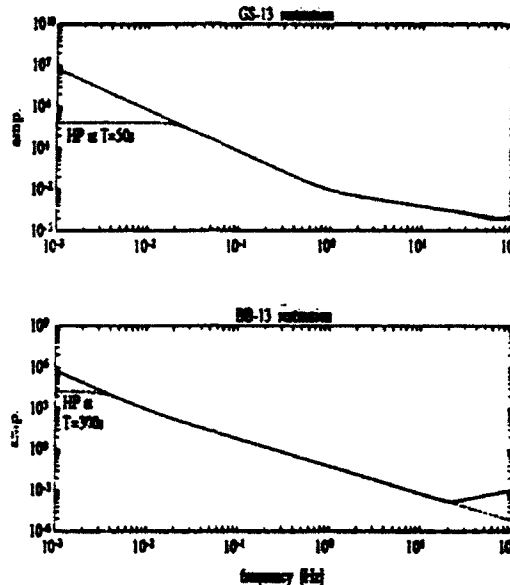


Table 6-1: Gain. Poles and zeroes of GERESS seismometer transfer functions. (For GS-13: assuming earth velocity as input. for BB-13: assuming earth acceleration as input. Poles and zeroes below the Nyquist frequency are printed in bold. If these are to be used as an approximation, the gain must be adjusted as indicated in brackets.)

Seism.type	gain g_s	zeros $s^{(0)}_k$	poles $s^{(1)}_l$
GS-13	1.5818E28 (2.6595E+01)	0 0	-4.3845E+00 + i 4.1812E+00
			-4.3845E+00 - i 4.1812E+00
BB-13	1.9991E+23 (4.2797E-01)	-6.1191E-05 -3.2015E+04 -1.2188E+03 -1.2793E+03	-1.2218E+02 + i 3.9408E+02
			-1.2218E+02 - i 3.9408E+02
			-6.0728E+02
			-1.3298E+03
			-2.5000E+07
			-1.7361E+08
			-4.5749e+01 + i 1.2322e+02
			-4.5749e+01 - i 1.2322e+02
BB-13	1.9991E+23 (4.2797E-01)	-6.1191E-05 -3.2015E+04 -1.2188E+03 -1.2793E+03	-3.0340e+03
			-1.2171e+03
			-6.0972e+02
			-6.2399e-02
			-1.0386e+02
			-1.3298e+03
			-2.5000e+07
			-1.7361e+08

Figure 6-4: Restitution operators are obtained by reversing seismometer transfer functions (solid lines.) They are simplified by omitting poles and zeroes which have effects above the respective Nyquist-frequencies only, and high pass filters at $T=50s$ and $T=300s$ are introduced to avoid instabilities. Amplitude characteristics of the resulting operators are given by the dotted broken lines.



Assuming ground velocity and ground acceleration as input for GS-13 and BB-13, respectively, this leads to the magnification and phase characteristics plotted in Figure 6-3 (solid lines.) For our purpose, only the intervals between dc cutoff filter (at $3.333 \cdot 10^{-3}$ Hz) and Nyquist frequency (at 5 Hz and 60 Hz respectively) are relevant, thus the transfer functions can be simplified by omitting all poles and zeros corresponding to frequencies above the Nyquist frequency, retaining only those printed in bold in table 6-1 and adjusting the gain factor accordingly. This manipulation produces only small consequences below the Nyquist frequency (broken lines in Figure 6-3.)

Direct inversion of the transfer function making zeros to poles and vice versa and taking the inverse of the gain, results in an operator capable of exactly reversing the influence of the systems on a signal (Figure 6-4, solid lines.) But as the inversion involves integration in the case of both systems (symbolized by poles at $s = 0$) these operators would become unstable in the presence of even the smallest dc offset. This instability must be removed by introducing two Butterworth high-pass filters at $T = 300$ s (BB-13) and $T = 50$ s (GS-13), which cancel the poles at zero (dashed lines in Figure 6-4.) The complete restitution operators in the Laplace-domain are listed in table 6-2.

For digital application these operators are transformed onto the z-domain and applied as forward recursive filters, using sine tapers to avoid

Table 6-2: Operators to reconstitute true ground displacement from GERESS high frequency channels (GS-13 sampled at 120 Hz) and broad band channels (BB-13 sampled at 10 Hz.) Operators are given in gain/zero/pole form both in the s -domain (see eq. 1) and the z -domain (eq. 13), as well as in polynomial form (eq. 14) in the appendices

Operator	gain g_s	zeros $s^{(k)}$	poles $s^{(m)}$
HFINVhp50	3.7720E-02	-4.3845E+00 +i 4.1812E+00 -4.3845E+00 -i 4.1812E+00	-1.2566E-01 -6.2832E-02 +i 1.0883E-01 -6.2832E-02 -i 1.0883E-01
	gain g_z	zeros $z^{(k)}$	poles $z^{(m)}$
	1.6284E-04	+9.6354E-01 +i 3.3602E-02 +9.6354E-01 -i 3.3602E-02 -1.0000E+00	+9.9895E-01 +9.9948E-01 +i 9.0642E-04 +9.9948E-01 -i 9.0642E-04
		numerator coefficients a_k	denominator coefficients b_l
		+1.000000000000000E+00 -9.270707123784236E-01 -9.975412649867432E-01 +9.295294473916804E-01	+1.000000000000000E+00 -2.997905604993305E+00 +2.995813402657642E+00 -9.979077965171582E-01
BBINVhp300	gain g_s	zeros $s^{(k)}$	poles $s^{(m)}$
	2.3366E-09	0 -6.2399E-02	-6.1191E-05 -2.0944E-02 -1.0472E-02 +i 1.8138E-02 -1.0472E-02 -i 1.8138E-02
	gain g_z	zeros $z^{(k)}$	poles $z^{(m)}$
	5.8474E-12	+9.937795E-01 +1.000000E+00 -1.000000E+00 -1.000000E+00	+9.999939E-01 +9.979078E-01 +9.989517E-01 +i 1.811901E-03 +9.989517E-01 -i 1.811901E-03
		numerator coefficients a_k	denominator coefficients b_l
		+1.000000000000000E+00 +6.220506692349304E-03 -1.993779493307651E+00 -6.220506692349415E-03 +9.937794933076506E-01	+1.000000000000000E+00 -3.995805091448180E+00 +5.987424068361191E+00 -3.987432853156351E+00 +9.958138762433976E-01

transient effects. A procedure to effect the necessary transform is given in the Appendix I, the restitution operators in pole/zero form in the z-domain and as recursive filter coefficients are listed in table 6-2.

6.3.2 Adjustment of sample frequencies

Before the two traces from restituted GS-13 and BB-13 registrations can be added, sample frequencies must be equalized, interpolating 11 values between every 2 values in the 10 Hz BB-13 trace. The nature of the interpolation algorithm employed is not critical, since frequencies falsely introduced by rough interpolation will be cut off later, anyhow. Both an elaborate and a simple triangular algorithm were tested and found to perform equally well.

6.3.3 Compensation of time shifts

At this stage a possible time lag between the two traces can be found by calculating the cross-covariance function. In the case of GEC2, the lag which is already clearly visible on the raw recordings, was found to be 18 samples (corresponding to 0.15 s.) The lag was compensated for by shifting the leading BB-13 trace with respect to the trailing GS-13 trace.

6.3.4 Tailoring of individual passbands

If the traces were added at this stage, the middle frequency range - where both seismometers perform well - would be overrated as compared to the low frequency end below 0.02 Hz (where the GS-13 trace was not properly restituted) and the high frequency end above 5 Hz (where the BB-13 trace was merely interpolated.) The solution is to perform a weighted summation by first applying a high-pass filter to the GS-13 restituted trace and a low-pass filter to the BB-13 restituted trace. These "tailoring filters" are depicted in Figure 6-5. Care is required in their design (see Appendix II), because they determine the transfer characteristics of the synthesized BB trace (solid line in Figure 6-5.) The small imperfection in the amplitude characteristic at 0.2 Hz is unavoidable, when filtering is limited to forward recursion. The tailored traces are shown in Figure 6-6.

6.3.5 Addition and numerical differentiation

Now the weighted traces can be added point-wise, resulting in the desired BB seismogram. It is a record of true ground displacement between $3.333 \cdot 10^{-3}$ Hz and 48 Hz (anti-alias filter cut-off.)

To obtain a velocity-proportional or acceleration-proportional seismogram, the BB trace may be numerically differentiated once or twice (Figure 6-7.)

Figure 6-5: Amplitude (top) and phase (bottom) characteristics imposed on the synthesized BB trace by tailoring filters (solid line.) The broken and dotted lines represent the contributions of HP and LP filters used. Imperfections at the middle frequency are unavoidable, they are shown in linear scale in fig 0-11.

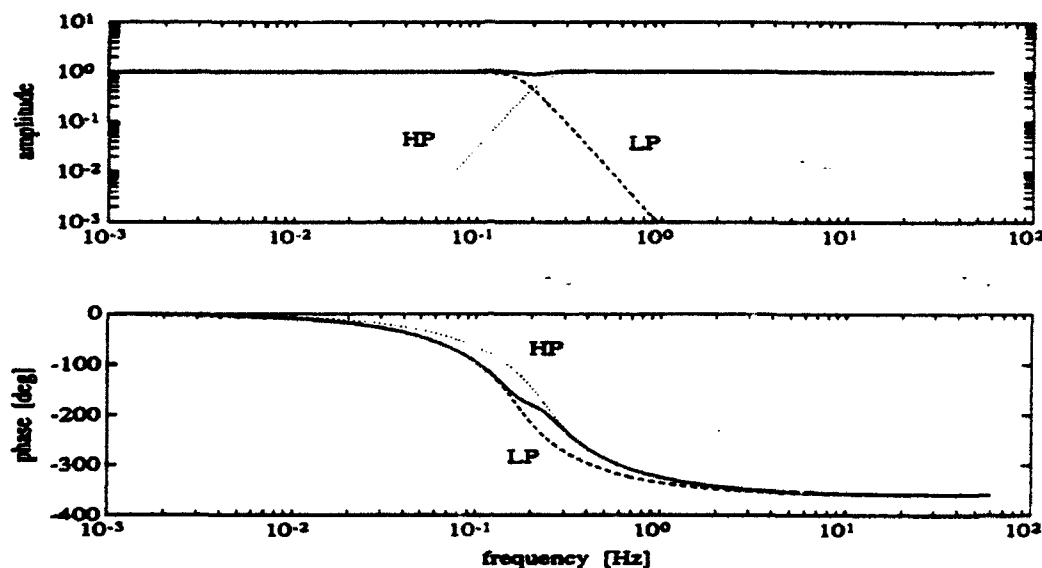


Figure 6-6: Restituted seismograms (interpolated in case of BB-13), run through the "tailoring filters", prior to summation.

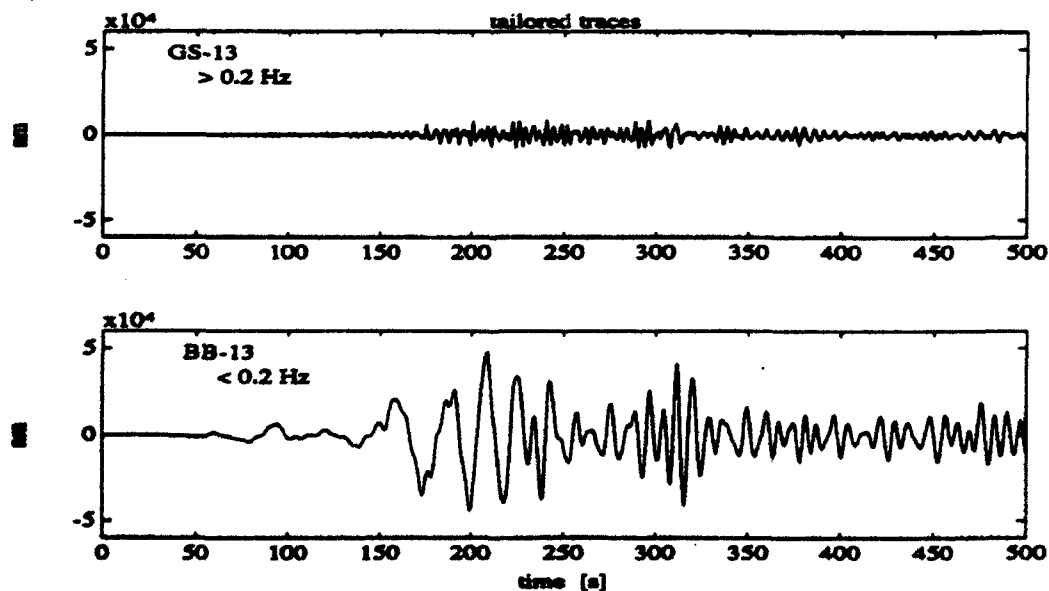


Figure 6-7: Synthesized BB trace. From top to bottom: (a) whole seismo-gram (b) first onset displacement (c) velocity (d) acceleration

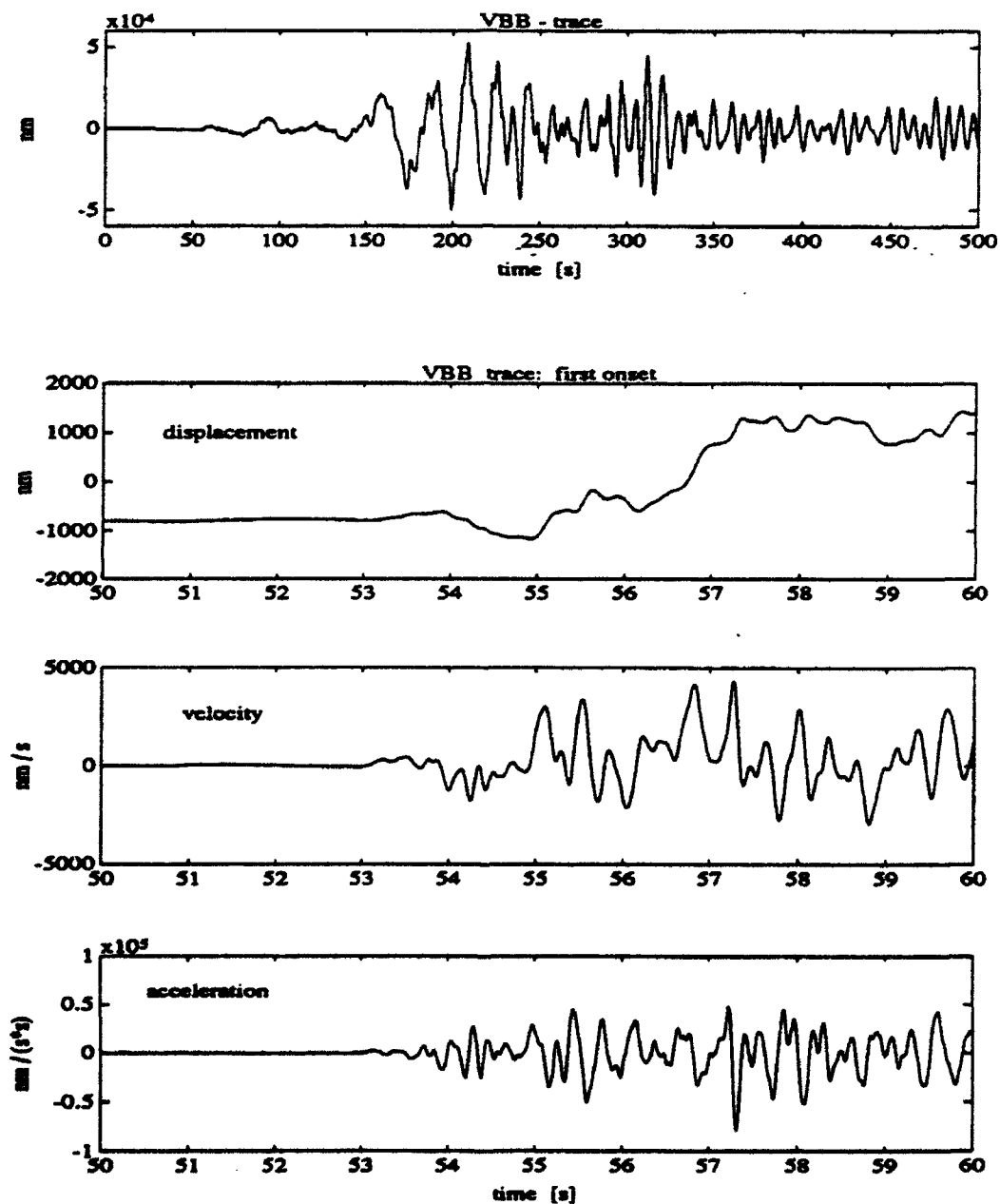
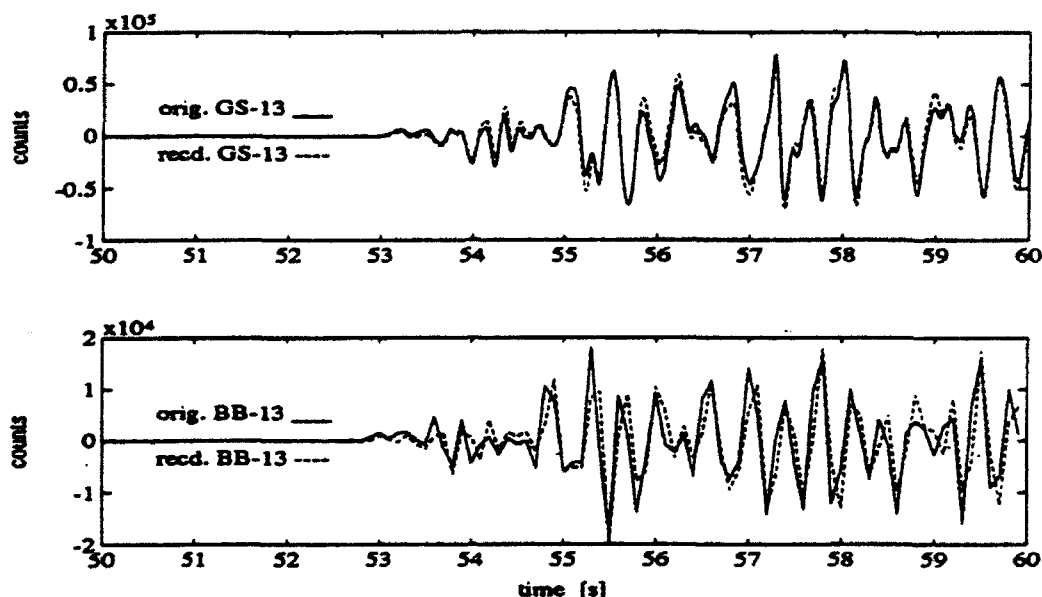


Figure 6-8: Comparison of originally measured traces (solid lines) and traces recovered from BB synthesis (broken lines) for verification purposes.



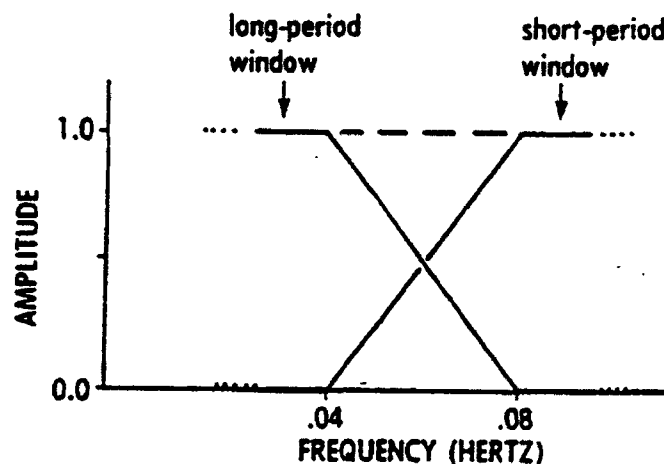
6.4 Verification

For the purpose of verification of the method, the GS-13 original trace can be recovered by treating the BB trace as input and simulating GS-13 system response through application of the transfer function according to Appendix I. Figure 6-8 (top) shows that a reasonable match is achieved between the measured and the simulated GS-13 trace. The small differences visible in the zoomed first few seconds can be ascribed to the phase bias introduced by the stabilizing high-pass filter at $T = 50$ s in the restitution phase.

The same should theoretically be possible for the BB-13 original trace, but here the anti-alias filter (3 dB point at 4.5 Hz) of the digital recording system must be modelled carefully and the number of data points decimated by a factor of 12. This introduces a certain amount of arbitrariness (at which point to start decimation) and the coincidence is not as good (see Figure 6-8, bottom.) The match could be improved, however, by low-pass filtering both the original and the recovered trace.

One can therefore be reasonably sure that after application of the above procedure one has a faithful BB record of true ground movement, which can be used in further studies requiring broad band data (e.g. moment tensor inversion), or can be filtered to match the system response of seismograph systems serving as international reference.

Figure 6-9: Tailoring filters which were applied in the frequency domain by Harvey & Choy [1982]. While adding up to unity in the frequency domain (dashed lines), their discontinuous derivatives should produce $\text{sinc}^2(t)$ -ripples.



6.5 Discussion

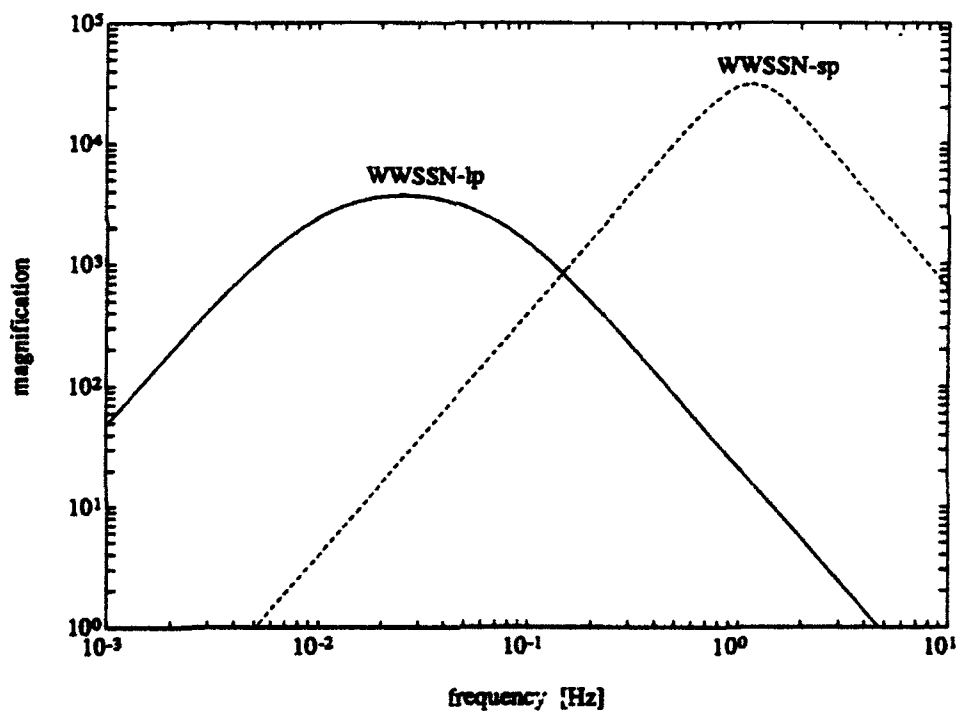
Problems may arise, if the signal to noise ratio drops below unity in the low frequency range. In this case the long period noise would be amplified in the BB trace, completely overwhelming the short period signal. Rather than redesigning the restitution filters with an increased high-pass cut-off point it is recommended to prefilter the original traces with a high-pass filter before the application of the BB synthesis. Alternatively the BB trace could be high-pass filtered.

The small phase bias introduced by the restitution filters could be avoided, if two-sided recursive algorithms (described by Marschall [1984]) were used for the implementation of all filters. This would, however, preclude the on-line real-time application of the synthesis.

The same applies for synthesis in the frequency domain, following Harvey & Choy [1982]. Moreover, the overlapping frequency filters employed by these authors (see Figure 6-9.) have discontinuous derivatives, which should produce $\text{sinc}^2(t)$ -ripples in the time domain.

The described method can also be applied to narrow band seismograph systems like WWSSN-lp and WWSSN-sp, as long as the resolution of the analog/digital converter is sufficiently high to raise the magnification to unity in the overlapping region while preserving an acceptable signal/noise ratio. As can be seen on Figure 6-10 an A/D-converter with 24 bit resolution, as used at GERESS, would suffice in this case.

Figure 6-10: Amplitude curves of WWSSN-lp (solid line) and WWSSN-sp (broken line) system response to ground velocity. [Static gain factors were adjusted to 1,000 and 200,000 for lp and sp respectively] In order to synthesize a BB [$10^{-3} \dots 20\text{Hz}$] trace, the signal level must be raised by up to 2.5 decades. In case of a 24-bit A/D-converter as used at GERESS, this would leave at least 95 dB resolution over the whole frequency range.



APPENDIX I

Let $H(s)$ be a stable transfer operator in the s -domain, $s = i\omega$ being the variable of the Laplace transform. It is usually given in (or can be cast into) pole/zero/gain form

$$H(s) = g_s \cdot \frac{A(s)}{B(s)} = g_s \cdot \frac{\prod_{k=0}^M (s - s^{(0)}_k)}{\prod_{l=0}^N (s - s^{(\infty)}_l)}, \quad (1)$$

with gain g_s , zeroes $s^{(0)}_k$ and poles $s^{(\infty)}_l$.

In order to be applicable to time sampled data, it must first be approximated in the z -domain, $z = e^{-sT}$ being the variable of the \mathcal{Z} -transform with sampling interval T . Several transformations were tried (pulse-invariant, step-invariant and ramp-invariant, see [Schüßler, 1964] for a review) but the well-known bilinear z -transformation [Golden, 1964]

$$s = \frac{2}{T} \cdot \frac{z - 1}{z + 1} \quad (2)$$

together with frequency prewarping

$$\tilde{\omega} = \frac{2}{T} \cdot \tan\left(\frac{T}{2} \cdot \omega\right) \quad (3)$$

was found to perform best.

Single poles and zeros are simply prewarped according to

$$\tilde{s}^{(0/\infty)} = \frac{2}{T} \cdot \tan\left(\frac{T}{2} \cdot s^{(0/\infty)}\right). \quad (4)$$

Complex conjugate poles and zeros can be imagined to arise as solutions of quadratic equations of the form

$$s^2 + 2h\omega_0 s + \omega_0^2 = 0 \quad (5)$$

which describe damped harmonic oscillation in the s -domain with free circular frequency ω_0 and damping constant $h < 1$. Their solutions are

$$s_{1/2} = -\omega_0 \cdot [h \pm i(1 - h^2)^{1/2}] \quad (6)$$

Introducing

$$\begin{aligned} x &:= \Re(s_1) = -\omega_0 h \\ y &:= \Im(s_1) = -\omega_0 \sqrt{1 - h^2} \end{aligned}$$

and solving for ω_0 and h we get

$$\omega_0 = \sqrt{x^2 + y^2} = |s_1| \quad \text{and} \quad (7)$$

$$h = \frac{x}{\omega_0} = \frac{|\Re(s_1)|}{\omega_0} \quad (8)$$

h is left unchanged, while ω_0 is prewarped to $\tilde{\omega}_0$ according to (3), such that the prewarped conjugate pair is

$$\tilde{s}^{(0/\infty)}_{1/2} = -\tilde{\omega}_0 \left[h \mp i(1 - h^2)^{1/2} \right] \quad (9)$$

In all the bracketed expressions in eq. 1, the $s^{(0/\infty)}$ is replaced by $\tilde{s}^{(0/\infty)}$ from eq. 4 or eq. 9, while s is replaced by $\frac{2}{T} \cdot \frac{z-1}{z+1}$ from eq. 2. Thus each

$$(s - s^{(0/\infty)}_i) \longrightarrow \left(\frac{2}{T} \cdot \frac{z-1}{z+1} - \tilde{s}^{(0/\infty)}_i \right)$$

and by rearranging

$$= \frac{\frac{2}{T} - \tilde{s}^{(0/\infty)}_i}{z - 1} \cdot \left(z - \frac{2 + \tilde{s}^{(0/\infty)}_i \cdot T}{2 - \tilde{s}^{(0/\infty)}_i \cdot T} \right) \quad (10)$$

Identifying

$$\frac{2 + \tilde{s}^{(0/\infty)}_i \cdot T}{2 - \tilde{s}^{(0/\infty)}_i \cdot T} := z^{(0/\infty)}_i \quad \text{and} \quad (11)$$

$$g_s \cdot \frac{\prod_{k=1}^M \left(\frac{2}{T} - \tilde{s}^{(0)}_k \right)}{\prod_{l=1}^N \left(\frac{2}{T} - \tilde{s}^{(\infty)}_l \right)} := g_z \quad (12)$$

we get

$$H(z) = H(s) \begin{matrix} s^{(0/\infty)} \longrightarrow \tilde{s}^{(0/\infty)} \\ s \longrightarrow \frac{2}{T} \cdot \frac{z-1}{z+1} \end{matrix} = g_z \cdot (z+1)^{N-M} \cdot \frac{\prod_{k=1}^M (z - z^{(0)}_k)}{\prod_{l=1}^N (z - z^{(\infty)}_l)} \quad (13)$$

the desired operator in the z -domain.

For each pole and zero in the s -domain a corresponding pole or zero in the z -domain can be computed according to eq. 11 and the gain is adjusted according to eq. 12. For every excessive pole ($N > M$) in the s -domain, one zero at $z = -1$ is added in the z -domain. In case of excessive zeros, $(z+1)^{N-M}$ would produce one or more poles on the unit circle, thereby destabilizing the filter. This shows, that the transform is *not* suitable in case of excessive zeroes. Another condition derived from eq. 3 is that *no* characteristic frequency associated with a pole or zero via eq. 7 may be higher than the Nyquist frequency $\frac{1}{2T}$ because of the periodicity of the tangent function.

Even though these conditions are met, the accuracy to which $H(z)$ approximates $H(s)$ varies, being usually poor close to the Nyquist frequency. It can be checked by evaluating $H(z)$ along the unit circle and comparing it to $H(s)$ evaluated along the imaginary axis.

Once eq. 13 has been obtained, it can be brought into polynomial form

$$H(z) = g_z \cdot \frac{\sum_{k=0}^N a_k z^{-k}}{\sum_{l=0}^N b_l z^{-k}} \quad (14)$$

by multiplication and is implemented as a forward recursive filter following [Seidl, 1980, eqs. 10 through 16] or [Ferber, 1989, eqs. 26 and 48 through 51]

APPENDIX II

Overlapping low pass and high pass Butterworth filters were employed as tailoring filters because of their smoothness both in the time and frequency domain. Their amplitude characteristics $M_{LP}(\omega)$ and $M_{HP}(\omega)$ are given [Kulhánek, 1967, pp 87ff] by

$$\begin{aligned} M_{LP}^2(\omega) &= \frac{\omega_L^{2n}}{\omega_L^{2n} + (-1)^n \omega^{2n}} \\ M_{HP}^2(\omega) &= \frac{(-1)^n \omega^{2n}}{\omega_H^{2n} + (-1)^n \omega^{2n}} \end{aligned} \quad (15)$$

They are solely determined by orders n and corner frequencies ω_L and ω_H , which shall be spaced equally (on a logarithmic frequency scale) around a middle frequency ω_M :

$$\begin{aligned} \omega_L &= \omega_M / a \\ \omega_H &= \omega_M \cdot a. \end{aligned} \quad (16)$$

The condition that,

$$M_L(\omega = \omega_M) + M_H(\omega = \omega_M) \stackrel{!}{=} 1$$

and, because of symmetry,

$$\Rightarrow M_L(\omega_M) = M_H(\omega_M) = 0.5 := \alpha$$

leads to the expression for a

$$a = \sqrt[2n]{\frac{1}{\alpha^2} - 1} \quad (17)$$

With ω_M set to $2\pi \cdot 0.2 \text{ Hz}$ and the order $n = 4$ chosen for coincidence of phase characteristics of both LP and HP, corner frequencies can be calculated according to eq. 16. Unfortunately, the resulting amplitude characteristics

Figure 0-11: Close-up of the crossover point of tailoring filters in linear scale. Ideally the sum of the filter amplitudes should be unity everywhere. The condition in eq. 17 yields unity at 0.2 Hz (left), while the condition in eq. 18 results in an amplification which preserves overall gain (right.)

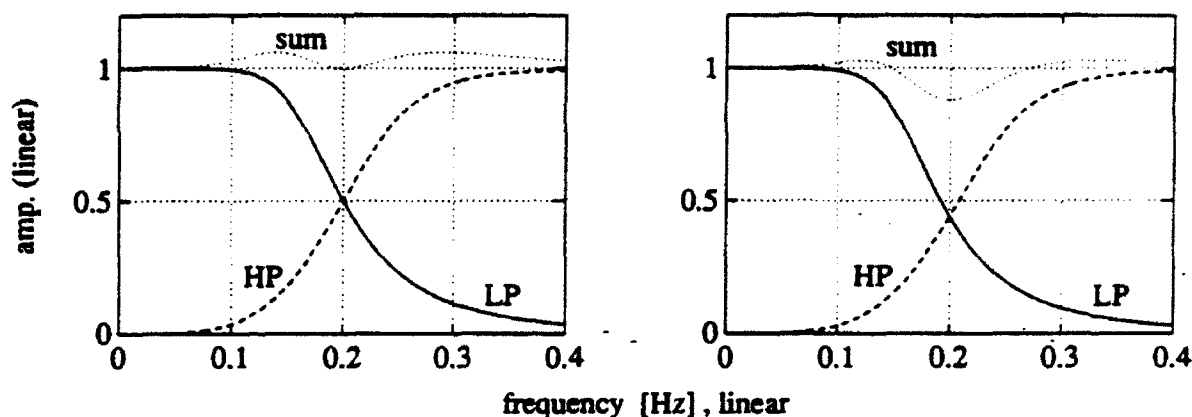


(Figure 0-11, left) do not add up to unity along the whole frequency axis. If overall gain is to be preserved, the expression

$$\int_0^{\infty} [M_{LP}(\omega, a) + (M_{HP}(\omega, a) - 1)] d\omega \stackrel{!}{=} 0, \quad (18)$$

evaluated by numerical integration and a zero-finding algorithm, leads to the determination of an optimum value of a ($n = 4$, $\omega_L = 2\pi \cdot 0.2 \text{ Hz}$) = 1.19504. The corresponding amplitude characteristic is also plotted in Figure 0-11 (right.) In the example considered, the resulting differences in the BB trace were below 3%.

Poles and zeros of the filters were calculated following [Kulhánek, 1967, eqs. 3.16 and 3.17]. Transfer to the z -domain and implementation as forward recursive filters were done as described in Appendix I.

I thank Prof. Harjes, who suggested the topic, and my colleagues for providing a creative working environment.

References

- [Ferber, 1989] Ferber, R.-G.: Recursive deconvolution filters for seismograph systems. *Bull.seism.Soc.Am.* 79, 1629-1641, 1989.

- [Golden, 1964] Golden, R. M. & Kaiser, J. F.: Design of wideband sampled-data filters. *The Bell System Technical J.* July 1964, 1533-1546.
- [Harjes, 1981] Harjes, H.-P.: Broad-band seismometry - a unified approach towards a kinematic and dynamic interpretation of seismograms, in *Identification of Seismic Sources - Earthquake or Underground Explosion*, pp. 763-786, ed. Husebye, E. S. & Mykkeltveit, S., Reidel, Dordrecht.
- [Harjes, 1990] Harjes, H.P.: Design and siting of a new regional array in Central Europe, *Bull. Seism. Soc. Am.* 80, 1801-1817.
- [Harvey & Choy, 1982] Harvey, D. & Choy, G. L.: Broad-band deconvolution of GSDN data. *Geophys.J.R.astr.Soc.* 69, 659-668, 1982.
- [Kulhánek, 1967] Kulhánek, O.: *Introduction to Digital Filtering in Geophysics*. Amsterdam, Elsevier 1967.
- [Marschall, 1984] Marschall, R.: Ein- und zweidimensionale Rekursiv-Filter und ihre Anwendung in der Seismik. *Habilitationsschrift Ruhr-Universität Bochum*, 1984.
- [Schüßler, 1964] Schüßler, H.-W.: A signalprocessing approach to simulation. *Frequenz* 35 No. 7, 174-184, 1964.
- [Seidl, 1980] Seidl, D.: The simulation problem for broad-band seismograms. *J.Geophys.* 48, 84-93, 1980.

7. QUANTIFICATION OF TIME - INDEPENDENT SPECTRAL STRUCTURES IN SONOGRAMS

Jan Wüster

7.1 Introduction

Near regional seismograms of conventional industrial explosions (i.e. mine and quarry blasts) show a peculiarity termed "spectral scalloping" or "time-independent spectral structures", which is absent from earthquake seismograms. It consists of local spectral peaks and troughs that can be traced along the whole duration of the seismogram. Sonogram analysis and subsequent smoothing and 1-bit-compression bring out these structures as horizontal bands (Hedlin et al., 1989). The phenomenon is observed, whenever industrial explosions are studied using high frequencies, it is generally explained with the multiple nature of commercial blasts, the so-called ripple-firing technique (peaks) (e.g. Smith, 1989) and by the finite size and duration of the source (troughs) (e.g. Chapman et al., 1992.)

The presence of spectral structures has been used as a discriminant between earthquakes and chemical explosions in discrimination studies in Scandinavia using NORESS data (Baumgard & Ziegler, 1988, Dysart & Pulli, 1990) and also in the Vogtland area in Central Europe using GERESS data (Wüster, 1993.) In Figures 7-1 and 7-2 two typical examples from the earthquake and explosion populations of the latter study are compared. Both earthquakes and explosions display spectral complexity in the sonograms. However, only in the case of the blasts can the local peaks be traced along the whole signal portion of the sonogram between the P-onset at $t=10$ sec and the coda at approximately $t=60$ sec, as revealed by the 1-bit-compressed digital matrices.

7.2 Why quantify?

The presence or absence of time-spanning spectral structures is easily noted in Figures 7-1 and 7-2, but in some cases, particularly with poor signal/noise ratio, the distinction is not as clear-cut. Also, in a concept in which several discriminants are combined to produce a final verdict, quantitative values must be attached to each discriminant. Moreover, if the origin of the spectral structures is attributed to ripple-firing, characteristic 'wavelengths' in the frequency domain are indicative of the delay between successive explosions

Figure 7-1: Seismogram, sonogram and 1-bit-compressed digital matrix of a typical Vogtland earthquake

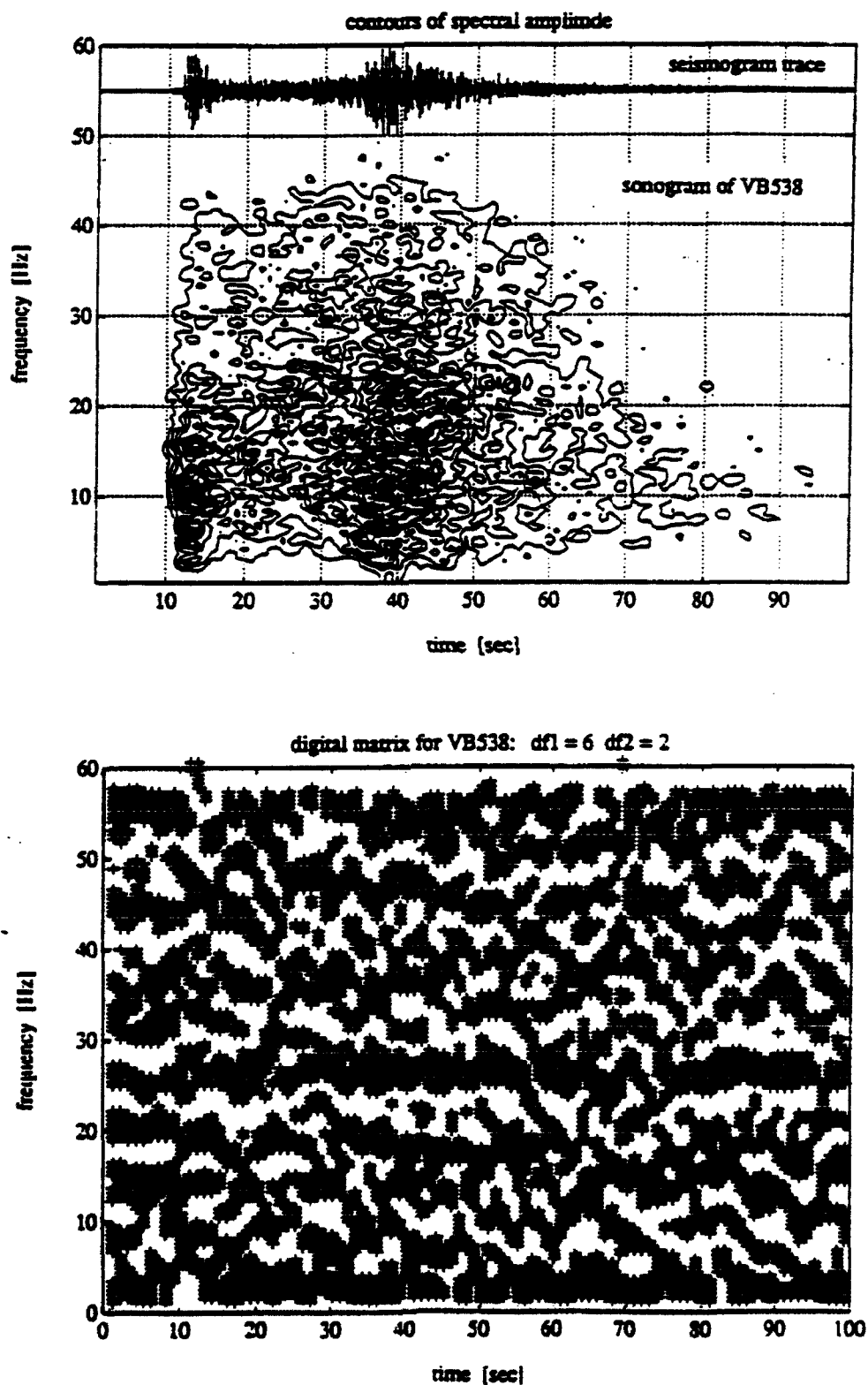
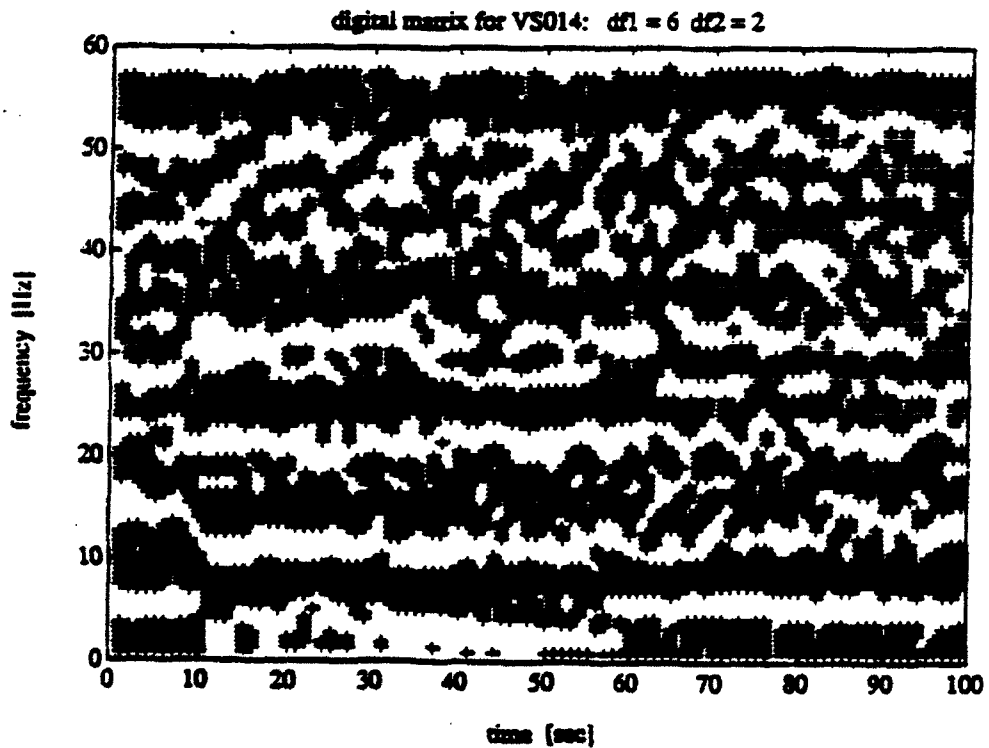
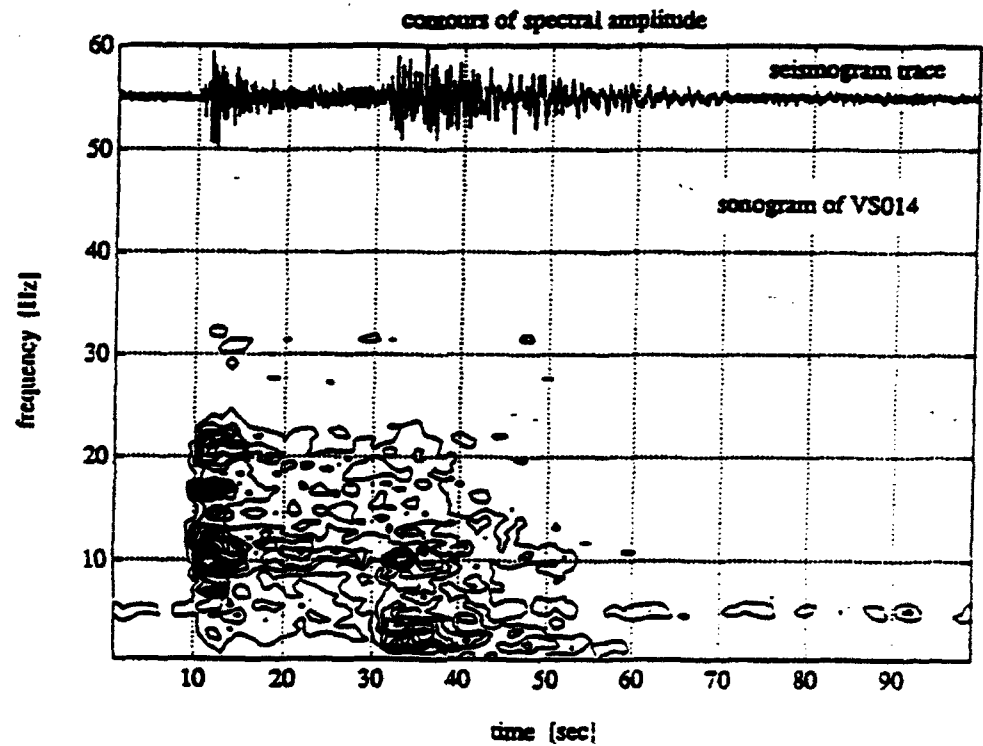


Figure 7-2: Seismogram, sonogram and 1-bit-compressed digital matrix of a typical Vogtland explosion



and may aid in the identification of specific quarries or mines. Therefore a quantitative evaluation of the spectral structures is desirable. To this end the following techniques were applied:

- cepstral analysis
- harmonic product spectrum
- horizontal sums.

7.3 Cepstral analysis

Let $f(t)$ be a time series and $|F(\omega)|$ a crude estimation of its amplitude-spectrum derived from the Fourier transform $\mathcal{F}\{f(t)\} = F(\omega)$, then the real cepstrum $\bar{f}(\bar{t})$ is defined according to Båth (1974) as the amplitude-spectrum of the real logarithm of $|F(\omega)|$:

$$\bar{f}(\bar{t}) = \left| \int_{-\infty}^{+\infty} \log(|F(\omega)|) e^{-i\bar{t}\omega} d\omega \right| \quad (1)$$

Its merit as opposed to a simple spectrum of the spectrum lies in the fact, that the logarithm separates the different factors, if the spectrum can be written as a product

$$F(\omega) = G(\omega) \cdot H(\omega) \quad (2)$$

This is regularly the case with multiple sources, as shown in the synthetic example of Figure 7-3. Five successive 2nd-order Küpper-pulses of 0.1 sec duration each are applied with delays of 0.2 sec (Fig. 7-3a.) The resulting spectrum $|F(\omega)|$ (Fig. 7-3b) is the spectrum of the single Küpper-pulse with its spectral maximum at 10 Hz ($|G(\omega)|$, Fig. 7-3c) multiplied by the spectrum of five successive spikes ($|H(\omega)|$, Fig. 7-3d.) The spectrum of the spectrum (Fig. 7-3e) is - according to the convolution theorem - the convolution $g(t) * h(t)$. The peak at 0.2 sec in Figure 7-3e is accompanied by two side maxima which would tend to broaden and obscure it in the presence of noise, neither could the second main frequency component at 0.1 sec be determined in an easy way. In the cepstrum (Fig. 7-3f), on the other hand, both spectral factors are clearly separated into distinct spectral peaks.

This property of the cepstrum is used for vocal pitch detection in acoustics (Noll, 1963) and a corresponding apparatus for use in telephony has even been patented (Schroeder, 1965.) The discrimination between single events and ripple-fired explosions in seismology poses an analogous problem to the discrimination between consonants and vowels in speech processing. In a voiced portion of speech, the vocal tract is excited by periodic puffs of air produced by the glottis, just as in a ripple-fired explosion the wave-path to the receiver is excited by periodic explosions. The analogy suggests that the

Figure 7-3: a,b,c,d

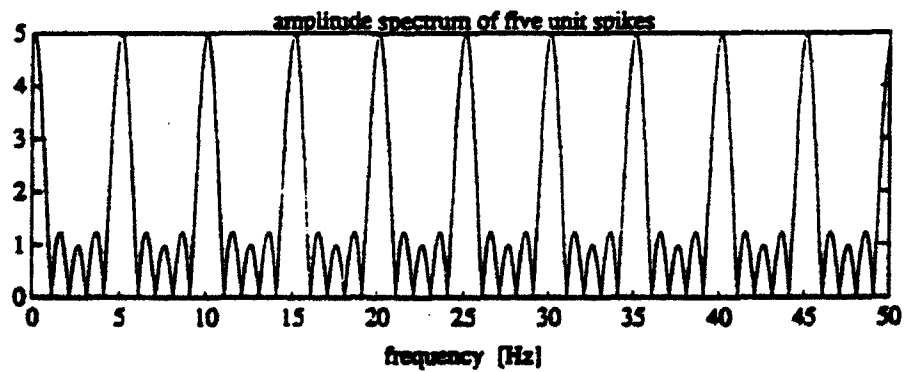
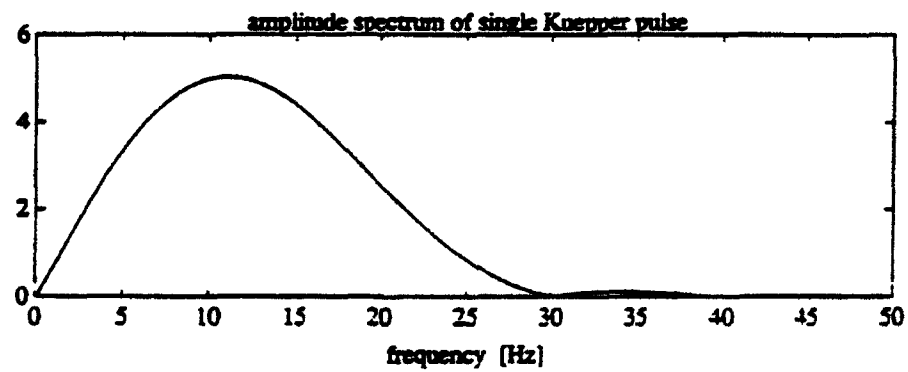
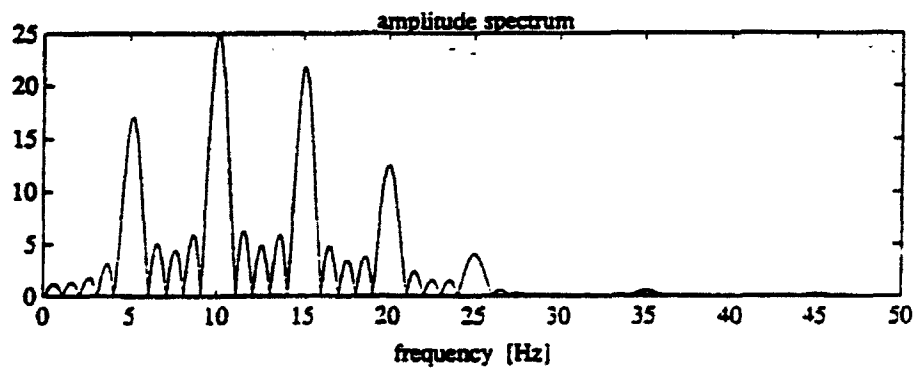
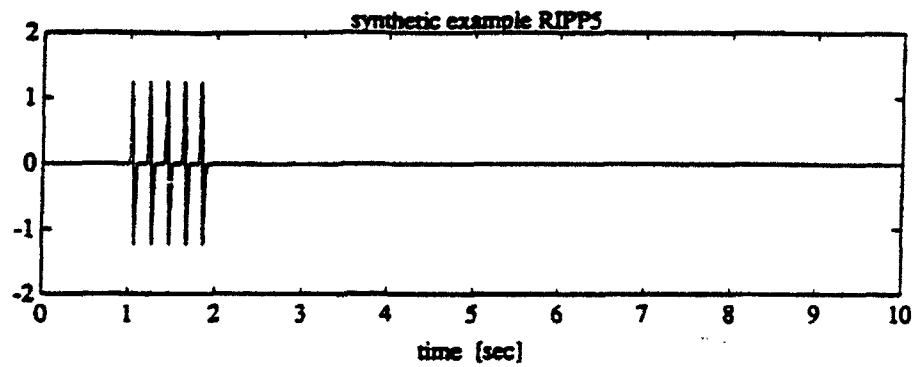
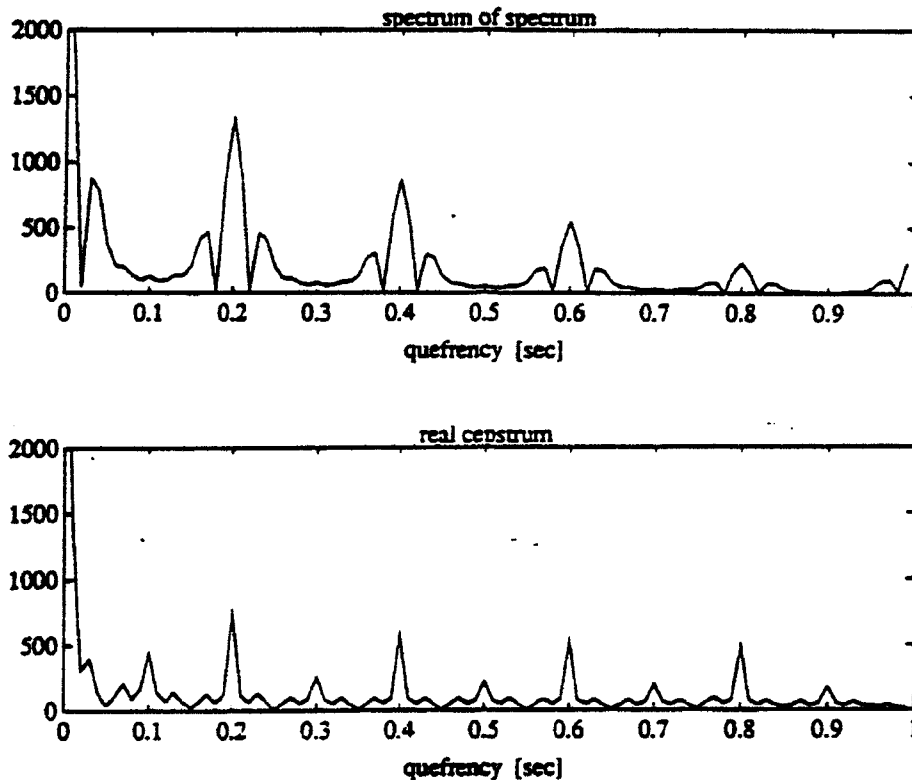


Figure 7-3: e,f



cepstrum should be well suited to extract the dominant quefrency (=wavelength in the frequency domain), thus quantifying the effect of the ripples.

Unfortunately, the logarithm is very susceptible to noise, which is much more a problem in seismology than in speech processing. This is shown in Figure 7-4 with the same synthetic example adding only 10% of normally distributed random noise. While the periodicity of the spectrum is still very clear, the corresponding cepstral peak is already quite feeble, and with 33% noise added it is no longer recognizable.

In cases of high signal/noise ratio, the cepstrum can indeed help to quantify frequency structures in sonograms, as is shown with a synthetic example in Figure 7-5. The time series RIPP120 is made to resemble the data traces used in the discrimination study. It is made up of Küpper pulses of 0.083 sec duration each, at 0.167 sec interval from $t = 10 \dots 45$ sec; 1% normally distributed random noise is superposed. Sonograms are calculated using exactly the same procedure as with actual data. In the 1-bit-compressed matrix (Fig. 7-5a) a clear banding structure results. The spectral period read from the matrix is 6 Hz. This corresponds to a quefrency of $1/6\text{Hz} = 0.16\bar{6} \dots$ sec brought out by the dominant cepstral peak in the wiggle trace plot of Figure 7-5b.

Turning now to real data, the cepstral wiggle trace plot for the event VS014 (Fig. 7-6a) does not allow a dominant quefrency to be picked, although the corresponding banding structure in Figure 7-1b is also very clear.

Figure 7-4: a,b,c,d: Synthetic example with noise

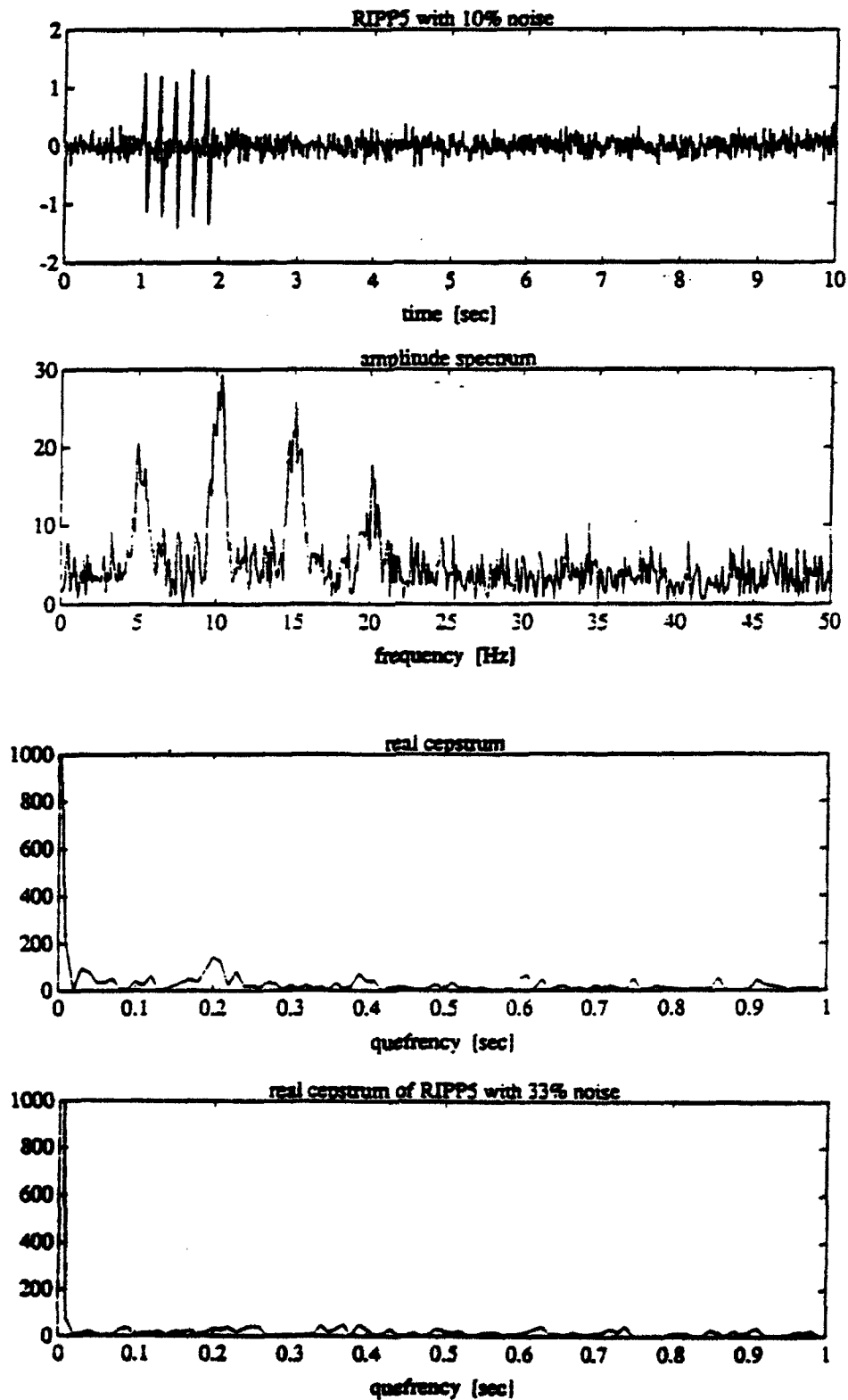
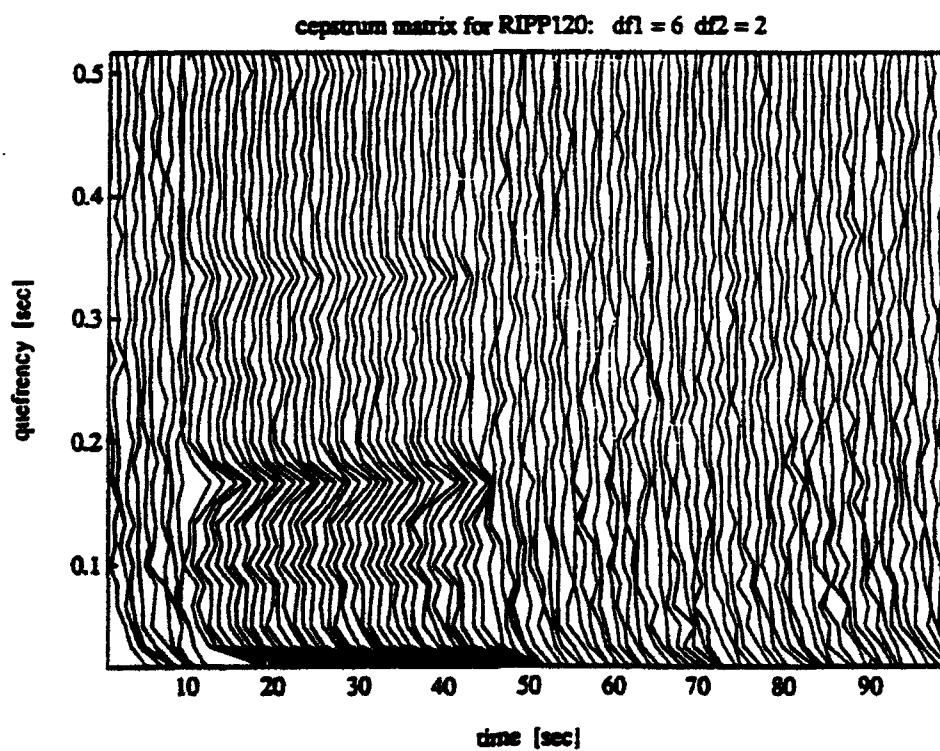
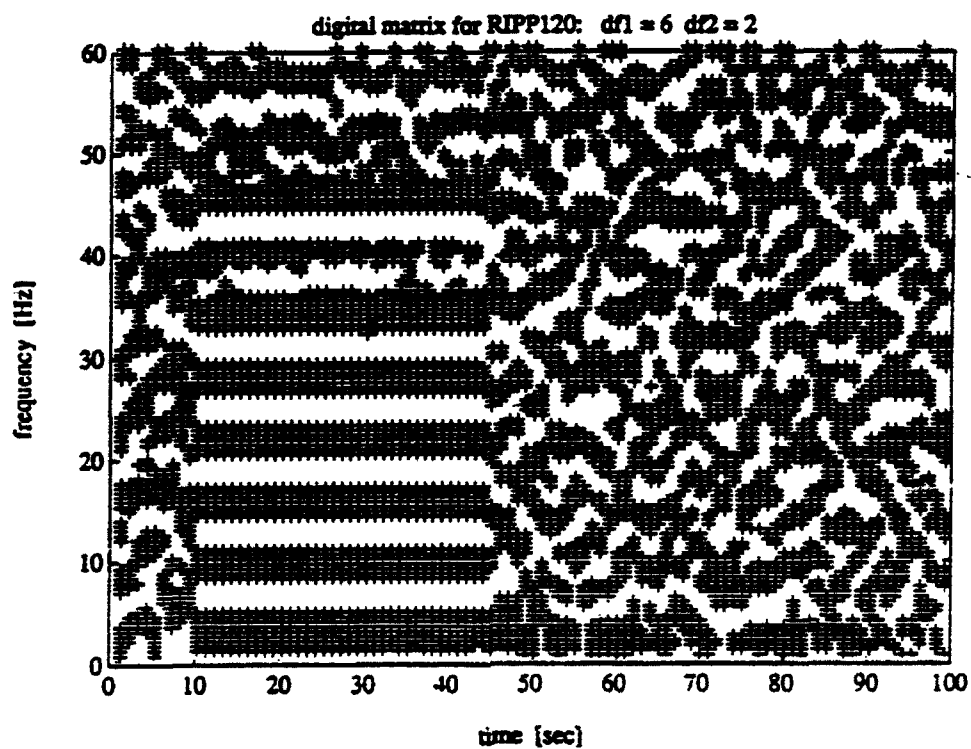


Figure 7-5: Synthetic data with 1% noise: a) 1-bit-compressed digital matrix, b) cepstrum matrix



Against these odds, Baumgard & Ziegler (1988) have successfully employed cepstral peaks for discrimination, using spectral stacks of all NORESS channels for smoothing and noise reduction. This is not an option here, if frequencies above 16 Hz are to be considered, because the normal GERESS channels are sampled at 40 Hz and anti-alias filtered at 16 Hz. Just the hf-element at array station GEC2 is sampled at 120 Hz (anti-alias filter at 48 Hz.)

7.4 Harmonic product spectrum

Another method for the measurement of the pitch or fundamental frequency of a signal is the harmonic product spectrum (HPS). It is defined by Schroeder (1986) as the function obtained by adding the logarithm of all spectral amplitudes, which are integer multiples of the fundamental frequency, i.e. the harmonic overtones:

$$\text{HPS}(\omega) = \sum_{n=1}^N \log |F(n\omega)| = \log \prod_{n=1}^N |F(n\omega)| \quad (3)$$

The HPS should give a clear peak at the fundamental frequency, even if this frequency and/or some of the overtones are missing, provided the overtones present are harmonic. The synthetic example in Figure 7-3 has already shown that periodic excitation results in harmonic overtones, and the fundamental frequency of 5 Hz is indeed extracted well by the HPS in Figure 7-7, even in the presence of noise.

Application of the HPS to the sonogram matrix for the synthetic example RIPP120 yields a clear peak at the fundamental frequency of 6 Hz (Fig. 7-7c). However, application of the method to real data does not yield a comparable peak (Fig. 7-6b)

7.5 Horizontal sums

At this point it was decided to start from the phenomenology: If spectral bands are observed, surely they can be quantitatively extracted. Other than in the applications of pattern recognition methods to the detection of seismic horizons (e.g. Lu & Cheng, 1990), we expect bands in the sonograms, corresponding to time-independent spectral peaks, to be strictly parallel and horizontal.

In order to extract such structures, horizontal sums are calculated across the 1-bit-compressed digital sonogram matrices, along the time axis. White spots (local spectral highs) are assigned a value of 1, black spots (local spectral lows) are assigned a value of 0. In order to avoid the misinterpretation of stationary spectral peaks of the noise as spectral bands of the

Figure 7-6: Cepstrum(a) and Harmonic Product Spectrum(b) matrices for a clear Vogtland explosion

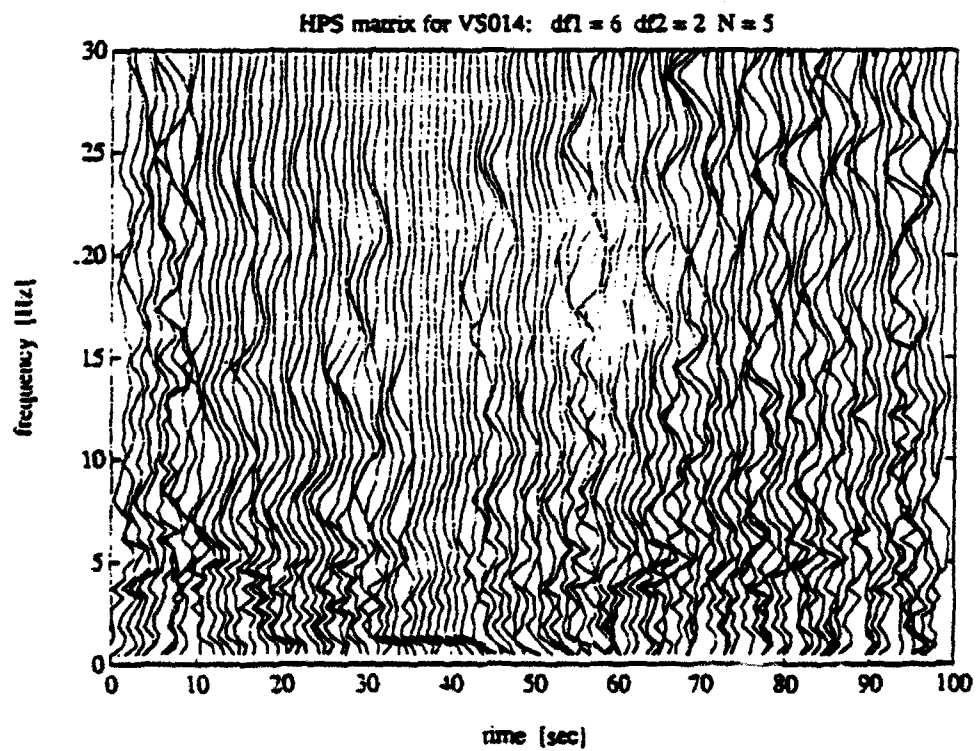
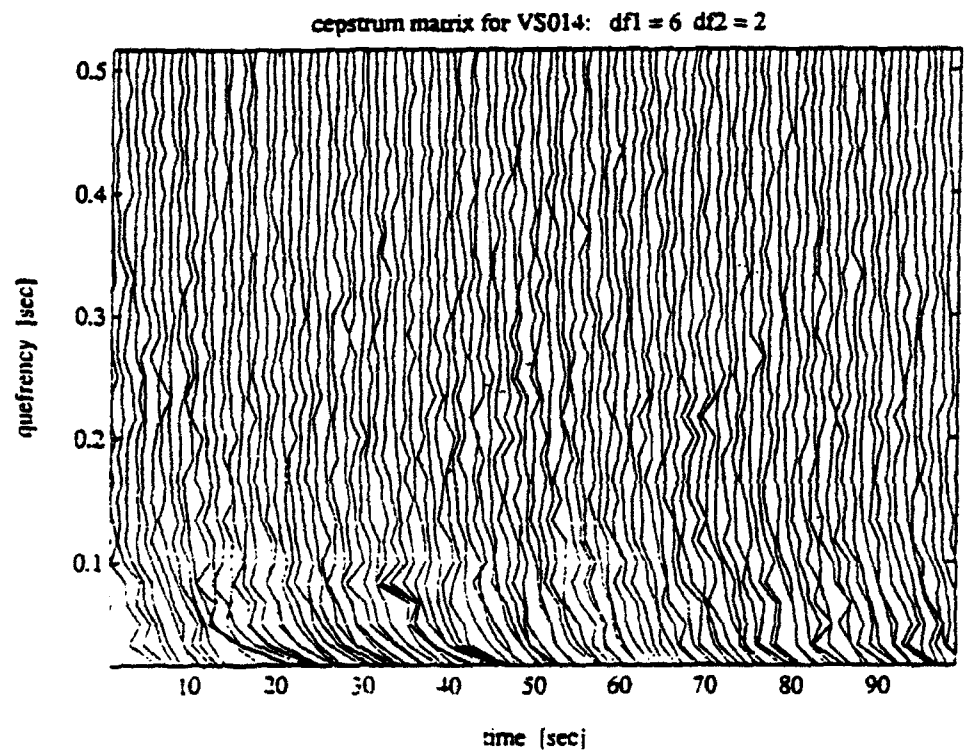


Figure 7-7: Harmonic Product Spectrum (HPS) of synthetic data

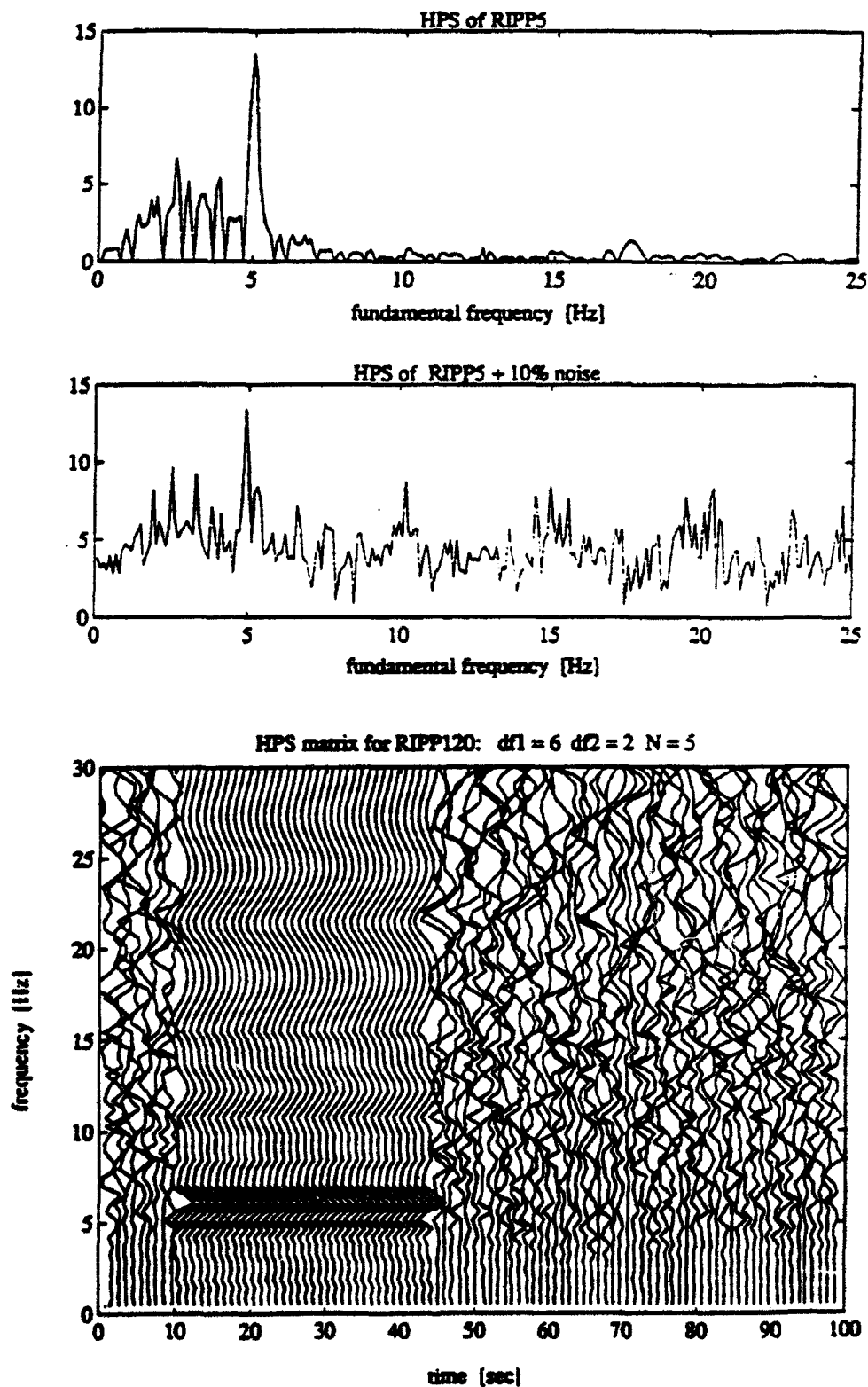
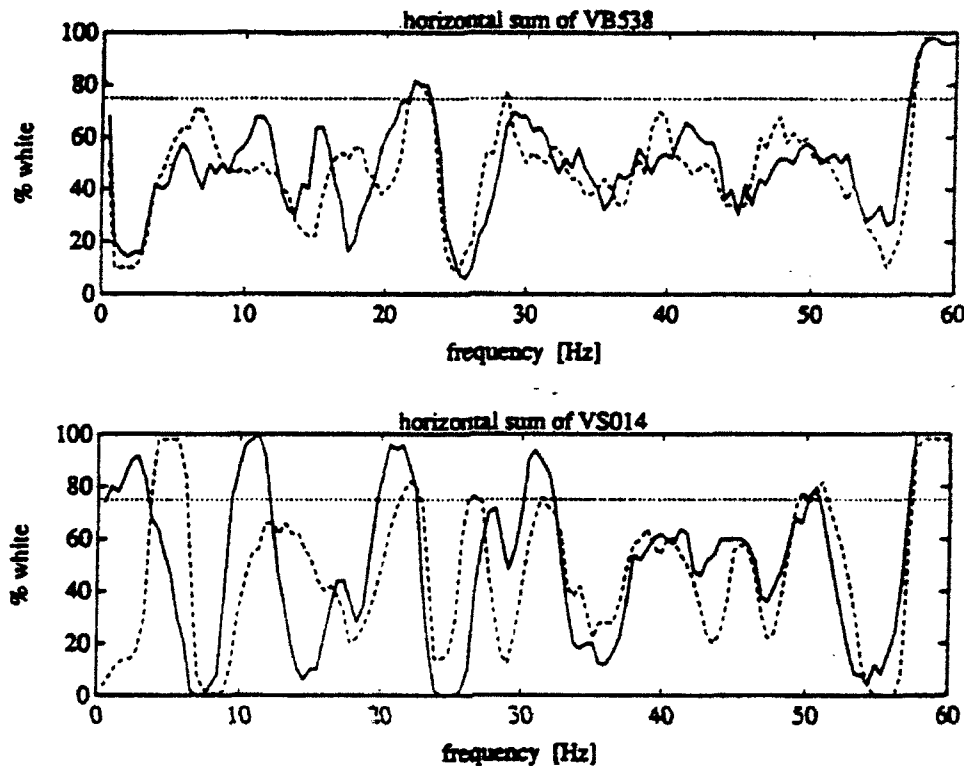


Figure 7-8: Horizontal sums across the 1-bit-compressed digital matrices. (Solid lines: over signal sections, broken lines: over noise sections.) Upper trace: Vogtland earthquake, lower trace: Vogtland explosion



signal, separate sums are calculated for the signal section ($t = 10 \dots 60 \text{ sec}$) and the noise sections ($t = 0 \dots 10$ and $60 \dots 100 \text{ sec}$) of each matrix. Two examples are shown in Figure 7-8. A band is declared, where the signal sum surpasses the 75% threshold and the noise-sum does not. A tool was developed which enables the observer to interactively determine the middle frequency of these bands (Fig. 7-9.) In the Vogtland discrimination study mentioned above, the number of bands thus determined discriminated effectively between a population of commercial blasts and earthquakes, as shown by the histogram in Figure 7-10.

7.6 Determination of blasting delays

A study on Czech quarries has given reason to expect, that most of the explosions used in the Vogtland discrimination study originate in the two coal strip mines "Jiri Vintirov" and "Nove Sedlo", within 2 km of each other, close to the town of Karlovy Vary. Speculating that blasting techniques may therefore be similar in many cases, the detected spectral bands were stacked in spectral bins of 1 Hz width. The resulting histogram is shown in Figure 7-11, the positions of stationary noise-bands are also indicated.

Peaks of 4 or more are obtained from the histogram at frequency bins

Figure 7-9: A tool to interactively pick the frequency bands

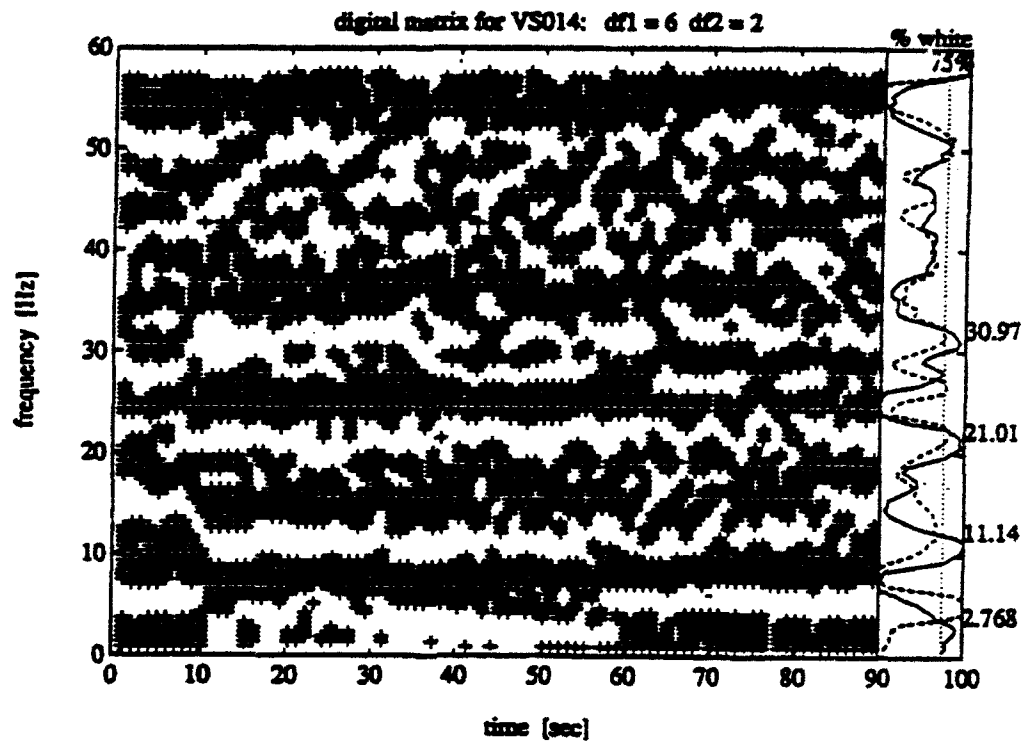


Figure 7-10: The number of frequency bands observed is a powerful discriminant between earthquakes and blasts in the Vogtland region

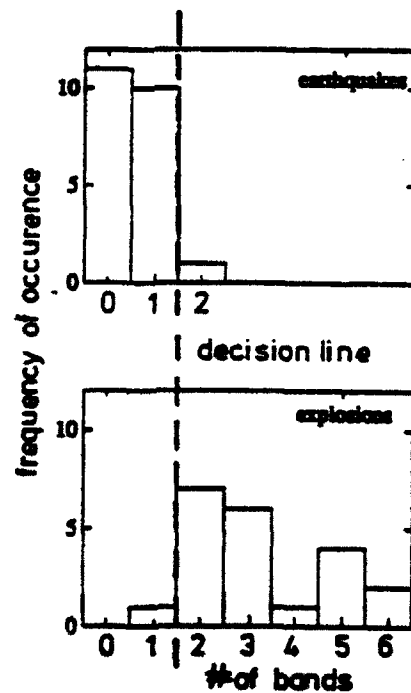
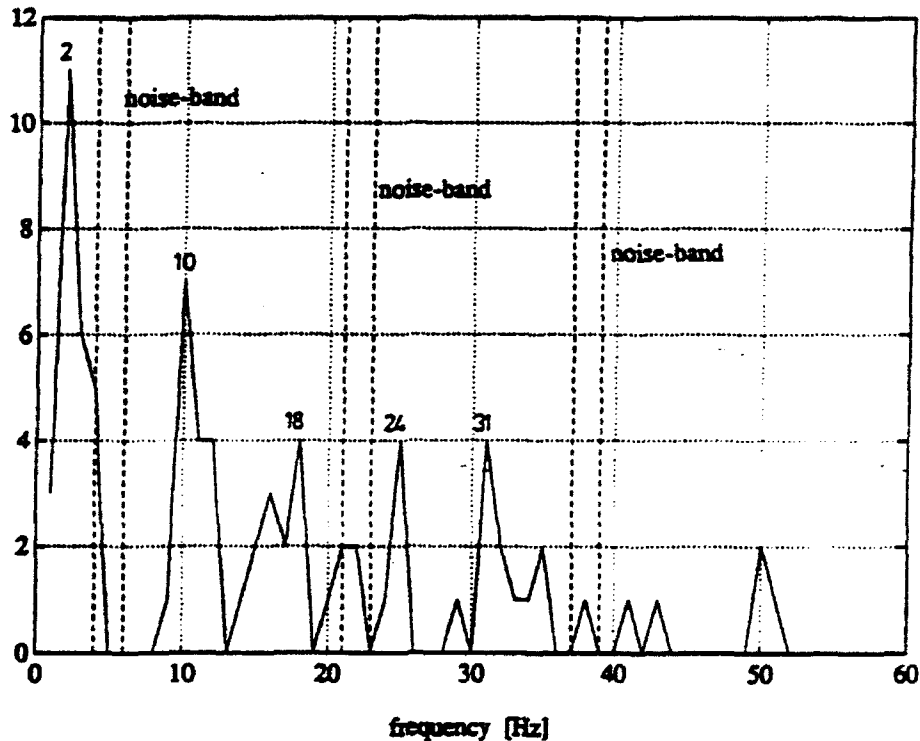


Figure 7-11: Stacked spectral bands for Vogtland explosions



of 2, 10, 18, 25 and 31 Hz. The distance between successive peaks is fairly regular (6-8 Hz, on the average 7.5 Hz) There is, however, no fundamental frequency, of which the detected bands are integer multiples. This is to say we are looking at unharmonic overtones. The spectral periods observed correspond to quefrequencies between 125 and 166 msec (138 msec on the average.) While this is clearly above typical inter-hole delays, it is of the order of typical inter-row delays reported by Chapman et al. (1991) from Appalachian explosions. Until now, no contact has been established to the Czech blasting engineers in order to compare actual blasting techniques to these results.

7.7 Discussion

In theory, ripple firing should give rise to spectral reinforcements at harmonic overtones to the fundamental frequency, which corresponds to the inter-shot delay. A number of authors has noted that this phenomenon is very susceptible to disturbances almost inevitable in blasting practice. Chapman et al. (1991) have shown that the interference of delays between individual holes and the delays between rows of holes already introduces substantial noise into the spectrum. Smith (1989) argues that the main effect of time scatter in blasting caps would be to suppress higher-order harmonics, leaving lower-order harmonics intact. But Reamer et al. (1992) obtain severe suppression and shift of maxima already at a time scatter of only 2%. At 6% time scat-

ter, a realistic figure according to these authors, even the first reinforcement is shifted from its theoretical value. In addition the effects of scatter in the charge sizes must be considered.

The authors (Reamer et al. 1992) were able to observe the harmonic spectra predicted by theory within 100 m of small ripple-fired explosions, using a precise electronic firing system. At regional distances from complex explosions fired with conventional (chemical) delays, only unharmonic and noisy spectral reinforcements can be observed in the form of time-independent spectral structures. Under these circumstances, cepstral and harmonic methods may be inadequate to quantify the phenomenon. The calculation of horizontal sums across 1-bit-compressed sonogram matrices explicitly makes use of the time-independent nature of the structures and is well suited to quantify the observed spectral banding.

The idea to try horizontal sums emerged in a discussion with Johannes Schweitzer, which is gratefully acknowledged.

References

- Båth, Markus (1974)
Spectral Analysis in Geophysics. Amsterdam, Oxford, New York (Elsevier), 1974.
- Baumgard, D. R. & K. A. Ziegler (1988)
Spectral evidence for source multiplicity in explosions: application to regional discrimination of earthquakes and explosions. *Bull. Seismol. Soc. Am.* 78, No. 5, 1773-1795.
- Chapman, M. C., G. A. Bolliger & M. S. Sibol (1991)
Spectral studies of the elastic wave radiation from Appalachian earthquakes and explosions - explosion source spectra modeling using blaster's logs. Phillips Laboratory, Report PL-TR-91-2231, 1 Sept 1991. ADA243956
- Chapman, M. C., G. A. Bolliger & M. S. Sibol (1992)
Modeling delay-fired explosion spectra and source function deconvolution at regional distances. Phillips Laboratory, Report PL-TR-92-2250, 30 Sept 1992. ADA260232
- Dysart, P. S. & J. J. Pulli (1990)
Regional seismic event classification at the NORESS array: seismological measurements and the use of trained neural networks. *Bull. Seismol. Soc. Am.* 80, Part B, 1910-1933.

- Hedlin, A. H., J. B. Minster & J. A. Orcutt (1989)
The time-frequency characteristics of quarry blasts and calibration explosions recorded in Kazakhstan, USSR. *Geophys. J. Int.* 99, 109-121.
- Lu, Shin-yee & Yoa-chou Cheng (1990)
An iterative approach to seismic skeletonization. *Geophysics* 55 No. 10, 1312-1320.
- Noll, Michael A. (1963)
Short-time spectrum and "cepstrum" techniques for vocal-pitch detection. *J. Acoust. Soc. Am.* 36, No. 2, 296-302.
- Reamer, S. K., K.-G. Hinzen & B. W. Stump (1992)
Near-source characterization of the seismic wavefield radiated from quarry blasts. *Geophys. J. Int.* 110 No. 3, 435-450.
- Schroeder, Manfred R. (1965) *Wave Analyzer*. US Patent 3,321,582. Filed Dec 9 1965, patented May 23 1967.
- Schroeder, M. R. (1968)
Period histogram and product spectrum: new methods for fundamental-frequency measurement. *J. Acoust. Soc. Am.* 43, No. 4, 829-834.
- Smith, Albert T. (1989)
High-frequency seismic observations and models of chemical explosions: implications for the discrimination of ripple-fired mining blasts. *Bull. Seismol. Soc. Am.* 79, No. 4, 1089-1110.
- Wüster, Jan (1993)
Discrimination of chemical explosions and earthquakes in Central Europe - a case study. Accepted for publication in *Bull. Seismol. Soc. Am.*

Prof. Thomas Ahrens
Seismological Lab, 252-21
Division of Geological & Planetary Sciences
California Institute of Technology
Pasadena, CA 91125

Prof. Keiiti Aki
Center for Earth Sciences
University of Southern California
University Park
Los Angeles, CA 90089-0741

Prof. Shelton Alexander
Geosciences Department
403 Deike Building
The Pennsylvania State University
University Park, PA 16802

Dr. Ralph Alewine, III
DARPA/NMRO
3701 North Fairfax Drive
Arlington, VA 22203-1714

Prof. Charles B. Archambeau
CIRES
University of Colorado
Boulder, CO 80309

Dr. Thomas C. Bache, Jr.
Science Applications Int'l Corp.
10260 Campus Point Drive
San Diego, CA 92121 (2 copies)

Prof. Muawia Barazangi
Institute for the Study of the Continent
Cornell University
Ithaca, NY 14853

Dr. Jeff Barker
Department of Geological Sciences
State University of New York
at Binghamton
Vestal, NY 13901

Dr. Douglas R. Baumgardt
ENSCO, Inc
5400 Port Royal Road
Springfield, VA 22151-2388

Dr. Susan Beck
Department of Geosciences
Building #77
University of Arizona
Tucson, AZ 85721

Dr. T.J. Bennett
S-CUBED
A Division of Maxwell Laboratories
11800 Sunrise Valley Drive, Suite 1212
Reston, VA 22091

Dr. Robert Blandford
AFTAC/TT, Center for Seismic Studies
1300 North 17th Street
Suite 1450
Arlington, VA 22209-2308

Dr. Stephen Bratt
Center for Seismic Studies
1300 North 17th Street
Suite 1450
Arlington, VA 22209-2308

Dr. Lawrence Burdick
IGPP, A-025
Scripps Institute of Oceanography
University of California, San Diego
La Jolla, CA 92093

Dr. Robert Burrige
Schlumberger-Doll Research Center
Old Quarry Road
Ridgefield, CT 06877

Dr. Jerry Carter
Center for Seismic Studies
1300 North 17th Street
Suite 1450
Arlington, VA 22209-2308

Dr. Eric Chael
Division 9241
Sandia Laboratory
Albuquerque, NM 87185

Dr. Martin Chapman
Department of Geological Sciences
Virginia Polytechnical Institute
21044 Derring Hall
Blacksburg, VA 24061

Prof. Vernon F. Cormier
Department of Geology & Geophysics
U-45, Room 207
University of Connecticut
Storrs, CT 06268

Prof. Steven Day
Department of Geological Sciences
San Diego State University
San Diego, CA 92182

Marvin Denny
U.S. Department of Energy
Office of Arms Control
Washington, DC 20585

Dr. Cliff Frolich
Institute of Geophysics
8701 North Mopac
Austin, TX 78759

Dr. Zoltan Der
ENSCO, Inc.
5400 Port Royal Road
Springfield, VA 22151-2388

Dr. Holly Given
IGPP, A-025
Scripps Institute of Oceanography
University of California, San Diego
La Jolla, CA 92093

Prof. Adam Dziewonski
Hoffman Laboratory, Harvard University
Dept. of Earth Atmos. & Planetary Sciences
20 Oxford Street
Cambridge, MA 02138

Dr. Jeffrey W. Given
SAIC
10260 Campus Point Drive
San Diego, CA 92121

Prof. John Ebel
Department of Geology & Geophysics
Boston College
Chestnut Hill, MA 02167

Dr. Dale Glover
Defense Intelligence Agency
ATTN: ODT-1B
Washington, DC 20301

Eric Fielding
SNEE Hall
INSTOC
Cornell University
Ithaca, NY 14853

Dr. Indra Gupta
Teledyne Geotech
314 Montgomery Street
Alexandria, VA 22314

Dr. Mark D. Fisk
Mission Research Corporation
735 State Street
P.O. Drawer 719
Santa Barbara, CA 93102

Dan N. Hagedorn
Pacific Northwest Laboratories
Battelle Boulevard
Richland, WA 99352

Prof Stanley Flatte
Applied Sciences Building
University of California, Santa Cruz
Santa Cruz, CA 95064

Dr. James Hannon
Lawrence Livermore National Laboratory
P.O. Box 808
L-205
Livermore, CA 94550

Dr. John Foley
NER-Geo Sciences
1100 Crown Colony Drive
Quincy, MA 02169

Dr. Roger Hansen
HQ AFTAC/TTR
130 South Highway A1A
Patrick AFB, FL 32925-3002

Prof. Donald Forsyth
Department of Geological Sciences
Brown University
Providence, RI 02912

Prof. David G. Harkrider
Seismological Laboratory
Division of Geological & Planetary Sciences
California Institute of Technology
Pasadena, CA 91125

Dr. Art Frankel
U.S. Geological Survey
922 National Center
Reston, VA 22092

Prof. Danny Harvey
CIRES
University of Colorado
Boulder, CO 80309

Prof. Donald V. Helmberger
Seismological Laboratory
Division of Geological & Planetary Sciences
California Institute of Technology
Pasadena, CA 91125

Prof. Eugene Herrin
Institute for the Study of Earth and Man
Geophysical Laboratory
Southern Methodist University
Dallas, TX 75275

Prof. Robert B. Herrmann
Department of Earth & Atmospheric Sciences
St. Louis University
St. Louis, MO 63156

Prof. Lane R. Johnson
Seismographic Station
University of California
Berkeley, CA 94720

Prof. Thomas H. Jordan
Department of Earth, Atmospheric &
Planetary Sciences
Massachusetts Institute of Technology
Cambridge, MA 02139

Prof. Alan Kafka
Department of Geology & Geophysics
Boston College
Chestnut Hill, MA 02167

Robert C. Kemerait
ENSCO, Inc.
445 Pineda Court
Melbourne, FL 32940

Dr. Karl Koch
Institute for the Study of Earth and Man
Geophysical Laboratory
Southern Methodist University
Dallas, Tx 75275

Dr. Max Koontz
U.S. Dept. of Energy/DP 5
Forrestal Building
1000 Independence Avenue
Washington, DC 20585

Dr. Richard LaCoss
MIT Lincoln Laboratory, M-200B
P.O. Box 73
Lexington, MA 02173-0073

Dr. Fred K. Lamb
University of Illinois at Urbana-Champaign
Department of Physics
1110 West Green Street
Urbana, IL 61801

Prof. Charles A. Langston
Geosciences Department
403 Deike Building
The Pennsylvania State University
University Park, PA 16802

Jim Lawson, Chief Geophysicist
Oklahoma Geological Survey
Oklahoma Geophysical Observatory
P.O. Box 8
Leonard, OK 74043-0008

Prof. Thorne Lay
Institute of Tectonics
Earth Science Board
University of California, Santa Cruz
Santa Cruz, CA 95064

Dr. William Leith
U.S. Geological Survey
Mail Stop 928
Reston, VA 22092

Mr. James F. Lewkowicz
Phillips Laboratory/GPEH
29 Randolph Road
Hanscom AFB, MA 01731-3010(2 copies)

Mr. Alfred Lieberman
ACDA/VI-OA State Department Building
Room 5726
320-21st Street, NW
Washington, DC 20451

Prof. L. Timothy Long
School of Geophysical Sciences
Georgia Institute of Technology
Atlanta, GA 30332

Dr. Randolph Martin, III
New England Research, Inc.
76 Olcott Drive
White River Junction, VT 05001

Dr. Robert Masse
Denver Federal Building
Box 25046, Mail Stop 967
Denver, CO 80225

Dr. Gary McCartor
Department of Physics
Southern Methodist University
Dallas, TX 75275

Prof. Thomas V. McEvilly
Seismographic Station
University of California
Berkeley, CA 94720

Dr. Art McGarr
U.S. Geological Survey
Mail Stop 977
U.S. Geological Survey
Menlo Park, CA 94025

Dr. Keith L. McLaughlin
S-CUBED
A Division of Maxwell Laboratory
P.O. Box 1620
La Jolla, CA 92038-1620

Stephen Miller & Dr. Alexander Florence
SRI International
333 Ravenswood Avenue
Box AF 116
Menlo Park, CA 94025-3493

Prof. Bernard Minster
IGPP, A-025
Scripps Institute of Oceanography
University of California, San Diego
La Jolla, CA 92093

Prof. Brian J. Mitchell
Department of Earth & Atmospheric Sciences
St. Louis University
St. Louis, MO 63156

Mr. Jack Murphy
S-CUBED
A Division of Maxwell Laboratory
11800 Sunrise Valley Drive, Suite 1212
Reston, VA 22091 (2 Copies)

Dr. Keith K. Nakanishi
Lawrence Livermore National Laboratory
L-025
P.O. Box 808
Livermore, CA 94550

Dr. Carl Newton
Los Alamos National Laboratory
P.O. Box 1663
Mail Stop C335, Group ESS-3
Los Alamos, NM 87545

Dr. Bao Nguyen
HQ AFTAC/TTR
130 South Highway A1A
Patrick AFB, FL 32925-3002

Prof. John A. Orcutt
IGPP, A-025
Scripps Institute of Oceanography
University of California, San Diego
La Jolla, CA 92093

Prof. Jeffrey Park
Kline Geology Laboratory
P.O. Box 6666
New Haven, CT 06511-8130

Dr. Howard Patton
Lawrence Livermore National Laboratory
L-025
P.O. Box 808
Livermore, CA 94550

Dr. Frank Pilotte
HQ AFTAC/TT
130 South Highway A1A
Patrick AFB, FL 32925-3002

Dr. Jay J. Pulli
Radix Systems, Inc.
201 Perry Parkway
Gaithersburg, MD 20877

Dr. Robert Reinke
ATTN: FCTVTD
Field Command
Defense Nuclear Agency
Kirtland AFB, NM 87115

Prof. Paul G. Richards
Lamont-Doherty Geological Observatory
of Columbia University
Palisades, NY 10964

Mr. Wilmer Rivers
Teledyne Geotech
314 Montgomery Street
Alexandria, VA 22314

Dr. George Rothe
HQ AFTAC/TTR
130 South Highway A1A
Patrick AFB, FL 32925-3002

Dr. Alan S. Ryall, Jr.
DARPA/NMRO
3701 North Fairfax Drive
Arlington, VA 22209-1714

Dr. Richard Sailor
TASC, Inc.
55 Walkers Brook Drive
Reading, MA 01867

Prof. Charles G. Sammis
Center for Earth Sciences
University of Southern California
University Park
Los Angeles, CA 90089-0741

Prof. Christopher H. Scholz
Lamont-Doherty Geological Observatory
of Columbia University
Palisades, NY 10964

Dr. Susan Schwartz
Institute of Tectonics
1156 High Street
Santa Cruz, CA 95064

Secretary of the Air Force
(SAFRD)
Washington, DC 20330

Office of the Secretary of Defense
DDR&E
Washington, DC 20330

Thomas J. Sereno, Jr.
Science Application Int'l Corp.
10260 Campus Point Drive
San Diego, CA 92121

Dr. Michael Shore
Defense Nuclear Agency/SPSS
6801 Telegraph Road
Alexandria, VA 22310

Dr. Robert Shumway
University of California Davis
Division of Statistics
Davis, CA 95616

Dr. Matthew Sibol
Virginia Tech
Seismological Observatory
4044 Derring Hall
Blacksburg, VA 24061-0420

Prof. David G. Simpson
IRIS, Inc.
1616 North Fort Myer Drive
Suite 1050
Arlington, VA 22209

Donald L. Springer
Lawrence Livermore National Laboratory
L-025
P.O. Box 808
Livermore, CA 94550

Dr. Jeffrey Stevens
S-CUBED
A Division of Maxwell Laboratory
P.O. Box 1620
La Jolla, CA 92038-1620

Lt. Col. Jim Stobie
ATTN: AFOSR/NL
110 Duncan Avenue
Bolling AFB
Washington, DC 20332-0001

Prof. Brian Stump
Institute for the Study of Earth & Man
Geophysical Laboratory
Southern Methodist University
Dallas, TX 75275

Prof. Jeremiah Sullivan
University of Illinois at Urbana-Champaign
Department of Physics
1110 West Green Street
Urbana, IL 61801

Prof. L. Sykes
Lamont-Doherty Geological Observatory
of Columbia University
Palisades, NY 10964

Dr. David Taylor
ENSCO, Inc.
445 Pineda Court
Melbourne, FL 32940

Dr. Steven R. Taylor
Los Alamos National Laboratory
P.O. Box 1663
Mail Stop C335
Los Alamos, NM 87545

Prof. Clifford Thurber
University of Wisconsin-Madison
Department of Geology & Geophysics
1215 West Dayton Street
Madison, WI 53706

DARPA/PM
3701 North Fairfax Drive
Arlington, VA 22203-1714

Prof. M. Nafi Toksoz
Earth Resources Lab
Massachusetts Institute of Technology
42 Carleton Street
Cambridge, MA 02142

DARPA/RMO/RETRIEVAL
3701 North Fairfax Drive
Arlington, VA 22203-1714

Dr. Larry Turnbull
CIA-OSWR/NED
Washington, DC 20505

DARPA/RMO/SECURITY OFFICE
3701 North Fairfax Drive
Arlington, VA 22203-1714

Dr. Gregory van der Vink
IRIS, Inc.
1616 North Fort Myer Drive
Suite 1050
Arlington, VA 22209

HQ DNA
ATTN: Technical Library
Washington, DC 20305

Dr. Karl Veith
EG&G
5211 Auth Road
Suite 240
Suitland, MD 20746

Defense Intelligence Agency
Directorate for Scientific & Technical Intelligence
ATTN: DTIB
Washington, DC 20340-6158

Prof. Terry C. Wallace
Department of Geosciences
Building #77
University of Arizona
Tucson, AZ 85721

Defense Technical Information Center
Cameron Station
Alexandria, VA 22314 (2 Copies)

Dr. Thomas Weaver
Los Alamos National Laboratory
P.O. Box 1663
Mail Stop C335
Los Alamos, NM 87545

TACTEC
Battelle Memorial Institute
505 King Avenue
Columbus, OH 43201 (Final Report)

Dr. William Wortman
Mission Research Corporation
8560 Cinderbed Road
Suite 700
Newington, VA 22122

Phillips Laboratory
ATTN: XPG
29 Randolph Road
Hanscom AFB, MA 01731-3010

Prof. Francis T. Wu
Department of Geological Sciences
State University of New York
at Binghamton
Vestal, NY 13901

Phillips Laboratory
ATTN: GPE
29 Randolph Road
Hanscom AFB, MA 01731-3010

AFTAC/CA
(STINFO)
Patrick AFB, FL 32925-6001

Phillips Laboratory
ATTN: TSML
5 Wright Street
Hanscom AFB, MA 01731-3004

Phillips Laboratory
ATTN: PL/SUL
3550 Aberdeen Ave SE
Kirtland, NM 87117-5776 (2 copies)

Dr. Svein Mykkeltveit
NTNT/NORSAR
P.O. Box 51
N-2007 Kjeller, NORWAY (3 Copies)

Dr. Michel Bouchon
I.R.I.G.M.-B.P. 68
38402 St. Martin D'Heres
Cedex, FRANCE

Prof. Keith Priestley
University of Cambridge
Bullard Labs, Dept. of Earth Sciences
Madingley Rise, Madingley Road
Cambridge CB3 0EZ, ENGLAND

Dr. Michel Campillo
Observatoire de Grenoble
I.R.I.G.M.-B.P. 53
38041 Grenoble, FRANCE

Dr. Jorg Schlittenhardt
Federal Institute for Geosciences & Nat'l Res.
Postfach 510153
D-3000 Hannover 51, GERMANY

Dr. Kin Yip Chun
Geophysics Division
Physics Department
University of Toronto
Ontario, CANADA

Dr. Johannes Schweitzer
Institute of Geophysics
Ruhr University/Bochum
P.O. Box 1102148
4360 Bochum 1, GERMANY

Prof. Hans-Peter Harjes
Institute for Geophysics
Ruhr University/Bochum
P.O. Box 102148
4630 Bochum 1, GERMANY

Trust & Verify
VERTIC
8 John Adam Street
London WC2N 6EZ, ENGLAND

Prof. Eystein Husebye
NTNF/NORSAR
P.O. Box 51
N-2007 Kjeller, NORWAY

David Jepsen
Acting Head, Nuclear Monitoring Section
Bureau of Mineral Resources
Geology and Geophysics
G.P.O. Box 378, Canberra, AUSTRALIA

Ms. Eva Johannisson
Senior Research Officer
FOA
S-172 90 Sundbyberg, SWEDEN

Dr. Peter Marshall
Procurement Executive
Ministry of Defense
Blacknest, Brimpton
Reading RG7-FRS, UNITED KINGDOM

Dr. Bernard Massinon, Dr. Pierre Mechler
Societe Radiomana
27 rue Claude Bernard
75005 Paris, FRANCE (2 Copies)